Purdue University
Purdue e-Pubs

Open Access Theses | Theses and Dissertations

2013

A Pulsed Jet for Generation of Turbulent Spots in a Mach 6 Boundary Layer

Andrew Daniel Abney
Purdue University, andrew.abney@gmail.com

Follow this and additional works at: https://docs.lib.purdue.edu/open_access_theses

 Part of the Aerospace Engineering Commons

Recommended Citation
Abney, Andrew Daniel, "A Pulsed Jet for Generation of Turbulent Spots in a Mach 6 Boundary Layer" (2013). *Open Access Theses*. 8.
https://docs.lib.purdue.edu/open_access_theses/8

This document has been made available through Purdue e-Pubs, a service of the Purdue University Libraries. Please contact epubs@purdue.edu for additional information.

Graduate School ETD Form 9
(Revised 12/07)

PURDUE UNIVERSITY
GRADUATE SCHOOL
Thesis/Dissertation Acceptance

This is to certify that the thesis/dissertation prepared

By Andrew Daniel Abney

Entitled
A Pulsed Jet for Generation of Turbulent Spots in a Mach 6 Boundary Layer

For the degree of Master of Science in Engineering

Is approved by the final examining committee:

Steven Schneider
Chair

Steven Collicott

Steven Beresh

To the best of my knowledge and as understood by the student in the *Research Integrity and Copyright Disclaimer (Graduate School Form 20)*, this thesis/dissertation adheres to the provisions of Purdue University's "Policy on Integrity in Research" and the use of copyrighted material.

Approved by Major Professor(s): Steven Schneider

Approved by: Tom Shih 10/31/2013
Head of the Graduate Program Date

A PULSED JET FOR GENERATION OF TURBULENT SPOTS IN A MACH 6 BOUNDARY LAYER

A Thesis

Submitted to the Faculty

of

Purdue University

by

Andrew D. Abney

In Partial Fulfillment of the

Requirements for the Degree

of

Master of Science in Engineering

December 2013

Purdue University

West Lafayette, Indiana

For Brooke, who encouraged me to chase after greater things, and supported me through it all.

ACKNOWLEDGMENTS

A great many thanks to the people who have helped me through this entire process. First to my parents, who instilled in me the value of an education, the importance of hard work, and more than anything, illustrated to me how to carry myself as a godly man. To Brooke, who encouraged me during the difficulties of graduate school, and kept me on task better than I could have ever done by myself. To my office mates, Amanda Chou, Brad Wheaton, Brandon Chynoweth, Chris Ward, Dennis Berridge, George Moraru, Greg McKiernan, Katya Casper, Ryan Henderson, Ryan Luersen, and Roger Greenwood, you have all offered encouragement and help when my personal knowledge fell short. To my small group, who have encouraged me in countless ways. To Dr. Schneider, who illustrated daily the life of a careful scientist, and never left a doubt that one of the foremost values he had was the development of his students. To the ASL machine shop, Gerry Hahn, Jim Younts and Robin Snodgrass, this project would have been impossible without your skill as machinists. This work was funded by Sandia National Labs, and also the Air Force Office of Scientific Research, under grant FA9550-12-1-0167.

TABLE OF CONTENTS

LIST OF TABLES

LIST OF FIGURES

Figure Page

Figure Page

SYMBOLS

C	capacitance
f	frequency
M	Mach number
p	pressure
R	resistance
Re	freestream unit Reynolds number
t	time
T	temperature
U	velocity
y	perpendicular distance from the nozzle wall
z	tunnel axial location, relative to throat
γ	intermittency factor
Φ	power spectral density
τ	hot wire response time, time span for weighted average

Subscripts

0	stagnation condition
$0v$	valve stagnation condition
le	leading edge
max	maximum value
$mean$	average value
min	minimum value
te	trailing edge

ABBREVIATIONS

AAE	Purdue University School of Aeronautics and Astronautics
BAM6QT	Boeing/AFOSR Mach 6 Quiet Tunnel
CTA	Constant Temperature Anemometry
DNS	direct numerical simulation
FFT	fast Fourier transform
FSO	full scale output
JAFCI	Johnathan Amy Facility for Chemical Instrumentation
PEEK	polyether ether ketone
PTFE	polytetraflouroethylene
PSD	power spectral density
RMS	root mean square

ABSTRACT

Abney, Andrew D. M.S.E., Purdue University, December 2013. A pulsed jet for generation of turbulent spots in a Mach 6 boundary layer. Major Professor: Steven P. Schneider.

Hypersonic vehicles operate in an environment with a high level of boundary-layer pressure fluctuations. The largest of these fluctuations are due to the intermittent passage of turbulent spots within the transition region, and can be sufficiently large to affect internal components of the vehicle. In order to better predict these flow variations, a turbulent spot model could be used. The boundary layer on the Boeing/AFOSR Mach 6 Quiet Tunnel nozzle-wall provided a convenient location for studying the statistical properties of turbulent spots in a hypersonic boundary layer, including growth rates, convection velocities, and pressure-fluctuation intensities. A valve system was developed to inject a transverse jet of air into the nozzle-wall boundary layer in an attempt to generate controlled spots. The resulting perturbations were characterized.

The pressure fluctuations were measured on the tunnel centerline downstream of the perturber. Pressure traces and spectra were examined to determine the effectiveness of the perturber system. The initial perturber system produced disturbances with a duration that was too long. A reduction in perturbation duration was achieved through modification of the perturber electronics. Physical modifications were also made to the valve, with mixed success. The perturbations were of a longer duration and higher initial amplitude than perturbations generated using a pulsed glow perturber in previous studies in the Boeing/AFOSR Mach-6 Quiet Tunnel, including fully turbulent perturbations at the maximum quiet freestream Reynolds number.

Inconsistent alignment of the perturber became the largest difficulty in using the device. A new method of aligning the valve was developed. A more effective means of

maintaining the alignment during transfer from the alignment tool to the nozzle wall is necessary. Additional reductions to the perturbation duration could be possible by optimizing the geometry of the passage through the nozzle wall. Presently, the perturber requires further refinement prior to use as a tool for generating repeatable turbulent spots.

1. Introduction

Hypersonic vehicles undergoing boundary-layer transition are subject to high amplitude pressure fluctuations due to the intermittent passage of turbulent spots. The transitional region along hypersonic vehicles can extend over significant portions of the vehicle length [1]. It has been shown that the pressure fluctuations are higher within the transitional region than in the fully turbulent flow. However, the pressure fluctuation field within the transitional region of hypersonic vehicles is still poorly understood. As a result, vehicles are often designed using conservative estimates of the pressure fluctuation field, leading to over-designed components. Several correlations exist for predicting pressure fluctuation levels within the transitional region. These correlations often rely on low-speed wind-tunnel tests or transition data from conventional hypersonic wind tunnels. The low-speed models neglect high-speed physics such as second-mode waves, whereas the conventional tunnel data are contaminated with acoustic noise radiated from the turbulent boundary layer on the nozzle wall [2]. Such tests have not provided sufficient understanding of the underlying physical processes that lead to transition.

In order to accurately model the transitional pressure field, an intermittency model of turbulent spot transition could be used [3]. The intermittency factor denotes the probability that a certain location will have turbulent flow, and varies from 0 for fully laminar flow to 1 for fully turbulent flow. This model assumes that upstream instabilities transition to infinitesimal turbulent spots at a single axial location. Estimations of this location can be determined from computations or an e^n calculation. Turbulent spots are generated randomly in time and span at the transition onset location, and grow as they convect downstream. With knowledge of the growth rate of turbulent spots and the spot formation rate per unit span, the length of the transitional region can be determined. This can then be combined with knowledge of the pres-

sure field underneath hypersonic turbulent spots to predict fluctuation amplitudes in transitional flow, similar to the model developed by Park and Lauchle for low-speed flat-plate flows [3].

Casper measured some of the growth parameters of young turbulent spots in a hypersonic boundary layer, including the low-frequency footprint of turbulent spots and the leading and trailing edge convection rates [4,5]. In order to accurately predict the pressure field, however, the interaction between two merging turbulent spots must be understood. Recent direct numerical simulation (DNS) computations have shown that there is some interaction between merging turbulent spots at high speeds [6]. Casper made initial measurements of longitudinally merging turbulent spots, but was unable to measure laterally merging turbulent spots due to limitations in the flow perturber used. A deeper understanding of this interaction is necessary for development of a high speed analog of Park and Lauchle's model. Additionally, an understanding of the dependence of spot parameters on the perturbation generation method is desired.

Measurements will be made within the nozzle-wall boundary layer of the Boeing/AFOSR Mach-6 Quiet Tunnel (BAM6QT). The BAM6QT nozzle wall is a good location for the measurement of turbulent spots. The thick nozzle-wall boundary layer allows for lower frequency disturbances and greater spatial resolution. Casper's work was conducted in the BAM6QT using a pulsed glow perturber. Unfortunately, the relatively small amplitude of the disturbances that were generated resulted in instability wave packets that convected well downstream prior to transitioning to turbulent spots. As a result, the turbulent spots convected downstream of the sensors prior to growing enough for two independent perturbations to merge laterally. The development of a new flow perturber to produce turbulent spots further upstream within the BAM6QT nozzle-wall boundary layer is necessary to measure laterally merging turbulent spots and the growth of more mature turbulent spots. This requires a new perturber capable of producing disturbances with higher initial amplitudes than the existing pulsed glow perturber with a high level of repeatability.

A pneumatic pulsed jet system which injects a transverse jet of high density air into the nozzle wall boundary layer is under investigation as a new perturber for the generation of turbulent spots. The Parker-Hannafin Corporation already has a pulsed valve system designed for use in spectroscopy experiments that is well suited for use in the BAM6QT. Before the system can be used to gather statistical data for usage in turbulent spot models of transition, the perturber operation must be characterized, and if need be refined to produce suitable disturbances. The primary challenge will be obtaining sufficiently short durations. The difficulties posed by a pneumatic system include fine tuning a physical system to operate on short time scales relative to the approximately 850 m/s freestream velocity in the BAM6QT. The target duration for the perturbations is between 10 and 100 μs. Reduction in the duration of the perturbations will be accomplished via optimization of the driving electrical signal and determination of a sufficient geometry for the passage through the nozzle wall. This study primarily focused on the characterization of the perturbation, and on optimizing the perturber through manipulation of the driver signal and modification of the valve.

Additionally, the development of an improved electronic perturber was pursued. This perturber was based on a Behlke high voltage transistor switch, which will allow for additional control of the generation of high voltage perturbations when compared to Casper's glow perturber [5]. This design process was delayed due to considerable manufacturing delays for the switch in question, and never left the design phase. It is unclear whether the new switch will provide enough control to improve the performance of the electronic perturbation system.

2. Review of Literature

Turbulent spots have been studied since Emmons discovered their existence in 1951 [7]. Emmons noticed turbulent disturbances in an inclined water table flow. The disturbances seemed to appear randomly in both time and space. These disturbances grew as they convected downstream, merging until the entire flow was fully turbulent. He noted that the spots seemed to grow with a defined shape, and that the spot generation rate could be increased by increasing the flow velocity. Based on this, Emmons developed an intermittency model of transition, which stated that turbulent transition was a result of the generation, growth and coalescence of turbulent spots. The spot generation rate was assumed to be independent of the location within a flow, so that spots were thought to be spontaneously generated at any location within the flow. In an initially laminar flow, disturbances would form due to the breakdown of boundary-layer instabilities '*carried in from the free stream*'. As the spots grew and convected downstream, more and more of the flow was turbulent, until the spots covered the entire span and flow was fully turbulent. Emmons denoted an intermittency factor, γ, as the portion of time that an axial location of the flow was turbulent, ranging from 0 for fully laminar flow to 1 for fully turbulent flow, and calculated its distribution based on the assumption of an independent spot generation rate.

Mitchner was the first to artificially generate turbulent spots, in a low disturbance wind tunnel at Cambridge University [8]. Mitchner generated perturbations by inserting a small projection into the flow or by a spark discharge to disturb the boundary layer flow. Although the perturbations were similar in shape to those observed by Emmons, Mitchner noted that much work was still needed to completely verify Emmons' theory that turbulent spots were responsible for transition. Mitchner suggested that further study of the intermittent region was necessary to fully confirm Emmons' theory. Schubauer and Klebanoff further studied artificially generated

turbulent spots, generated using a spark perturber in the National Bureau of Standards low disturbance wind tunnel [9]. Extensive hot-wire measurements were made of the spots at different locations downstream of the spark perturber. Schubauer and Klebanoff found that the oscillograms of artificially generated turbulent spots were indistinguishable from naturally occurring turbulence. Finally, two different sets of simultaneous hot wire measurements were made of natural turbulent transition, one with two hot-wires offset in the axial direction, and one with hot wires displaced in the wall normal direction. The streamwise separated hot wires showed that naturally occurring turbulence could be detected at the upstream location prior to the downstream location, confirming Emmons' theory that the turbulent spots convected downstream during the transition process. The wall-normal-separated hot wires showed that turbulence could be detected at the wall prior to the displaced hot wire, which showed that naturally occurring turbulence displayed the same shape at the leading edge as artificially generated turbulent spots. This led Schubauer and Klebanoff to conclude that they were actually detecting the leading edge of naturally occurring turbulent spots. This provided enough evidence for Schubauer and Klebanoff to determine that the transition process consisted of the breakdown of boundary-layer instabilities which resulted in the instantaneous generation and growth of turbulent spots that then convected downstream and merged to form a fully developed turbulent flow.

Narasimha compared Emmons theory of turbulent-spot transition to experimental measurements and noted a discrepancy between measured intermittency distributions and those calculated using Emmons theory [10]. Narasimha showed that transitional flow property calculations agreed best when the spot generation rate approached a delta function centered at the measured onset of transition, which Narasimha termed "concentrated breakdown". This agreed with the suggestion by Schubauer and Klebanoff that spot generation occurred within a narrow band centered on the measured transition location. Dhawan and Narasimha then computed various boundary layer properties within the intermittent zone [11]. When using the "concentrated-breakdown" theory, the calculation agreed quite well with measurements of various

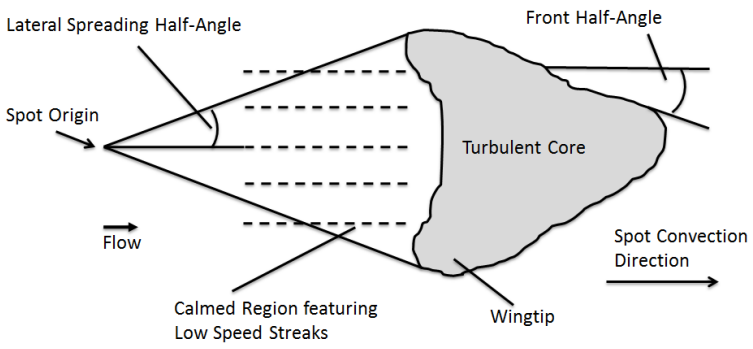

Figure 2.1. Turbulent spot schematic

boundary layer profiles. Narasimha provided an overall review of transitional flows in Reference [12].

2.1 Structure of Turbulent Spots

The general structure of a turbulent spot is shown in Figure 2.1. Most of the research noting the structure of turbulent spots was conducted in a low speed environment, and was concerned with both the structure and growth mechanisms of turbulent spots [13–16]. Turbulent spots are known to have a downstream-oriented arrowhead shape, first demonstrated by Emmons, and later confirmed by Schubauer and Klebanoff. The spot is trailed by a calmed region with a fuller velocity profile than the surrounding laminar boundary layer, which includes low speed streaks. The leading edge lifts away from the wall by approximately the height of the laminar boundary layer [17]. The spot planform geometry is defined by two primary characteristics, the lateral spreading angle and the front half angle. The wing tips of the spot also overhang above the flow surface.

Although Emmons discovered the existence of turbulent spots, Elder provided the first visualization of turbulent spots in a water tunnel [14]. Elder disturbed the flow in a water tunnel by momentarily inserting a rod into the flow to produce a turbulent spot. Dye was allowed to seep into the flow from a slit upstream of the

disturbance location, allowing visualization of the spot. The resulting images showed the arrowhead shaped region of turbulence as indicated by the hot-wire measurements of Schubauer and Klebanoff. [9]. Elder noticed that the internal structure of the spot was dominated by periodic fluctuations. Elder attributed this regular motion to the presence of coherent vortical structures. Downstream of the turbulent spot, streaks formed in the calmed region. Gad-el-Hak et al. used laser dye fluorescence to visualize cross sections of the internal structure of turbulent spots on a plexiglass plate towed through a towing tank [13]. A wall-normal sheet of laser light fluoresced dye lines as artificially generated turbulent spots convected through the flow field. The turbulent eddies revealed in this method remained coherent as they convected through the field of view.

Perry and Lin used smoke visualization to compare the footprint of a turbulent spot generated by a brief injection of air to the vortices generated by oscillating a 4.15 mm rod laying transverse to the flow [15]. Smoke visualization showed that the footprint of the turbulent spot was similar to the vortices generated using the trip wire. Antonia et al. studied the structure of the turbulent spot along the plane of symmetry using both hot and cold wire measurements [16]. The spot was generated using a spark discharge in air, and simultaneous temperature measurements were taken. Individual samples revealed the existence of spatially coherent structures within the spot. These structures occurred randomly within the spot, and as a result were obfuscated by ensemble averaging. Sankaran et al. further studied the substructures within turbulent spots using a cold wire array oriented in either the streamwise direction or the wall normal direction [18]. The cold wire arrays were able to detect substructures across both orientations. Henningson was the first to use DNS simulations to study the flowfield within turbulent spots [19]. Visualizations of the wall-normal vorticity components showed that DNS was capable of resolving the internal vortical structures within the turbulent spot.

Downstream of the turbulent core lies the calmed region. Wave packets were found in the calmed region in many studies [13,20]. The wave packets trailing the turbulent

spots appear to coincide with the predicted Tollmien-Schlichting waves in subsonic flow. The trailing wave packets were studied by Chambers and Thomas, who showed that they did not contribute the growth of the spot [21]. Glezer et al. studied the trailing wave packets at a broader range of conditions and found that breakdown to turbulence depended on the stability of the surrounding laminar boundary layer [22]. Depending on the stability, the waves would either amplify or decay.

Various methods were used in generating the artificial turbulent spots within the previously referenced works, including spark generation [9, 17], physical perturbation of the flow using a solid instrument briefly inserted in the flow [14], and fluidic injection [15, 23]. Despite the different methods used, the spot structure eventually developed into the characteristic arrowhead planform trailed by the calmed region. Chambers and Thomas used all three methods to produce turbulent spots in a low disturbance wind tunnel and found that although the initial disturbances varied, the spots ultimately developed into the familiar shape reported in literature [21], although any differences in the development length were not reported.

2.2 Growth and Interaction

In order to fully classify the growth of turbulent spots, the growth in all three dimensions must be classified. Wygnanski et al. studied the propagation of turbulent spots using hot wire anemometry in a low turbulence wind tunnel [24]. By measuring the passage of artificially generated turbulent spots at various streamwise locations downstream of the generator, they were able to effectively track the growth rate of the spots in all three dimensions. In order to improve the consistency of their measurements, care was taken to develop a spot detection parameter, which found that spectral content above 500 Hz was the most effective determination for their conditions, even though the total contribution to the turbulent energy is relatively small. With a clear detection method, they tracked the wall-normal growth of the spot. It was shown that the spot grew in the normal direction at approximately the

same rate as a turbulent boundary layer, although the data was not clear enough to determine if the spot grew linearly in the wall-normal direction, or with $x^{4/5}$ as would be expected from the growth of a turbulent boundary layer. Gad-el-Hak et al. studied streamwise cross sections and showed that the entrainment of fluid in the wall-normal direction was strikingly similar to that reported for a fully turbulent boundary layer [13].

Lateral and longitudinal growth occur too rapidly to be attributed to entrainment. Lateral growth is likely due to the destabilization of the surrounding laminar boundary layer, as Wygnanski et al. noted the spot grows in the lateral direction more than an order of magnitude faster than would be predicted by classical entrainment [23, 25]. Gad-el Hak et al. confirmed this for lateral growth through the use of dye injection on a flat plate [13]. A turbulent spot was created by injecting one color dye, while another dye color was allowed to seep out of slits in the flat plate. During the spot growth, the second color of dye was found within the turbulent spot without mixing with the initial dye color as would be required by classical entrainment. Additionally, Gad-el-Hak et al. noted oblique wave structures directly upstream of the turbulent spot, although they did not connect them with the Tollmien-Schlichting waves. Fischer compiled data on the lateral and wall-normal growth rates of turbulent spots across a range of Mach numbers, and found that the wall normal-spreading angle was nearly constant across Mach numbers from low subsonic to hypersonic at approximately 0.6 degrees [26]. However, the lateral spreading angle varied from 9-11 degrees at low subsonic velocities to 2-4 degrees within the hypersonic regime. This strengthens the argument that lateral growth is dominated by the destabilization of the surrounding laminar boundary layer; boundary layer stability increases with increasing Mach number. Casper studied the pressure field underneath instability wave packets and turbulent spots at Mach 6, and found a spreading angle of 16$\pm$2 degrees [5]. This is far higher than any angle reported by Fischer, although Casper stated that the process used to determine lateral spreading angle needed refinement, as it was difficult to distinguish second mode waves from the turbulent core with the pressure data, and it was unclear

whether the boundary should be limited to strictly turbulent fluid or include the instability waves.

Longitudinal growth can be attributed to two different mechanisms. The first is the growth of the overhang region at the leading edge of the spot. Gad-el-Hak et al. proposed that the growth of the overhang was caused by boundary layer instabilities resulting from vortex motion at the head of the overhang [13]. Secondly, vortex dynamics within the spot can induce growth of the spot by generation of new coherent structures through the '*lateral deformation of the vortex lines comprising the initial hairpin vortex, and a process of vortex-surface interaction, which causes the ejection of surface fluid and subsequent hairpin formation by viscous-inviscid interactions.*' [27]

Early investigations by Elder and Schubauer and Klebanoff showed little interaction between turbulent spots as they merged [9, 14]. When developing the intermittency model of transition, Narasimha also assumed no interaction between turbulent spots as they merged. However, recent studies have shown that turbulent spots do interact. Makita and Nishizawa used hot-wire rakes to measure the spanwise merging of turbulent spots at low speeds [28]. They showed a strong increase in upwash at the wingtips of laterally merging turbulent spots. Krishnan and Sandham ran DNS computations for laterally merging turbulent spots at Mach 2 which showed the development of inflectional velocity profiles in the wingtips of laterally merging turbulent spots in supersonic flow. This leads to additional velocity fluctuations and the generation of new coherent structures where the turbulent spots interact [29]. Additionally, the interacting wingtips result in higher intermittency factors, showing a direct effect on the turbulent spot model of transition. It is unclear as of yet how important these interactions will be in developing a turbulent spot model of transition for engineering predictions, but further study is necessary.

2.3 High Speed Work

James studied shadowgraphs of turbulent spots in compressible flow, and found that they have the same general structure as in incompressible flow [30]. Krishnan and Sandham used DNS computations to study the development of turbulent spots at a range of supersonic Mach numbers from 2 to 6, and found that the general structure was consistent and compared well with that proposed by Cantwell et al. for low speed flows [23, 29, 31]. DNS simulations by Krishnan and Sandham showed that turbulent spots in a hypersonic boundary layer are surrounded by second-mode waves (Mack mode) as opposed to the Tollmien-Schlichting waves present in subsonic turbulent spots [32]. Redford et al. conducted DNS simulations of turbulent spot development in a Mach-6 boundary layer with both an adiabatic wall and a cold wall [20]. The cold wall case showed two-dimensional structures that appeared to be second-mode waves. The waves were not readily visible in the adiabatic wall case. This lends credence to the thought that the wave structures are attributed to the second-mode instability, as it is destabilized by wall cooling.

Casper studied the pressure field of turbulent spots in a hypersonic boundary layer in the Boeing/AFOSR Mach 6 Quiet Tunnel (BAM6QT) using a pulsed glow perturber [4, 5]. Casper was able to measure the development of instability wave packets and their eventual transition to turbulent spots within the nozzle-wall boundary layer in the BAM6QT. Casper's work was aimed at developing an accurate turbulent spot model of transition for use in the design of hypersonic vehicles. An extensive set of data was collected regarding the pressure field underneath turbulent spots within a hypersonic boundary layer. Casper's work showed that instability waves are still an integral part of the structure of turbulent spots; they can be measured at the leading and trailing edges of turbulent spots. Casper was unable to measure the lateral coalescence of turbulent spots. Although the perturbations did transition to young turbulent spots, they had not yet grown enough in the spanwise direction to permit the measurement of laterally merging turbulent spots in the BAM6QT. Additionally,

the turbulent spots measured by Casper were young, and may not have been fully developed.

2.4 Development of Turbulent-Spot Models of Transition

In order to design flight vehicles in the hypersonic regime, it is of great value to predict the flowfield characteristics caused by the intermittent transition process. One key concern is the ability for the structural vibration modes of a flight vehicle to be excited by the pressure fluctuations caused by the intermittent passage of turbulent spots. Zharov et al. modeled the intermittent transition process using a statistical approach in a low Reynolds number incompressible flowfield [33]. By applying measured growth rates and statistical data on the spot formation rates, a transition length was determined, and the turbulent flowfield characteristics that were calculated matched experimental data. Park and Lauchle further modeled the intermittent flowfield by adding knowledge of the pressure field within the spots [3]. By assuming that the internal pressure field of each spot could be accurately modeled by the Corcos model for turbulent boundary layers, and combining that with an experimentally developed space-time correlation for the intermittency function, Park and Lauchle were able to model the frequency-wavenumber spectrum of the intermittent flowfield. They also found that the wall pressure fluctuations were higher than under fully turbulent flows, and mentioned that the high amplitude pressure fluctuations could cause coupling with structural components. Development of a hypersonic model of turbulent spot transition would allow designers to reduce aeroelastic coupling due to the intermittent passage of turbulent spots.

3. Instrumentation and Data Processing

3.1 Boeing/AFOSR Mach 6 Quiet Tunnel

All measurements were made in the Boeing/AFOSR Mach-6 Quiet Tunnel at Purdue University, shown in Figure 3.1. The BAM6QT is one of three operational hypersonic quiet tunnels in the world. The tunnel is a Ludwieg tube design consisting of a pressurized driver tube with a converging-diverging nozzle at one end. The pressurized end of the tunnel is separated from a vacuum tank either by a set of double diaphragms or by a ball valve at the downstream end of the tunnel. To start a run, the diaphragms are burst or the ball valve is opened, causing an expansion wave to travel upstream and reflect between the upstream end of the driver tube and the contraction. Stagnation pressure and temperature remain quasi-steady between reflection cycles (approximately 200 ms) until the tunnel unstarts due to the drop in stagnation pressure. Run times are typically between 3-5 seconds depending on initial stagnation pressure. The BAM6QT is capable of an initial P_0 of 34-2070 kPa with an initial T_0 of 430 K. The current maximum quiet pressure is approximately 1190 kPa.

The BAM6QT can operate as either a conventional hypersonic tunnel or as a quiet tunnel with a laminar nozzle-wall boundary layer sustained through the test section. This is important for transition research, as noise radiated from a turbulent nozzle-wall boundary layer can lead to early transition or the growth of bypass instabilities [34]. The leading cause of freestream tunnel noise in cold hypersonic wind tunnels is the radiation of acoustic waves away from turbulent boundary layers along the nozzle wall. The BAM6QT has several design features that delay transition along the nozzle wall. The diverging portion of the nozzle was built in eight sections in order to hold the tight tolerances required for the nozzle wall contour. At the throat, there is an

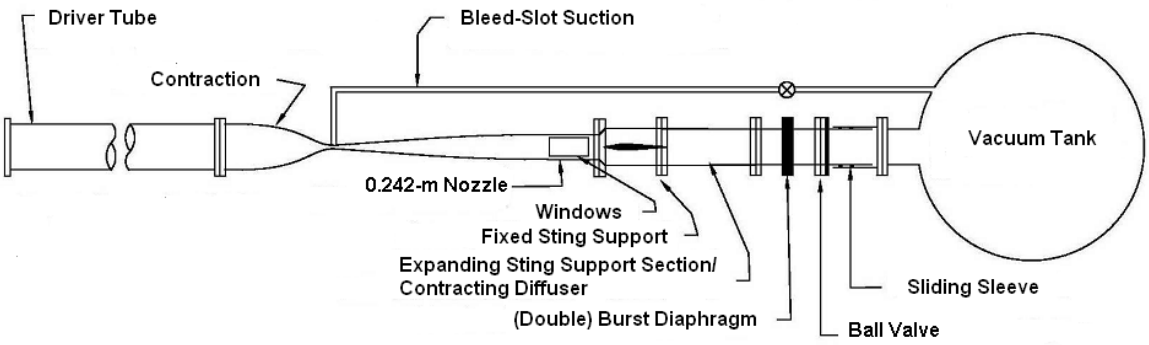

Figure 3.1. Boeing/AFOSR Mach 6 Quiet Tunnel

annular bleed slot that bypasses directly to the vacuum tank to remove the turbulent boundary layer that develops along the contraction wall. This allows a fresh laminar boundary layer to begin along the divergent portion of the nozzle. The bleed slot is opened via a fast-acting valve that is triggered when the tunnel starts. The first four sections (0.76 m) of the nozzle wall were constructed of electroformed nickel which was then polished to further reduce surface roughness. Due to the thin boundary layer near the throat, the surface finish in these sections is critical to prevent roughness-induced boundary-layer transition. The nozzle wall contour is also elongated to delay transition due to the Görtler instability. Lastly the supply air is filtered to remove particulate above 0.01 microns that could damage the nozzle-wall surface finish. By leaving the fast-valve closed during a run, the BAM6QT can operate as a conventional hypersonic tunnel. Further information regarding the design of the BAM6QT can be found in Schneider. [35]

The last 0.77 m of the nozzle act as the test section of the BAM6QT. The nozzle diameter is almost constant in this section at approximately 0.24 m. The test section also features 8 window inserts distributed in 90° intervals about the azimuth at two axial locations. These window inserts can be used to provide optical access or instrumentation. The four upstream windows are all 10 × 3.1 inches, and are

completely interchangeable, allowing for multiple configurations depending on the apparatus. The upstream inserts also feature smaller 2.5-inch-diameter inserts for mounting apparatus. The downstream set of openings contains two pairs of windows. A set of 14.1 $\times$ 4.1 inch windows are located on the top and bottom of the BAM6QT test section, and the top window features a slotted blank that can be used for instrumentation or can be removed to allow access for the traverse system. There are also two window inserts of 14.1 $\times$ 7.4 inches located on the sides of the test section that are used primarily for optical access. There are three inserts that can fit into the largest window blanks: a blank steel insert shaped to the contour of the nozzle, a large contoured plexiglass window that provides optical access and is rated to 1050 kPa, and a contoured window insert with two 5-inch portholes for use at stagnation pressures above 1050kPa.

3.1.1 Traverse System

The BAM6QT features a traverse system that allows probe measurement of the freestream flow as well as the model boundary layers. The traverse system is mounted through a 12.5 inch long slot in the top downstream window insert to allow multiple probes to be used. Both pitot and hot-wire probes have been developed for the BAM6QT, although pitot measurements were not made during this project. The traverse system connects to the probe supports via three 0.375-inch-diameter shafts that pass through a brass traverse bar. The traverse bar is positioned in the axial direction prior to pressurization, and then clamped into place to seal the tunnel. Vertical motion during a run is possible due to ball bearings that pass the probes through the tunnel wall. The two outer rods of the probe supports are solid, while the inner rod is hollow to allow instrumentation wire to pass through the tunnel wall. The center rod is sealed using a Conax fitting. Further information regarding the development of the traverse system can be found in Swanson [36].

3.1.2 Nozzle Wall Apparatus

Three of the nozzle-wall inserts were used to support instrumentation in this project. The most upstream 2.5-inch-diameter insert was modified in order to allow a passage for the perturber jet. The nozzle insert was machined with a 0.039-inch-diameter hole, located along the tunnel centerline at $z = 1.924$ m, where z is the axial distance from the throat. The atmospheric side of the insert was machined with four 10-32 tapped holes to allow the valve to be mounted. Immediately downstream of the perturber insert is a second 2.5 inch insert with a Kulite pressure transducer flush mounted at $z = 2.055$ m.

In the smaller of the two downstream nozzle-wall inserts, a contoured plug was machined to allow for additional instrumentation in the slot normally reserved for the traverse. Ten holes were drilled with varying diameters to allow a variety of sensors to be mounted along the nozzle centerline. Currently, four Kulite sensors are located in a streamwise array along the tunnel centerline at $z = 2.201, 2.302, 2.378$ and 2.480 m. The remaining holes were filled by gluing dowel pins in place using Loctite 243 Threadlocker. While the Loctite seemed to provide adequate strength, there were issues with successful sealing of the dowel pins, which led to a failure during two entries.

A cylindrical pipe insert, designed by Casper [5], is located downstream of the tunnel test section. This insert takes advantage of the laminar flow that extends downstream of the test section. The pipe insert consists of 5 separate rings with an internal diameter of 0.242 meters. The most upstream ring is designed to provide a smooth transition from the nozzle to the pipe insert. The other four rings are completely interchangeable, and have inserts for a variety of sensors. Currently three of the rings feature a single Kulite XCQ-062-15A A-screen fast-pressure sensor oriented along the tunnel centerline. The last ring consists of a spanwise array of XCQ-062-15A A-screen pressure sensors located at ± 0, 11, 21, 32, 42, and 63 mm about the azimuth.

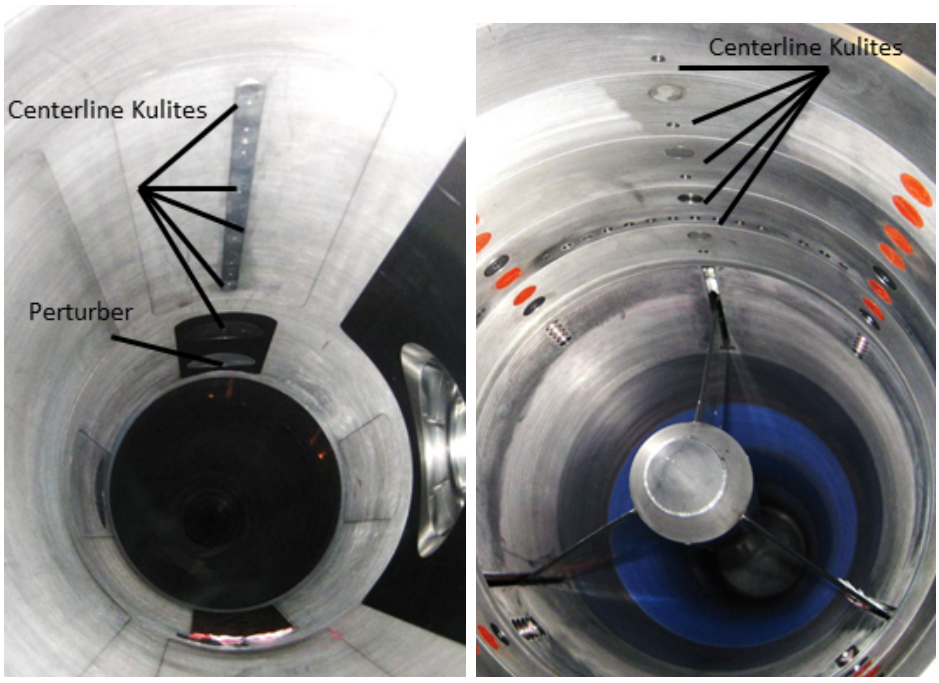

(a) (b)

Figure 3.2. Two separate views of the internal instrumentation for perturbation measurements. (a) Looking upstream towards the nozzle from the test section exit. (b) Looking downstream towards the diffuser from the test section exit.

3.2 Pulsed Jet Perturber

The perturbations studied in this project were generated using a pulsed jet perturber system. The basis of this system is a Parker Hannafin Corporation (Parker) #009-1669-900 pulse valve. Parker pulse valves are primarily used for spectroscopy experiments where pressurized specimens are injected into a vacuum chamber in order to cool the specimen via supersonic expansion. The valve provided an off-the-shelf component that was well suited to the pressure environments encountered during pressurization of the BAM6QT, as well as the low static pressures that occur during a tunnel run. A disassembled valve is shown in Figure 3.3. The valve coil threads onto the valve body with a 1/2 28-UNEF thread. Internally, the valve consists of an armature with an internal load spring holding a poppet into place. The armature

assembly is then inserted into the coil, and held into place with a buffer spring as the valve body is threaded onto the valve coil. Upon actuation of the valve, the armature is drawn back into the coil, and the poppet retracts to allow flow through a 0.039-inch exit-orifice on the stock valve. The total travel of the valve is on the order of 0.003-0.005 inches. A schematic of the two valve states is shown in Figure 3.4. In order to prepare the valve for use, the valve had to be aligned. The valve alignment was a one dimensional process by which the location of the valve coil relative to the valve body was set by threading the coil onto the body, to alter the position of the internal valve components. This process is discussed in greater detail in Section 5.4.

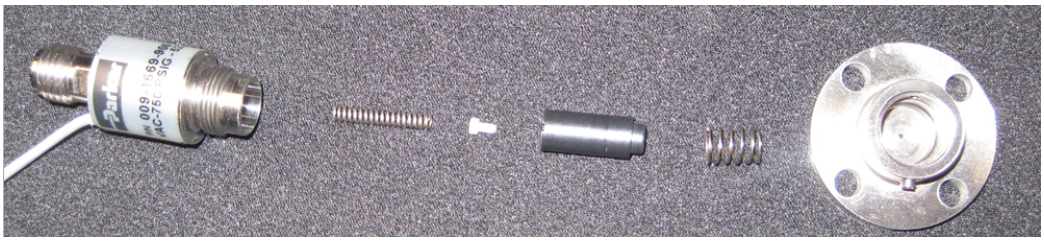

Figure 3.3. Exploded view of Parker 009-1669-900 Pulse Valve. Parts from left to right: coil, load spring, poppet, armature, buffer spring, body.

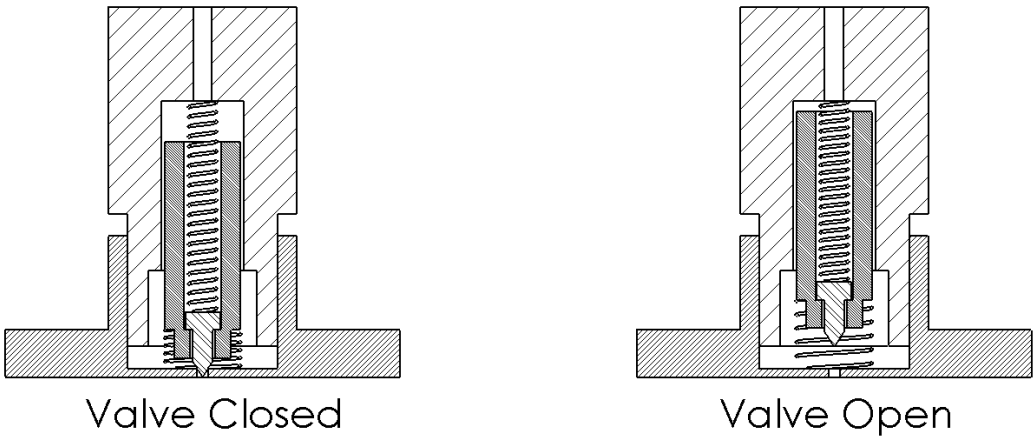

Figure 3.4. Schematic showing the internal states of the valve. Not to scale, exaggerated for clarity.

3.2.1 Valve Electronics

Two sets of electronics were used to power the valve. One set was built by the Jonathan Amy Facility for Chemical Instrumentation at Purdue University, and was generously lent to the author by the Zwier group at Purdue University during construction of a new valve driver. The second set of electronics were built by John Phillips, the AAE electronics technician, and was modified to better fit the requirements of the experiment. The valve electronics actuated the valve by supplying a short (40-100μs) pulse of 300 V DC power to the valve, to quickly retract the solenoid into the coil. Adjustments could be made to the duration of the high voltage pulse by adjusting a potentiometer on the front panel of the electronics, as shown in Figure 3.5. After this pulse a low voltage (5-8 V) pulse could be set at a determined duration to hold the valve open while eliminating the risk of overheating the coil. The maximum repetition rate of the stock electronics was 50 Hz. It was determined during initial testing with the Zwier group electronics that the low voltage holding pulse, which had a minimum duration of approximately 120 μs from the beginning of the driver signal, caused the perturbation to have a duration well above the desired length. The AAE set of electronics was modified to allow this pulse to be eliminated from the signal. The second modification performed raised the maximum repetition rate of the valve to 180 Hz, and then again to 400 Hz. The maximum repetition rate used during experimentation was 200 Hz to ensure that individual perturbations did not interfere with each other. These modifications are discussed in more detail in Section 4.2.1.

3.3 Test Cell

A previous incarnation of the BAM6QT diffuser section is currently in use as a vacuum test cell. The test cell was used extensively in the latter portion of the investigation as a tool for aligning the pulse valve, and determining minimum pulse durations. The diffuser section is capped by two 1/2 inch thick sheets of Lexan with integral o-ring grooves to provide a suitable seal required for the vacuum needed to

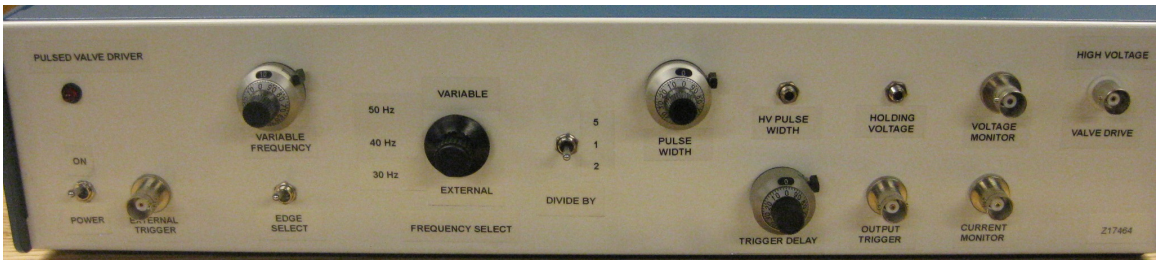

Figure 3.5. Front panel for the AAE pulse valve driver electronics built from the JAFCI plans with modifications for BAM6QT use [37].

match the static pressure of ≈0.1 psia present in the BAM6QT during a maximum quiet freestream Reynolds number of $12 \times 10^6/m$. A 1/4 inch pipe extends from the top of the test cell, connecting to three different ball valves; one ball valve is connected to the vacuum pump in room 29C to pull vacuum on the test cell, one ball valve is connected to a vacuum gage, and the last is used for venting the test cell to ambient pressure. Instrumentation wires were ran through a Conax pressure fitting mounted on the top of the test cell. Figure 3.6 shows an image of the test cell located in the downstairs portion of room 29B.

A schematic of the current test cell in operation is shown in Figure 3.7. One of the Lexan sheets was modified to allow the pulsed jet perturber to mount on the atmospheric side of the test cell. A 0.750 inch diameter hole was drilled in the test cell, with blind mounting holes for the Parker valve as well as holes for a Kulite pressure transducer to mount on the vacuum side of the test cell. In order to better mimic the operation of the perturber mounted in the BAM6QT, a 0.9 inch thick piece of aluminum stock was machined with a 0.039-inch-diameter orifice to match the thickness of the nozzle-wall insert passage. This piece was mounted between the pulse valve and the Lexan sheet to approximate the frictional losses that the perturbation may experience passing through the nozzle wall orifice. An image of the Lexan sheet with the assembled alignment apparatus is shown in Figure 3.8.

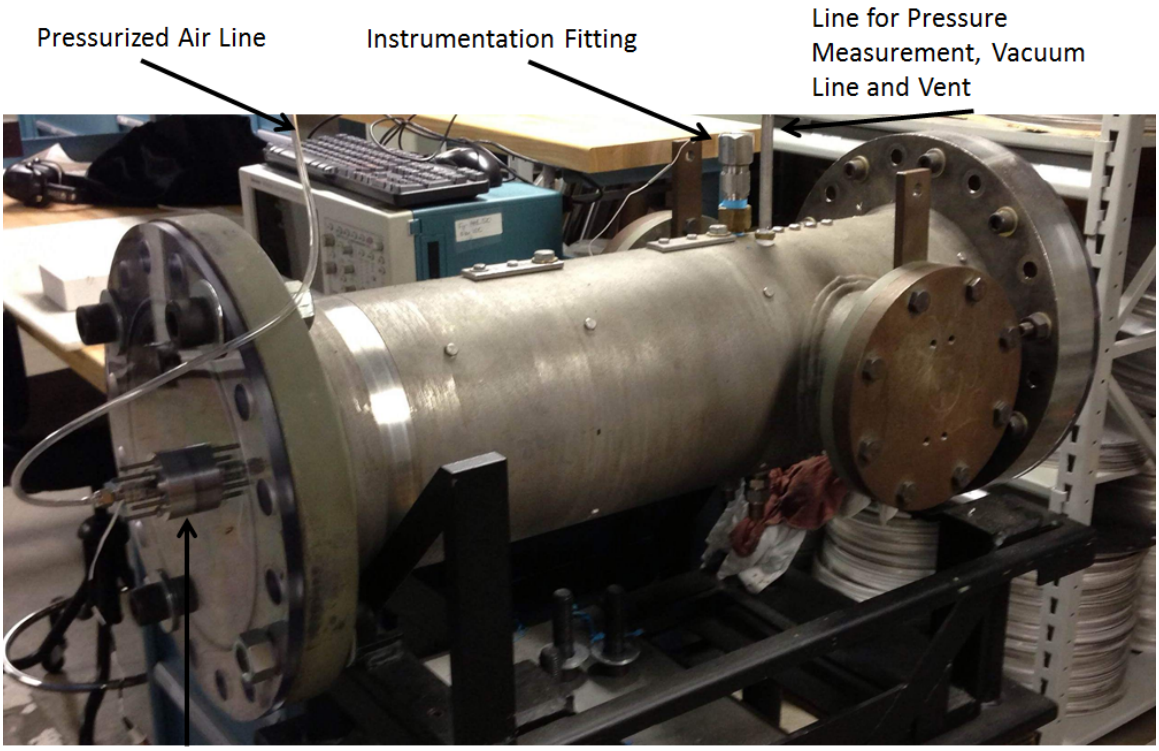

Figure 3.6. Test cell equipped for use as a valve alignment apparatus.

As the valve fires, air flows through the nozzle wall spacer and undergoes supersonic expansion. The jet then impinges directly onto the Kulite sensor mounted inside the test cell. This sensor mount is offset by a 0.020 inch spacer between the sensor mount and the acrylic flange on the vacuum side of the system. This results in an annular slot with an area of 0.047-square-inches between the sensor mount and the acrylic end flange for the injected air to flow into the main chamber of the test cell. This is an area roughly 40 times the exit area of the valve-exit orifice. The current configuration features roughly a 1/2 inch gap between the exit orifice of the injected air and the sensor. It is unclear if the existing span is optimal; with the current design, adjusting the span requires machining a new sensor mount. Future designs could include an adjustable mounting for the Kulite sensor to allow this gap to be changed on-the-fly. Detailed drawings of the valve alignment apparatus can be found in Appendix A.

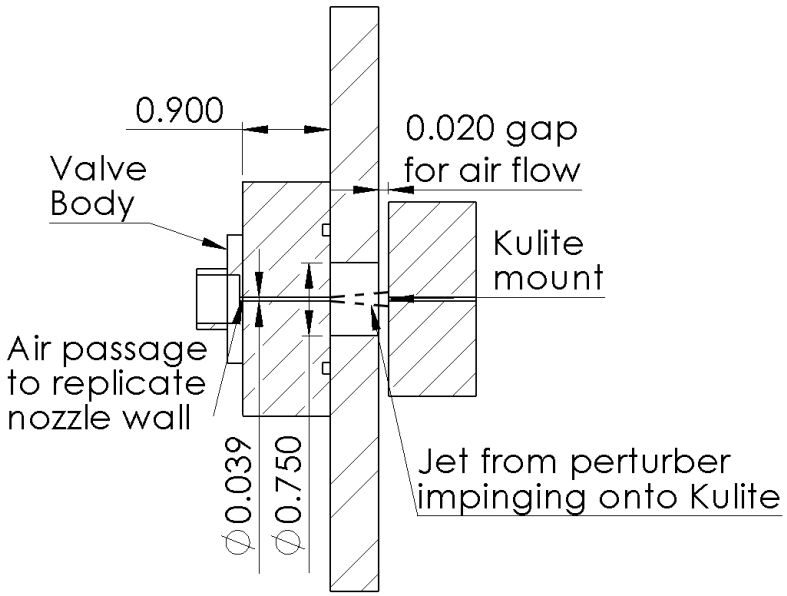

Figure 3.7. Schematic of test cell during operation.

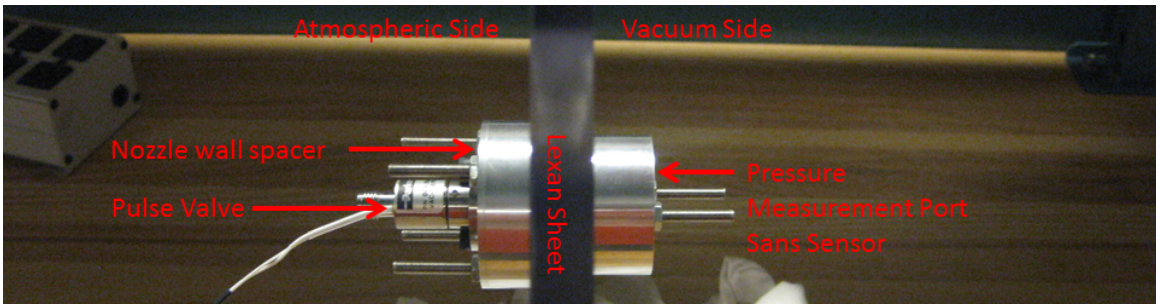

Figure 3.8. Valve alignment apparatus assembled on the acrylic test cell flange.

3.4 Pressure Transducers

3.4.1 Kulite Semiconductor Pressure Transducers

Kulite pressure transducers were used for measurement of static and stagnation pressures in the BAM6QT. The pressure transducer consists of strain gauges etched onto a silicon diaphragm in a Wheatstone bridge. The voltage output of the sensor is proportional to the pressure difference across the diaphragm. The reference side of this diaphragm is sealed with a vacuum reference pressure. Custom electronics amplify the DC output with a gain of 100. The AC signal is obtained by high-pass filtering the DC signal and amplifying again by a gain of 100 for a total gain of 10,000. The custom electronics were built in house by John Phillips, the AAE department electronics technician.

Kulite Semiconductor XCQ-062-15A pressure transducers were used for nozzle-wall pressure-fluctuation measurements. These sensors have a measurement range between 0 and 103 kPa with a resonant frequency between 225-300 kHz. Above 103 kPa, the sensors are mechanically stopped to prevent damage to the silicon diaphragm during pressurization. The sensor diaphragms on the sensors used in this experiment were protected by an A-screens which consists of a single hole surrounding the diaphragms. This allows minimal protection, but provides a flat frequency response up to 30-40% of the resonant frequency of the sensor [38]. The Kulites are statically

calibrated prior to each tunnel entry using a Paroscientific Digiquartz 740-30 portable standard with an accuracy of 0.008% of the full scale output. Once calibrated, the DC sensor output was used. Accurate static pressure measurements are difficult at the low pressures in the BAM6QT, and all pressure fluctuation measurements are normalized by the theoretical freestream static pressures given by the isentropic flow relations.

Stagnation pressures were measured in the contraction section near the driver tube using a Kulite Semiconductors XTEL-190-200A pressure transducer. The Mach number in the driver tube is very low, and as such the pressure measured by the XTEL-190-200A transducer provides a measurement of the decreasing stagnation pressure during a run. The stagnation pressure sensor was calibrated using a Paroscientific Digiquartz 740-400A digital standard, with an accuracy of 0.01% full scale. During the first tunnel run of an entry, pressurization was stopped at 10-15 psi intervals to allow calibration measurements. Another Kulite pressure transducer is used in the diffuser section of the tunnel to trigger the data acquisition system. When the flow becomes supersonic during initial tunnel startup, the static pressure in the diffuser drops suddenly. This sudden drop in static pressure can be used as a repeatable trigger for the oscilloscopes. This sensor is used simply for a qualitative trigger, and no quantitative data is collected.

3.4.2 Hot Wire Anemometry

Hot wire anemometry is well suited for the characterization of hypersonic flows due to the high frequency response and spatial resolution [39]. Hot wires operate on the principle that most metals' resistance (R) increases with temperature. When placed into a flow, convective heat transfer results in a change in the wire temperature and therefore its resistance. Hot wire anemometry takes advantage of this relation to measure various properties of the flow. Hot wires are thin wires heated by passing an electric current through them. The temperature is held constant by a controlling

circuit. A constant temperature anemometry (CTA) circuit can be seen in Figure 3.9. Resistors R_1 and R_2 are constant circuit elements, and for a 1:1 bridge ratio are equal to each other. R_3 is the control resistor, and is used to set the wire temperature. The control circuit is used to maintain a constant voltage drop across the hot wire and R_3, by varying the current. When placed into a flow, convective heat transfer will alter the hot wire resistance. The control circuitry responds by increasing the current through the wire to maintain a constant temperature. The voltage trace can be used to determine the mass flux in supersonic flows, as both density and velocity change in the flow, although only uncalibrated traces are presented in this report.

The hot wire probes were equipped with 0.0002 inch-diameter Platinum-Rhodium wire to prevent oxidation at the high wire temperatures (700-900 K) required for mass flux measurements in the BAM6QT. The hot wires were controlled by a TSI IFA-100 CTA using a 1:1 bridge ratio. The hot wire had a cold resistance of 6.9 ohms and the control resistor had a resistance of 11.6 ohms to set a resistance ratio between 1.7 and 1.9 as recommended by Rufer [40]. Several methods were used to improve the durability of the hot wires during operation, as recommended by Wheaton [41]. The anemometer was turned from standby to run mode just prior to the beginning the run, and turned back to standby as soon as the oscilloscopes loaded 5 seconds of data, to prevent the hot wire from breaking during the higher density flow encountered during the subsonic blowdown at the end of the run.

The hot wire was tuned while installed in the BAM6QT. The wire was subjected to a square-wave disturbance generated internally by the IFA-100 at atmospheric pressure with no flow. The dynamic response of the wire was monitored using an oscilloscope. The gain and cable compensation were adjusted until the hot wire responded at a high frequency with no oscillation. The response of the tuned hot wire can be seen in Figure 3.10. The time constant of the tuned wire(τ)=12 μs, leading to a frequency response of 64 kHz using Equation 3.1 given by Spina and McGinley [39]. The hot wires used in this experiment are thicker than traditional wires used in hypersonic flowfields due to durability issues encountered by Rufer [40].

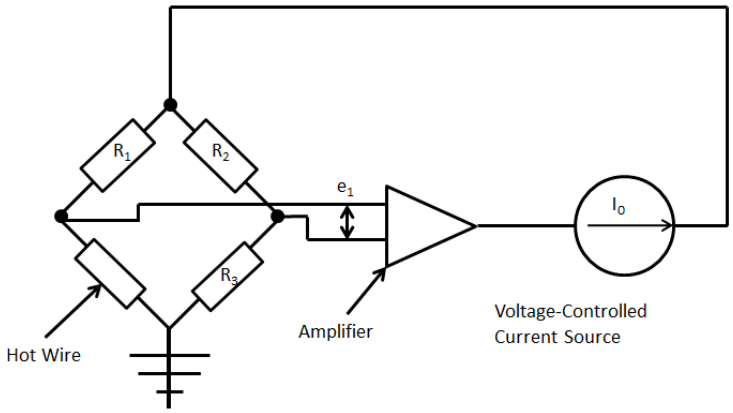

Figure 3.9. Constant temperature anemometer control circuit, redrawn from Reference 39.

The larger wire proved more durable, but at expense of the frequency response. The thicker wire provided ten runs without breakage, and the frequency response was still high enough to measure the frequencies of interest within the nozzle-wall boundary layer.

$$f = \frac{1}{1.3\tau} \tag{3.1}$$

3.4.3 Hot Wire Probe Support

Hot-wire measurements were made using the BAM6QT traverse system. Due to the thickness of the nozzle-wall boundary layer, special 51-mm-long probe struts were designed by Wheaton to reduce the effect of probe interference [41] as shown in Figure 3.11. An angled brass probe strut with a 2×0.375 inch double-wedge cross section (Figure 3.12) was used to hold the hot wire within the tunnel. The probe strut consists of a 4.250-inch straight section that descends through the traverse slot attached to a 5.000-inch section that is angled at 62° upstream allowing the probe to measure approximately 9.5 inches further upstream than the straight probe. The hot wire probe was positioned using the BAM6QT traverse system. The axial location of

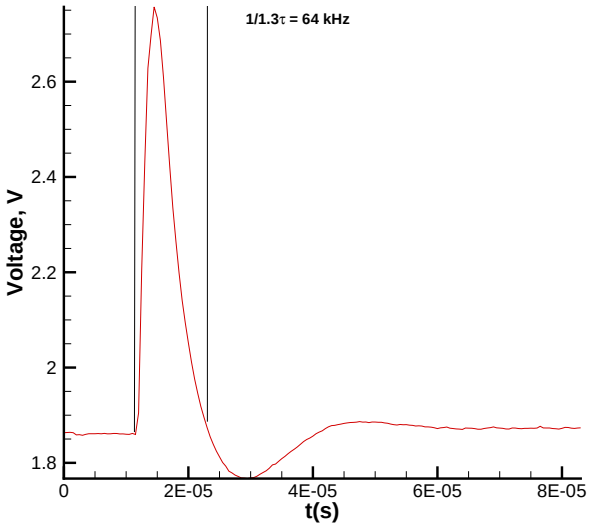

Figure 3.10. Tuned hot wire response to a square wave input in the BAM6QT at atmospheric pressure with no flow.

the probe within the tunnel was determined through the use of the traverse ruler. The vertical location relative to the nozzle wall was determined using a set of gage blocks as reference datums. The traverse was lowered to the desired position, and the gage blocks were slid underneath the probe until they just touched the bottom rear edge of the probe. Using knowledge of the probe and tunnel geometry, both the radial and axial location of the traverse probe could be determined using a MATLAB program written by Wheaton [41]. Hot wire measurements were made along the bottom of the nozzle wall at an axial location of $z = 1.955$ m and a distance y=1.9 mm above the wall. This positioned the hot wire within the boundary layer, 0.031 m downstream of the perturber.

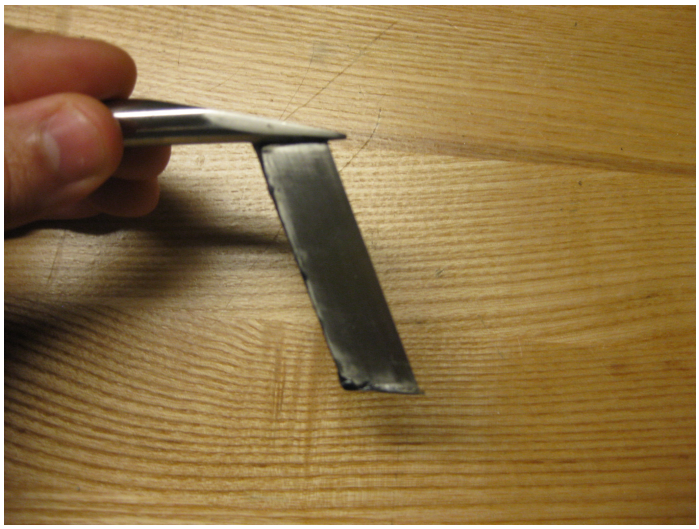

Figure 3.11. 51 mm hot-wire probe used to measure inside the nozzle wall boundary layer. Schematics can be found in [41].

Figure 3.12. Angled traverse probe strut for measuring along the bottom wall of the BAM6QT. Schematics can be found in [41].

3.5 Data Processing

All data were recorded using Tektronix oscilloscopes, including a TDS7104, DPO7104, two TDS5034B and one DPO7054 Digital Phosphor Oscilloscopes. Data was typically sampled at 1MS/s in Hi-Res mode. Hi-Res mode is used to increase the vertical

resolution of the oscilloscopes from 8 bits to above 12 by sampling the data at the maximum sampling rate of the scope (1.25-5 GS/s) and averaging in real time to the desired sampling rate. Kulite data were digitally low-pass filtered at 175 kHz using an 8th order Butterworth filter within MATLAB to remove sensor resonance.

Individual perturbations were extracted from the pressure data by use of the triggering signal. Initially, 100 samples were taken sequentially within a 0.5 second portion of the run approximately one second after the perturber began firing. Each sample was 3-ms in order to fully capture the perturbation at each axial location. In order to eliminate perturbations contaminated by naturally occuring spots, or valve misfires, two criterion were applied to the pressure traces from the Kulite XCQ-062-15A located at $z = 2.831$ m. Samples which had local RMS levels above 0.01% of p_∞ prior to the passage of the perturbation were eliminated from the data set. This removed any perturbations that were contaminated by the presence of a naturally occurring turbulent spot. Additionally, any perturbations where the RMS fluctuation levels exceed 0.15% of p_∞ behind the perturbation were removed from the data set to remove any samples contaminated by flow disturbances that occur after the perturbation. This was often seen as a large deviation from the expected mean static pressure downstream of the perturbation. The cause for the deviations are unclear, but resulted in a data sample that was categorically different from the bulk of the perturbations. The threshold was higher behind the perturbation due to the presence of second mode waves in the calmed region. The incidence of disturbances behind the perturbation was much lower than the incidence of naturally occurring turbulent spots. Once the rejected samples were eliminated from the data set, the data set was further reduced. The first 50 of the remaining samples were further analyzed to provide a consistent sample size. The 50 individual perturbations were then ensemble averaged to give a representative perturbation. Figure 3.13 shows examples of each elimination criterion.

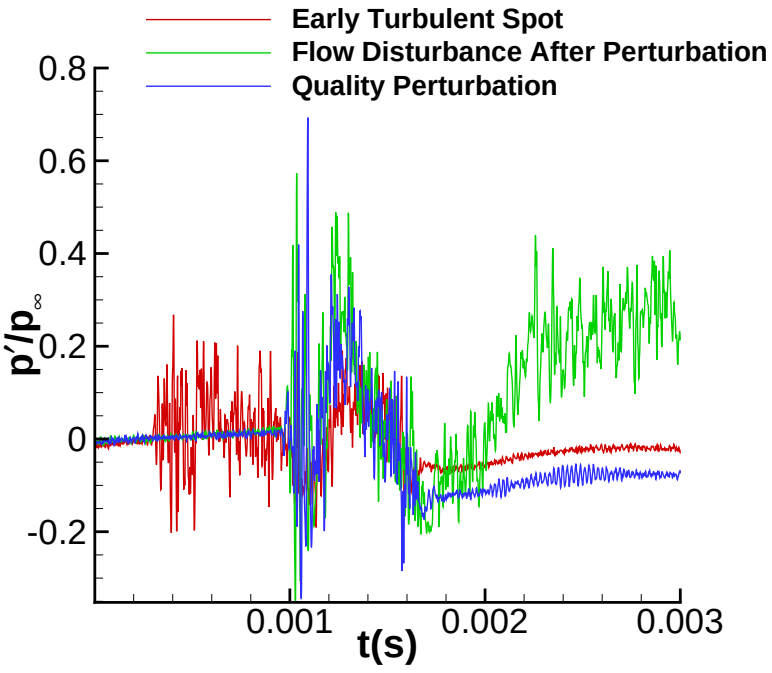

Figure 3.13. Examples of perturbations eliminated using RMS criterion.

3.5.1 Perturbation Detection Method

The method of Hedley and Keffer was used to determine the leading and trailing edge of the perturbations [43]. In order to accomplish this, the ensemble averaged pressure traces were conditioned to form a detector function. The resulting trace, D, is then smoothed using a moving average to eliminate any zeros that would otherwise be interpreted as the end of the perturbation, generating the criterion function S. Once this process is carried out, the criterion function is compared to an adjustable threshold to determine the state of the flow. This process was used generally for determining the presence of turbulence, but was also used by Casper to determine the duration and convection rates of instability wave packets in the BAM6QT [5]. The process used herein is the same one used by Casper.

Equations 3.2 and 3.3 are used to generate the detector function, formed by the product of the magnitude of the signal and the square of the first derivative computed

using a central-difference scheme. This product emphasizes the high frequency components of the signal that one would expect to see during a turbulent perturbation. The detector function is then smoothed using an exponentially weighted moving average over 24 sampling periods ($\tau_s = 24\Delta t$), modified from Ching and LaGraff [44], given in Equations 3.4 and 3.5.

$$m(t) = \left| \frac{p(t) - p_{min}}{p_{max} - p_{min}} \right| \tag{3.2}$$

$$D(t) = m(t) \left(\frac{\partial p(t)}{\partial t} \right)^2 \tag{3.3}$$

$$S(t) = \frac{(\Delta t)^2}{1 + \tau_s/\Delta t} \sum_{j=i+(\tau_s/2\Delta t)}^{j=i-(\tau_s/2\Delta t)} \omega_j D(j\Delta t) \tag{3.4}$$

$$\omega = exp\left[- \left(\frac{.625}{\tau_s/\Delta t} \right) |j - i| \right] \tag{3.5}$$

Once calculated, the criterion function (Eq. 3.4) was logically compared to a threshold level to determine the points at which the perturbations began and ended. A threshold level of 0.001 p_∞ was used to determine the onset of perturbations. Determining the end of the perturbation proved more difficult due to the turbulent nature of the perturbations, and the slow decay of the perturbations. The trailing edge threshold level was adjusted several times without a noticeable increase in accuracy, so a level of 0.001 p_∞ was used here as well. A sample of this process is shown in Figure 3.14. Once the leading and trailing edges of each perturbation were determined, the convection velocity could be determined.

3.5.2 Power Spectral Density Calculation

For each run, the power spectral density (PSD) was calculated at each measurement location. The fast Fourier transform (FFT) was taken for each 3-ms pressure trace. The resulting FFT's were then averaged to give the PSD at each sensor location. By ensemble averaging the FFT's of each individual trace, a representation

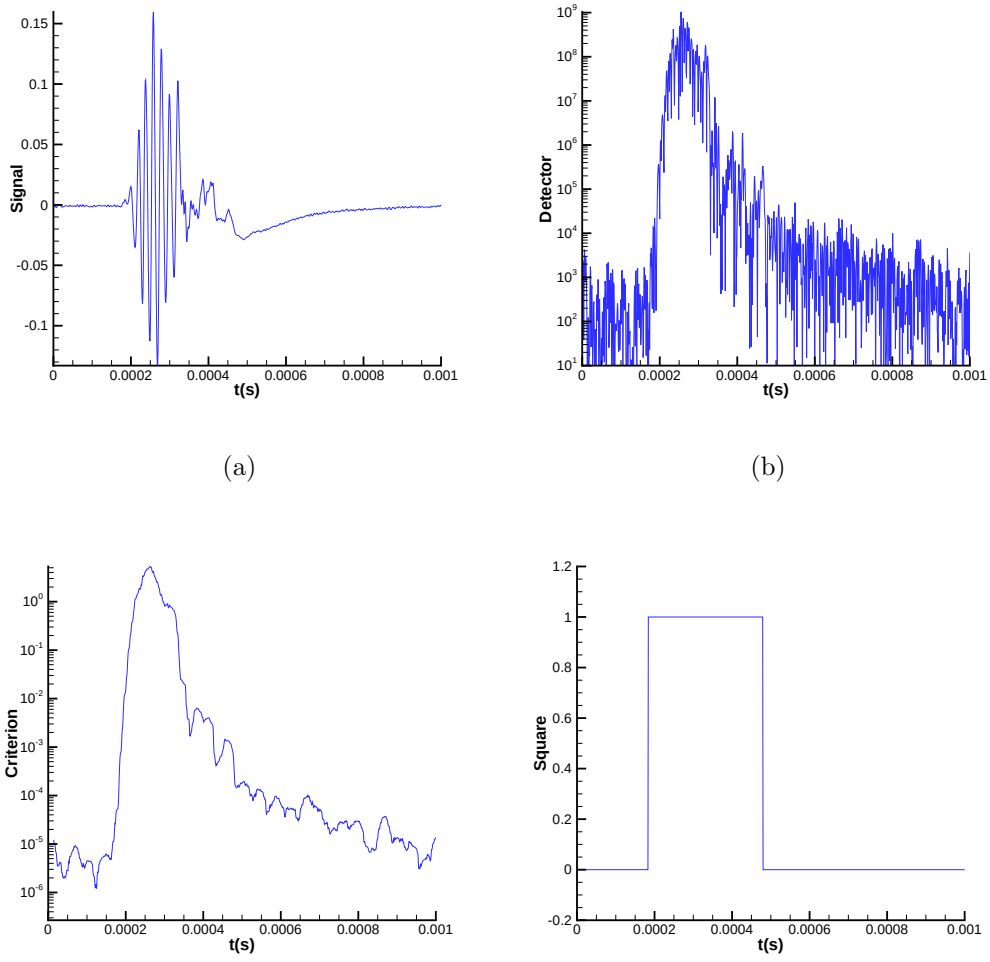

(a) (b)

(c) (d)

Figure 3.14. General process for perturbation duration detection. (a) Ensemble averaged pressure signal at $z = 2.201$ m (b) Detector function output (c) Criterion function output (d) Square wave signaling the duration of the perturbation.

of the average frequency content at each sensor is produced. This is qualitatively different than taking the FFT of the ensemble averaged pressure traces. Due to the turbulent nature of the perturbations, the pressure fluctuations are not in phase. Ensemble averaging the individual pressure traces averages out the pressure fluctuations if they are not in phase. If the FFT is taken of the ensemble averaged trace, this results in a loss of frequency content present in the individual traces.

4. Perturber Modifications

Initial testing of the pulsed jet perturber was conducted in the BAM6QT during week-long tunnel entries in October 2012 and February 2013 using the traverse plug sensors as well as the instrumented pipe insert. Additional measurements were made using hot-wire anemometry in March 2013. In July 2013 the perturber alignment apparatus was briefly evaluated using the instrumented pipe insert and the upstream instrumented nozzle-wall insert. During the July 2013 entry the seal on some of the glued-in dowel pins failed on the instrumented traverse plug, and a blank traverse plug was inserted in its place, resulting in an absence of data at $z = 2.201, 2.302, 2.378$ and 2.480 m. All the pressure traces presented in this report are offset proportionally to their distance downstream.

4.1 Alignment Procedure

Prior to each run in which the pulse valve poppet was changed, the valve had to be realigned. In order to change the poppet, the valve had to be completely disassembled and reassembled. The valve was reassembled with significant travel left in the threads that attach the valve body to the coil in order to allow for a gross alignment of the valve. Once assembled, the air supply could be connected, and the valve stagnation pressure could be set using a pressure regulator. The valve driving electronics were then turned on, and gross adjustment of the valve was accomplished by tightening the body onto the coil until pulses of air could be felt escaping the valve during operation. Valve response was then fine tuned by adjusting the valve body and high voltage driver signal until a pulse could be consistently felt by covering the valve orifice with the author's index finger, and subjectively judging the intensity of the pulse. An attempt was made to produce the shortest possible perturbations

using this tactile method by adjusting the valve to one extreme of travel or the other. Once the minimum pulse intensity was reached by adjusting the valve body, the high voltage driving pulse was turned down incrementally, and the valve body position was further refined. This process was repeated until no more significant reductions in the finger-tip-detected impulse were made by further adjustment, or until the valve ceased to operate. Typical high voltage pulse durations were on the order of 70-80 μs as measured from the voltage out signal on the valve driver. This method of alignment was subjective, and the difficulty was further compounded by the shimming method used to hold the valve in place once adjusted.

Once the initial valve alignment was completed, feeler gages were used to determine the spacing between the valve body and the coil. The valve was disassembled to allow shims to be placed between the valve and coil to set the valve position, and reassembled. This method was very time consuming, and proved inconsistent, as the reassembled valve sometimes behaved differently due to shifts in the internal valve components. Eventually, the annular shims designed to be inserted between the valve coil and body were replaced with motor mount shims. The slotted motor mount shims eliminated the need to completely disassemble the valve during alignment. The motor mount shims were further made obsolete by the addition of 4-40 set screws on the valve body which allowed the valve valve alignment to be set without disassembling the valve. Improvements to this alignment procedure are discussed in Chapter 5. Once the valve was fully aligned, it was attached to the nozzle wall insert. Figure 4.1 shows samples of each method.

There were two large difficulties that occurred when aligning the valve. Assembly of the valve is accomplished by threading the valve body onto the valve coil using a 1/2-28 UNEF thread. A cutaway schematic of the valve can be seen in Figure 4.2. Aligning the valve requires balancing two forces operating internally in the valve. As the coil is threaded onto the body, the load spring will hold the poppet sealing face against the exit orifice, while the buffer spring holds the armature in contact with the poppet. During this process, the armature is being moved further within the

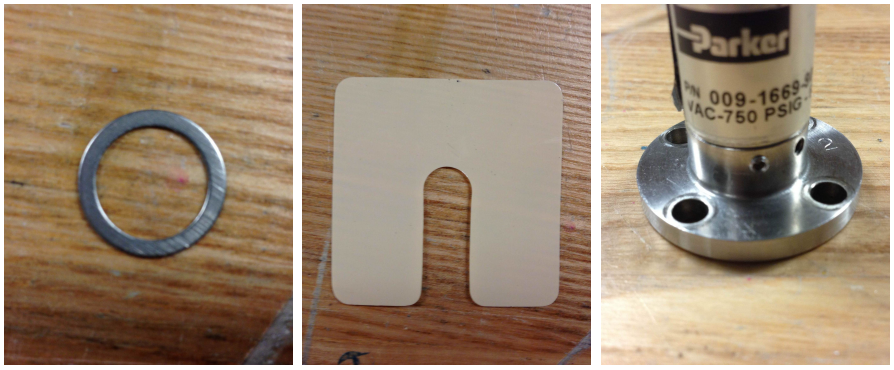

(a) (b) (c)

Figure 4.1. Objects used to set alignment. (a) Annular shims. (b) Slotted motor mount shims. (c) Set screw.

field generated by the solenoid coil. At a certain point, the impulse supplied to the armature by the driving signal will cause the solenoid will overcome the load spring, and the valve will fire. As the coil continues to thread onto the body, the armature travel will become constrained by the internal faces of the body and coil, reducing the duration and intensity of the jet. Eventually, the armature will be fully constrained by the internal cavity, and the valve will cease to fire. Aligning the valve requires finding an intermediate position where the valve fires with a jet that is sufficient in both intensity and duration.

Due to the coarse thread pitch relative to the total travel of the valve, the adjustment process goes from one extreme to the other in approximately 30 degrees of rotation. This makes maintaining accurate alignment difficult, as a slight shift in rotation can alter the valve performance. Additionally, there is some slop expected in any threaded system, leading to additional variance. Care must be taken when tightening the set screws to maintain the valve alignment, as this process has been shown to change the performance of the valve.

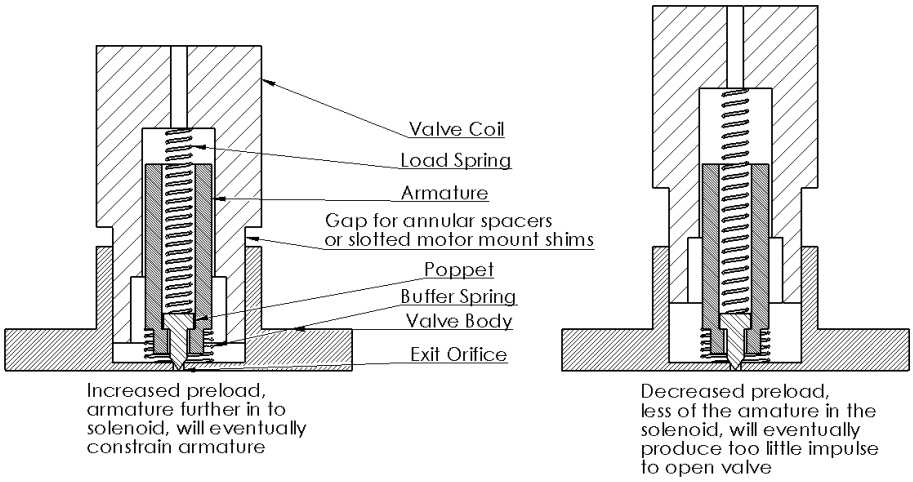

Figure 4.2. Cutaway schematic of the internals of the Parker pulse valve.

4.2 Perturbations generated by the stock valve

A perturbation produced by the stock valve using the JAFCI valve-driver electronics borrowed from the Zwier group is shown in Figures 4.3 and 4.4. An ensemble averaged perturbation and a single sample are shown along with the PSD of the perturbation. The ensemble average is an accurate representation of the mean static pressure of the perturbation, but does not portray the fluctuation amplitude well due to the turbulent nature of the perturbation which causes the fluctuations to average out of the ensemble. The perturbation was generated at $Re = 11.4 \times 10^6$/m with a valve stagnation pressure of $p_{0v} = 80$ psig. At $z = 2.201$ m the perturbation had a duration of approximately 1.5 ms.

The spectra indicate a turbulent perturbation, with large levels of broadband noise. This is very promising, as Casper's glow perturber was only capable of producing instability wave packets [5]. Near the maximum quiet freestream Reynolds numbers in the BAM6QT, the instability wave packets generated by Casper would transition to young turbulent spots towards the end of the measurement range. The fact that the perturbations shown here are fully turbulent by the first sensor location

at $z = 2.201$ m is a large step forward in the effort to measure mature turbulent spots. However, further refinement of the perturbations is necessary.

The two sensors at $z = 2.781$ and 2.831 m show an increase in frequency content below 50 kHz, although the cause of this is unknown. A possible explanation is that the large perturbation generated with this configuration was a successful turbulent perturbation contaminated by a leaking jet caused by the low voltage holding pulse. Unfortunately, the sample duration is much longer than the 10-100 μs desired. At over one millisecond in duration, the perturbation would be over 1 m in length at the velocities in the BAM6QT. Due to the relatively long duration, it seems that the measured pressure traces are the result of a quasi-steady flowfield generated by a transverse jet, as opposed to a true turbulent spot. In order to be confident that the perturbations generated by the pulsed valve are true turbulent spots, a reduction in duration is essential.

4.2.1 Driver Modifications

The effect of the driver signal on the perturbations was determined over the course of multiple runs during the entries in October 2012 and February 2013. The pulse valve is designed to be driven by a 28 V control signal under normal operating conditions. However, Parker also recommends the valve for pulse valve duty by driving the valve with a brief 320 V signal ranging in duration from a few microseconds to a few hundred microseconds [45]. This over-voltage signal causes the valve to open rapidly, on the order of a few microseconds. Once the valve is open, the driver keeps the valve open with a 5-8 V signal. Once the driver signal is complete, the voltage is reduced to approximately -23 V to prevent the solenoid from ringing. A sample driver signal can be seen in Figure 4.5.

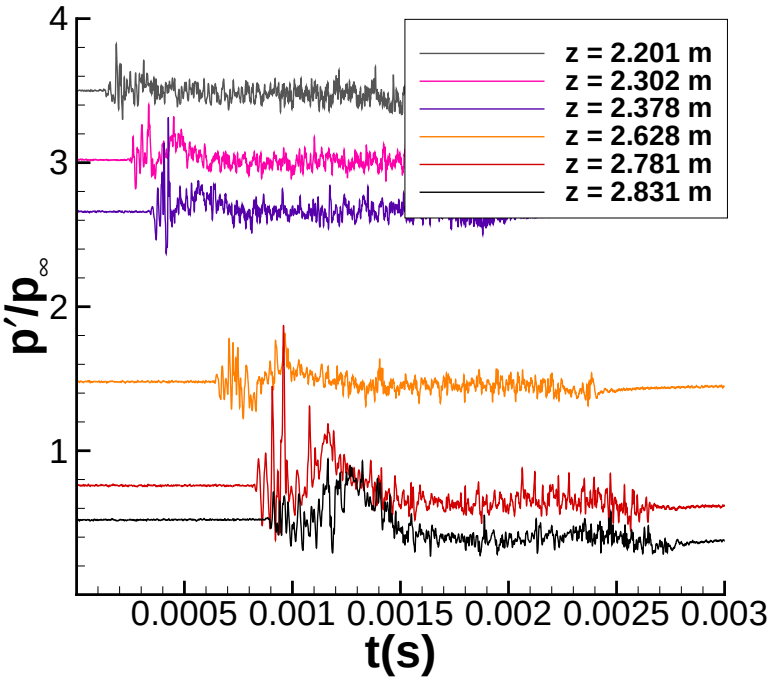

(a) Single sample

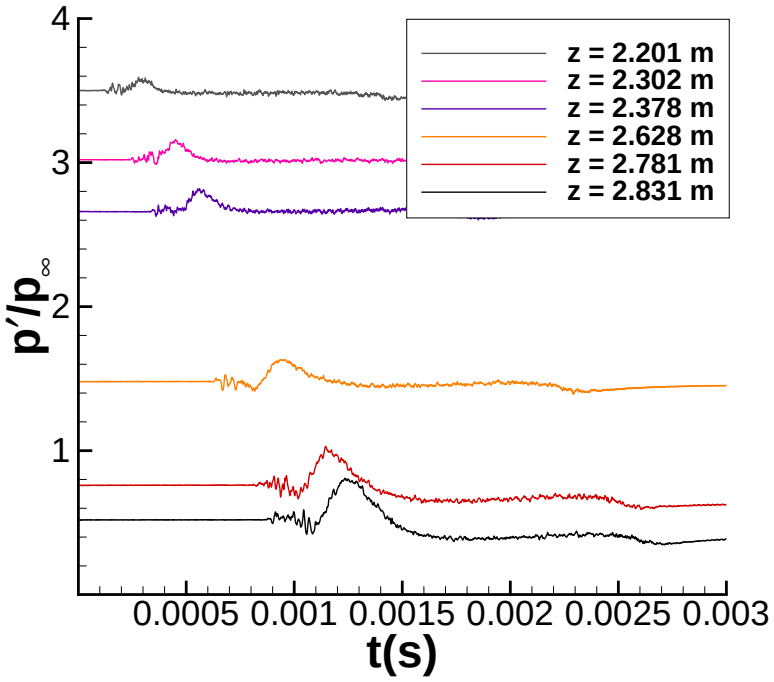

(b) Ensemble average

Figure 4.3. Perturbation produced by the stock valve with the stock JAFCI valve driver. $Re = 11.4 \times 10^6/\text{m}$, $p_{0v} = 80$ psig

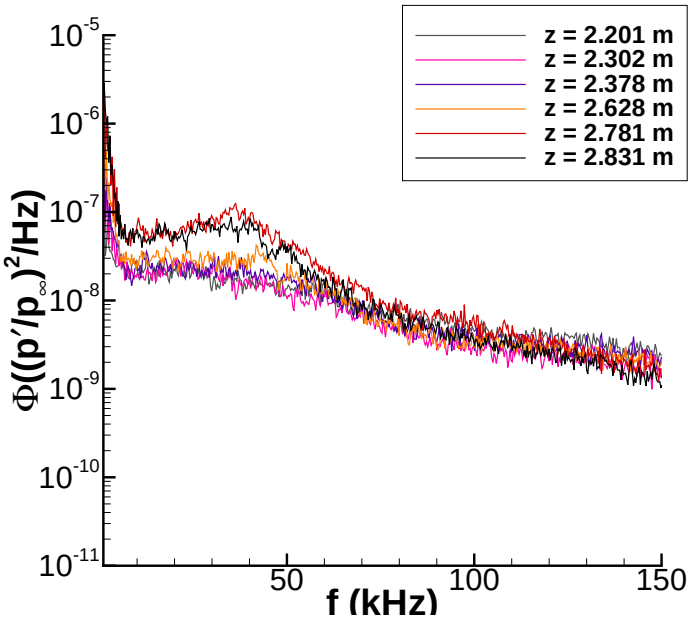

Figure 4.4. Power spectral density for perturbations generated using the stock valve with the JAFCI valve driver. $Re = 11.4 \times 10^6/\text{m}$, $p_{0v} = 80$ psig.

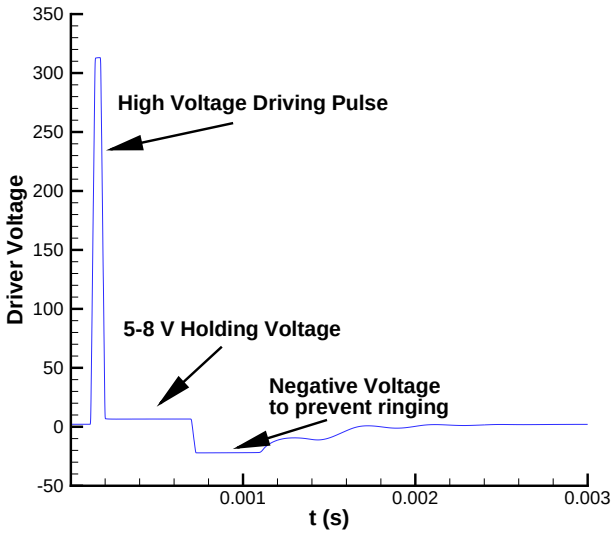

Figure 4.5. Sample driver signal generated by the JAFCI driver, measured from the 'voltage out' on the front panel.

4.2.2 Low Voltage Pulse

All of the measurements made during the October 2012 entry were limited by the presence of the 5-8 V signal which held the valve open and produced extremely long perturbations. The timing circuit shown in Figure 4.6 is the same for both the high and low voltage sections of the circuit board, differing only in the value of the capacitor C_1. When a trigger signal is received by the integrated circuit (IC) responsible for controlling the pulse width, it starts the driving pulse and shorts C_1. Once the capacitor recharges to the IC threshold level, the pulse ends. The IC used in the driver electronics requires a 1.4 kΩ resistance at a minimum, setting the minimum circuit time constant. Component values are listed in Table 4.1. In the low voltage circuit, the time constant set by C_1 and R_1 resulted in a minimum theoretical low voltage pulse duration given by

$$t_w = ln(2)C_1R_1 \approx 0.7C_1R_1 \tag{4.1}$$

which corresponds to approximately $150\mu s$ with the linear potentiometer (R_2) turned all the way down. The low voltage pulse was found to be a limiting factor in the operation of the pulse valve, resulting in extended duration perturbations. In order to alleviate this problem a new driver was built by John Phillips, the AAE electronics technician. During construction, the value of C_1 in the low voltage timing circuit was changed to match the high voltage timing circuit, giving a new minimum pulse duration (t_w) of approximately 320 ns. This allowed the low voltage pulse to be fully eliminated from the driving signal by reducing its duration to less than the duration of the high voltage pulse.

The effects of the low voltage pulse width can be seen in Figure 4.7. Both samples are taken from runs with a $Re \approx 11.5 \times 10^6$/m using the stock poppets for the pulse valve. The AAE driver produces a much steeper high voltage driving pulse, resulting in a longer overall high voltage signal, and yet the perturbation is shorter by approximately 300 μs. The effect of the low voltage pulse was to hold the valve open far longer than required for turbulent spot generation. Since a primary goal is

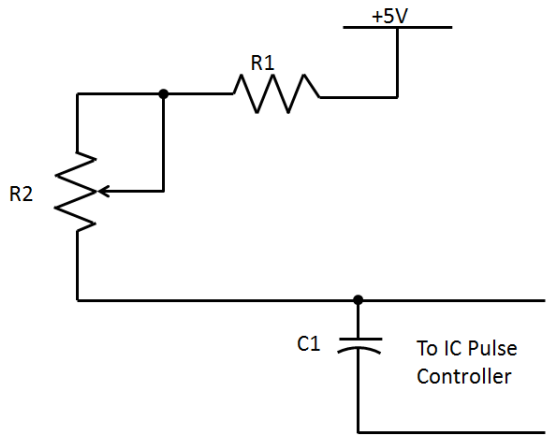

Figure 4.6. High and low voltage timing circuit feeding into pulse generating circuits, redrawn from [37]

Table 4.1 Timing circuit component values

Component	Low Voltage Circuit Value	High Voltage Circuit Value
R_1	1.4 kΩ	1.4 kΩ
R_2	100 kΩ Linear Potentiometer	100 kΩ Linear Potentiometer
C_1	0.15 μf Capacitor	3.3 nf Capacitor

to produce as short of a perturbation as possible, all of the following data presented were collected using the AAE built valve driver with the low voltage pulse turned all the way down, unless otherwise noted.

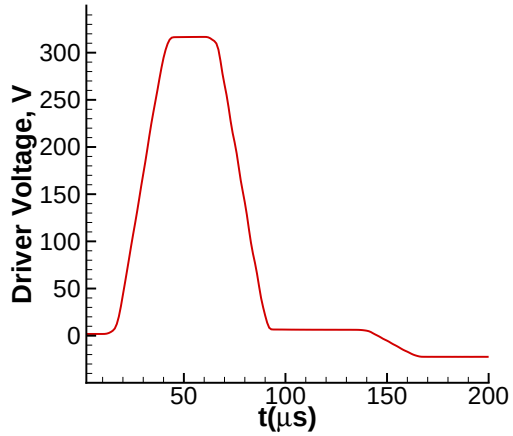

(a) JAFCI Driver Signal

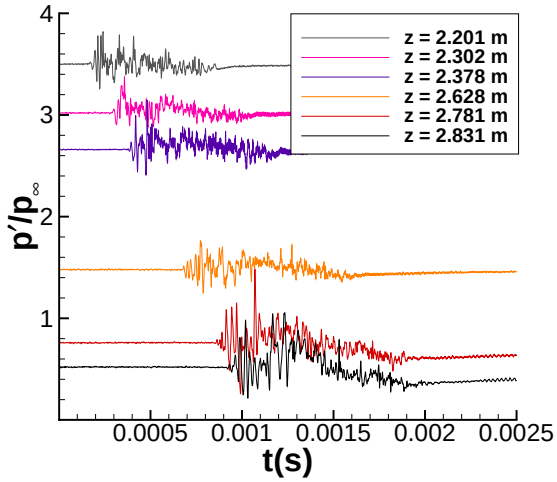

(b) Perturbation from the JAFCI driver.

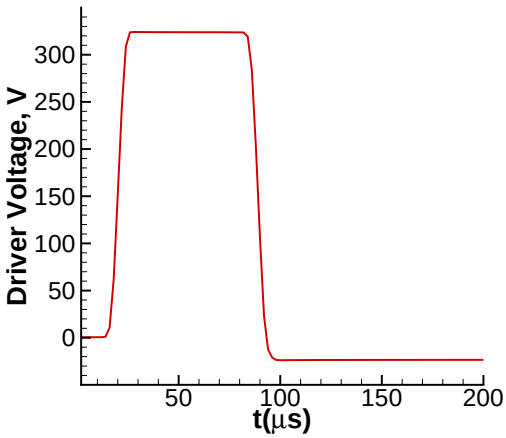

(c) AAE driver signal

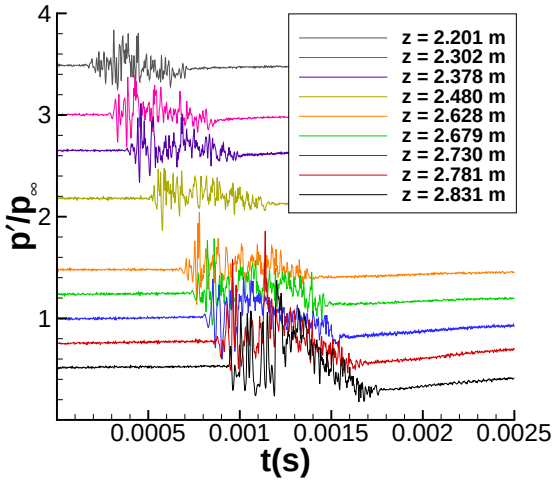

(d) Perturbation from the AAE driver.

Figure 4.7. Comparison of two different pulsed valve drivers. $Re \approx 11.5 \times 10^6/\text{m}$, $p_{0v} = 80$ psig with stock poppet.

4.3 Poppet Modifications

Even with the low voltage pulse eliminated from the valve driver signal, the perturbations still had a duration of well over 100 μs. In an effort to further reduce the disturbance duration, physical modifications were made to the valve. The most easily modified pieces of the valve were the internal poppets and the valve exit orifice. These modifications were performed in an effort to alter the mass flow through the valve orifice through a reduction in the exit area of the valve. Two approaches were used on the poppets. The first, shown in Figure 4.8 was to add an additional 0.038-inch diameter cylindrical face to the valve poppet. This face would result in the poppet countersinking within the exit orifice. As the valve armature retracted, the poppet would remain countersunk in the orifice until the end of the travel, reducing the effective total travel of the valve. By reducing the effective travel, it was hoped that the total valve open time would be reduced while still maintaining a perturbation strong enough to generate turbulent spots.

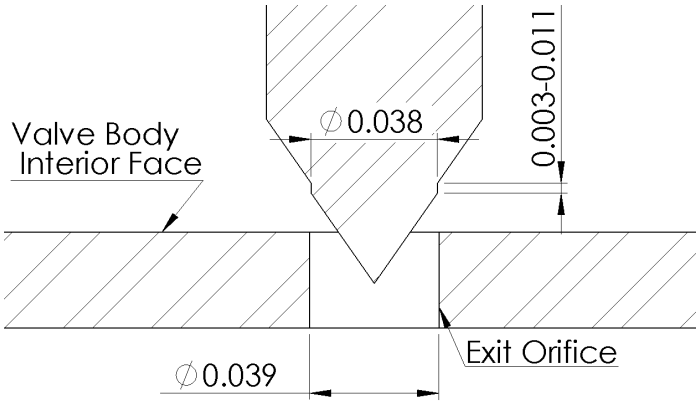

Figure 4.8. Poppet with additional 0.038-inch-diameter cylindrical face

Several different poppets were made by Robin Snodgrass of the ASL machine shop with flat depths ranging from 0.003 inches to 0.011 inches. The depths were quoted with a tolerance of ± 0.001 inch. Machining the poppets proved difficult due to the deflection of the plastic when the cutting tool was brought to the part. As a result, a

few of the poppets did not work once modified and either leaked or would not unseal during operation.

4.3.1 Perturbation measurements along the tunnel centerline

Figures 4.9 through 4.20 show the perturbations generated by several different poppet configurations, including ensemble averaged pressure traces, individual samples, and the power spectral density of the perturbations. In these figures, t = 0 s corresponds to the beginning of the trigger signal. Poppet face lengths were varied from 0.000 (stock) to 0.011 inches. All runs were made with a nominal $p_{0i} = 176$ psia and $p_{0v} = 80$ psig using the AAE valve electronics.

Care should be taken when interpreting the data presented. The primary difficulty in operating the pulsed jet perturber was achieving a consistent alignment whenever the valve had to be disassembled. Each of the different poppet configurations tested required the pulsed valve to be completely disassembled in order to change out the poppet. Any differences in the data could be due to this difficulty in aligning the valve. Additionally, a single perturber configuration was never tested in back-to-back runs at the same tunnel conditions. This was a result of never fully refining the perturbations to a sufficiently short duration. Time was instead spent trying to improve the response of the perturber. It is therefore desired that one of the first things measured in future is the multiple run repeatability. It was hoped to determine how repeatably the valve could be realigned. This was not pursued due to the lack of an objective method of valve alignment. Development of such a method is discussed in Section 5.4, but the alignment sensor failed prior to the realignment tests.

Figures 4.9 and 4.10 show the perturbation and spectra resulting from the stock valve configuration. The ensemble average perturbation shows a slight increase in the static pressure within the perturbation which rolls off back to static levels as the perturbation ends for sensors located at $z = 2.201 - 2.480$ m. As the disturbances convect downstream to $z = 2.628 - 2.831$ m, the static pressure rise increases in

magnitude, but is delayed in its onset within the perturbation. Additionally the local static pressure at the trailing edge drops below the undisturbed levels at the downstream sensor locations. Once the perturbation is past, the static pressure slowly returns to the undisturbed level. The individual sample shows the level of fluctuations that are averaged out of the signal. The PSD of this sample shows the typical turbulent spectra as seen by Casper, with broadband noise that begins to roll off around 50 kHz [5].

Figures 4.11 and 4.12 show the perturbation generated with the valve equipped with a 0.003-inch flat on the poppet poppet. The perturbation is similar to the one generated using the stock valve. Figure 4.13 shows the PSD of a 1-ms-duration sample immediately following the trailing edge of the perturbations seen in Figures 4.9 and 4.11. Spectral peaks occur at approximately 45 kHz in the stock poppet case, and grow as the perturbation convects downstream. These frequencies correspond to second mode wave growth in the calmed region behind the perturbation, and are typical for the perturbations generated at the maximum quiet Reynolds number. The second mode waves trailing the perturbation generated with the 0.003 inch face poppet are almost an order of magnitude weaker, and feature a much broader peak from 40-50 kHz, although the reason for this is unclear.

The perturbations generated using the 0.005 inch poppet (Figures 4.14 and 4.15) show evidence that the perturbation could have been an instability wave packet upstream of the sensors. At $z = 2.201$ m in Figure 4.15, the spectra shows a peak from 50-60 kHz. The pressure traces at $z = 2.201$ m are the first to show a wave packet that is not smoothed by ensemble averaging. This implies that the wave packet has yet to fully break down to turbulence. The perturbation could be experiencing the late stages of transition at this location. Towards the late stage of transition in the instability wave packets generated by Casper, broadband noise rose rapidly to the level of the the spectral peak caused by the second-mode wave packets. It is possible that the perturbation is in this stage at the first sensor location. By $z = 2.302$ m, the spectra indicate that the perturbation is turbulent.

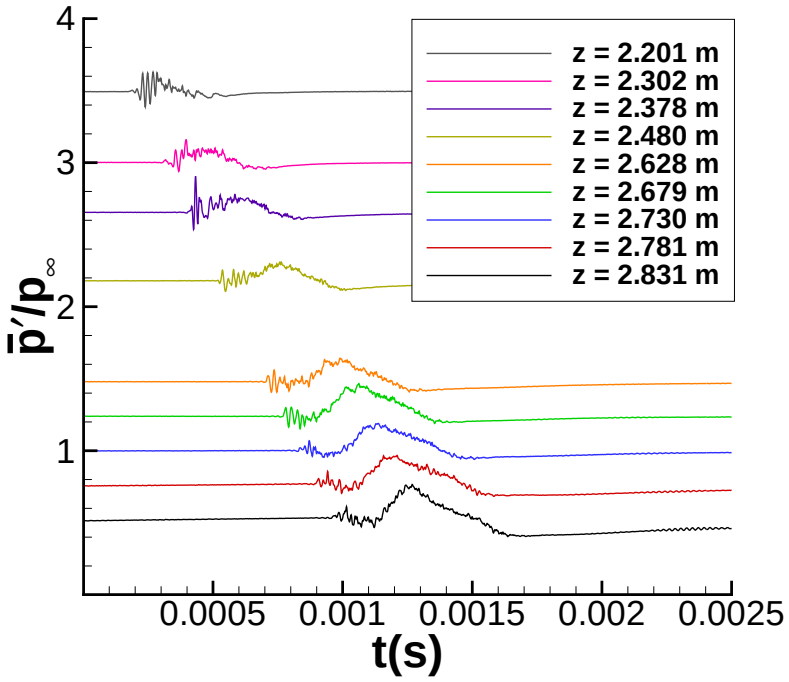

(a) Ensemble average

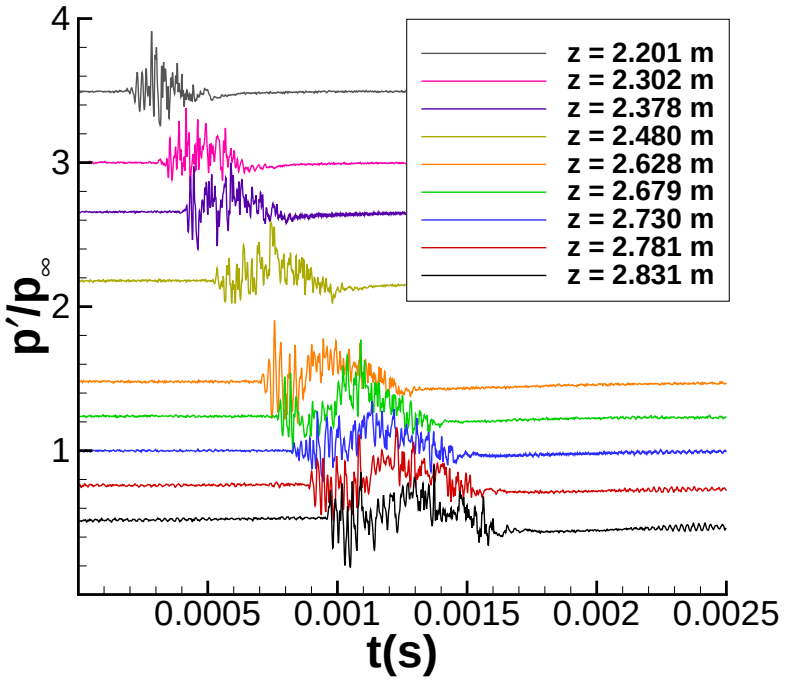

(b) Single perturbation

Figure 4.9. Perturbation generated using the stock valve poppet. $Re = 11.7 \times 10^6/\text{m}$, $p_{0v} = 80$ psig.

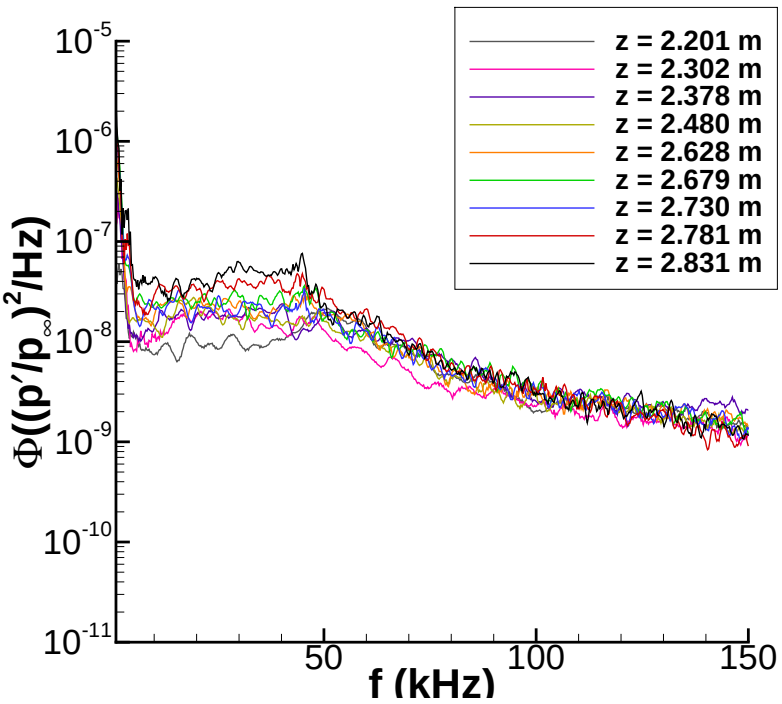

Figure 4.10. Power spectral density for perturbations generated using the stock valve poppet. $Re = 11.7 \times 10^6$/m, $p_{0v} = 80$ psig.

The perturbations shown in Figures 4.16 and 4.17 were generated with the valve equipped with the 0.009-inch-flat. The spectra at $z = 2.201$ m shows a broad peak at 50-60 kHz. By $z = 2.302$ m, there is no longer any peak, instead it has been replaced by broadband noise. It should be noted however that the wave packet at the leading edge of the perturbation is well represented by the ensemble average until $z = 2.730$ m. When the poppet face length is increased to 0.011 inches (Figures 4.18 and 4.19) the spectra indicates a turbulent perturbation at all measurement locations. Additionally, the ensemble averaged perturbations are a poor representation of the fluctuation levels present in the individual samples at all locations.

Figure 4.20 shows the pressure measurements at $z = 2.201$ m for the five valve configurations discussed, offset for clarity. While some poppets do produce slightly shorter duration perturbations, there is no clear trend. It is worth repeating that the differences shown are likely due to the poor repeatability in the alignment of

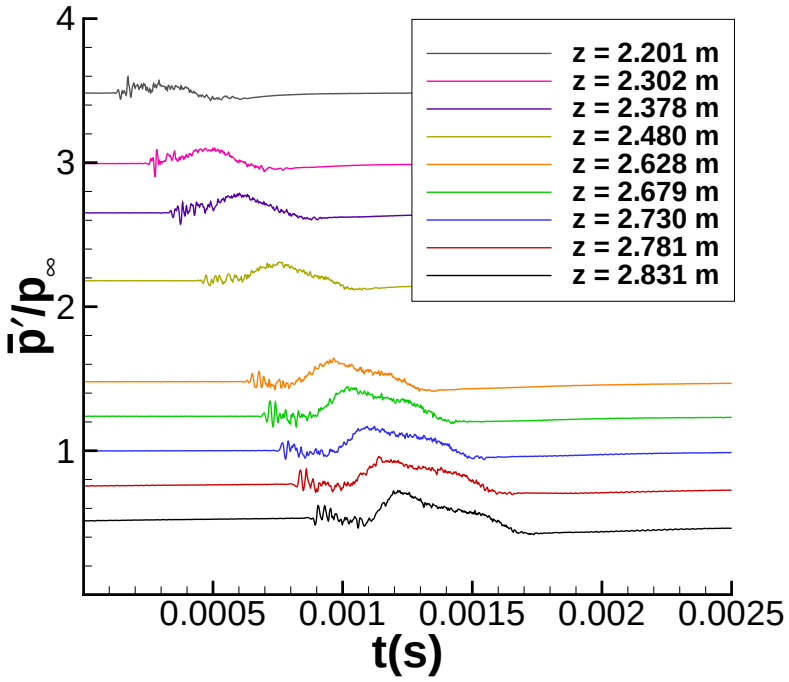

(a) Ensemble average

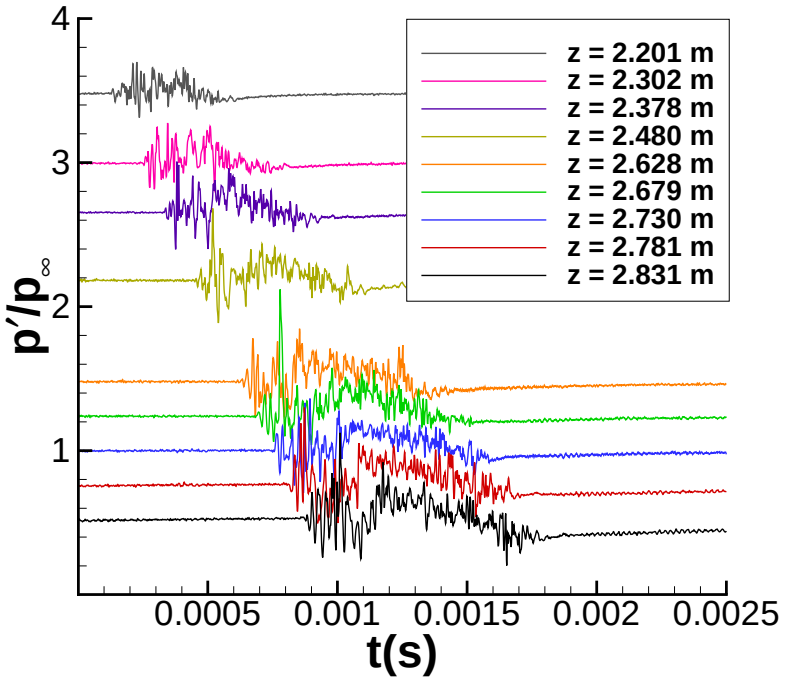

(b) Single perturbation

Figure 4.11. Perturbation generated using the poppet with a 0.003-inch flat. $Re = 11.7 \times 10^6/\text{m}$, $p_{0v} = 80$ psig

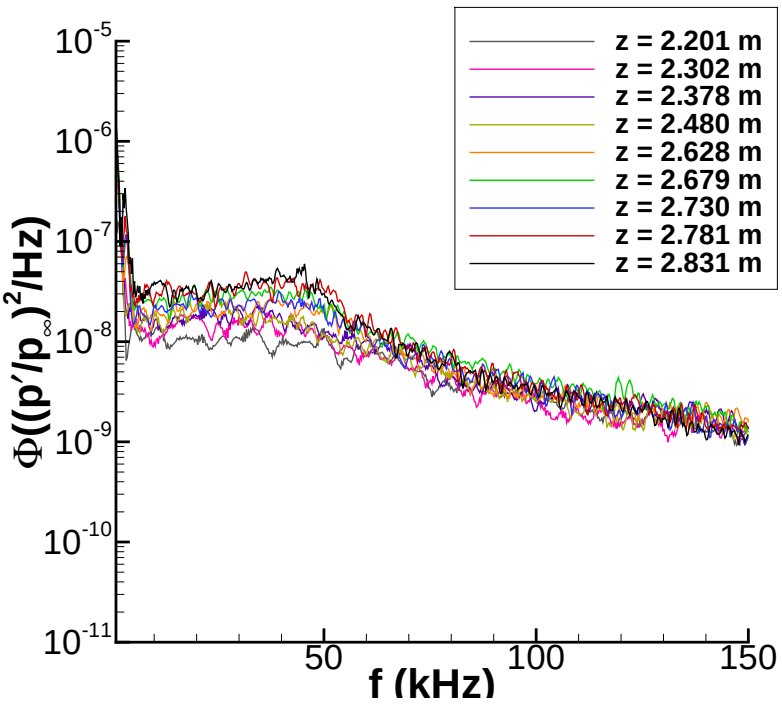

Figure 4.12. Power spectral density for perturbations generated using the poppet with a 0.003-inch flat. $Re = 11.7 \times 10^6/\text{m}$, $p_{0v} = 80$ psig.

the valve. The subjective method used to align the valve leads to different intensity perturbations. It is difficult to set equal intensity perturbations with the subjective alignment method, obfuscating any effect the poppet modifications had on the perturbation duration. Ideally each poppet configuration could be set to produce the same peak amplitude, allowing a measurement of the resulting change in perturbation. In order to accomplish this, an objective method of poppet alignment must be developed. Additional scatter could be due to the difficulty in accurately machining the poppets.

In all cases, by the final sensor at $z = 2.831$ m the mean pressure follows a similar trend to those reported by Casper in the BAM6QT at a freestream Reynolds number of $Re = 10.8 \times 10^6/\text{m}$ [5]. Casper's measurements show a repeatable wave packet at the leading edge of the turbulent spot followed by a large increase mean static pressure followed by a slightly negative pressure. In the present data set, a

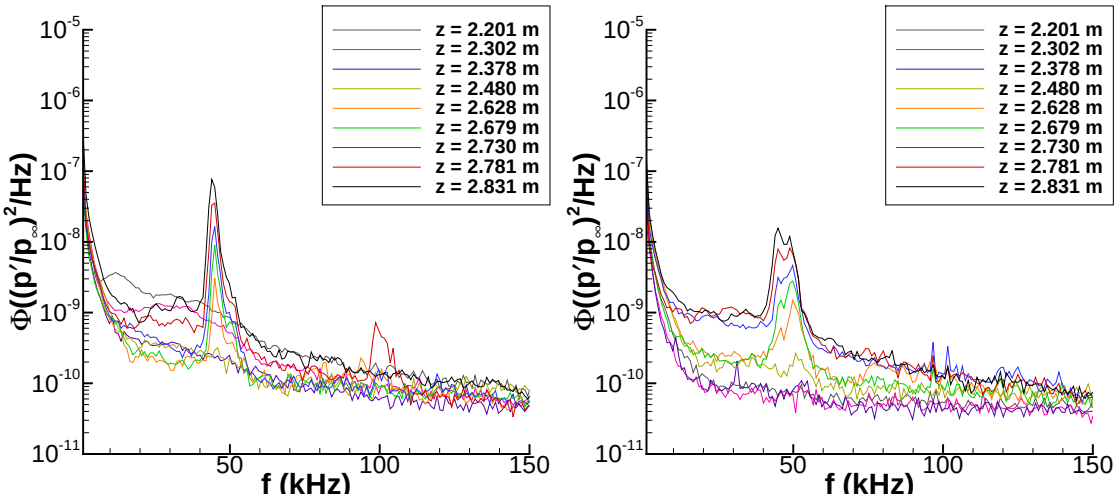

(a) Stock poppet

(b) 0.003 Inch poppet

Figure 4.13. Power spectral density for a period 1 ms immediately after the trailing edge of the perturbations generated by two different valve configurations. $Re = 11.7 \times 10^6/\text{m}$, $p_{0v} = 80$ psig.

similar disturbance structure can be seen, although the waves preceding the mean static pressure rise are out of phase and as a result are attenuated in the ensemble averaged pressure traces. The out of phase signals could be a result of the inherent inconsistency of the mechanical processes in the pulsed jet perturber that were not present in the pulsed glow perturber utilized by Casper, due to the more repeatable timing of a fully electronic device.

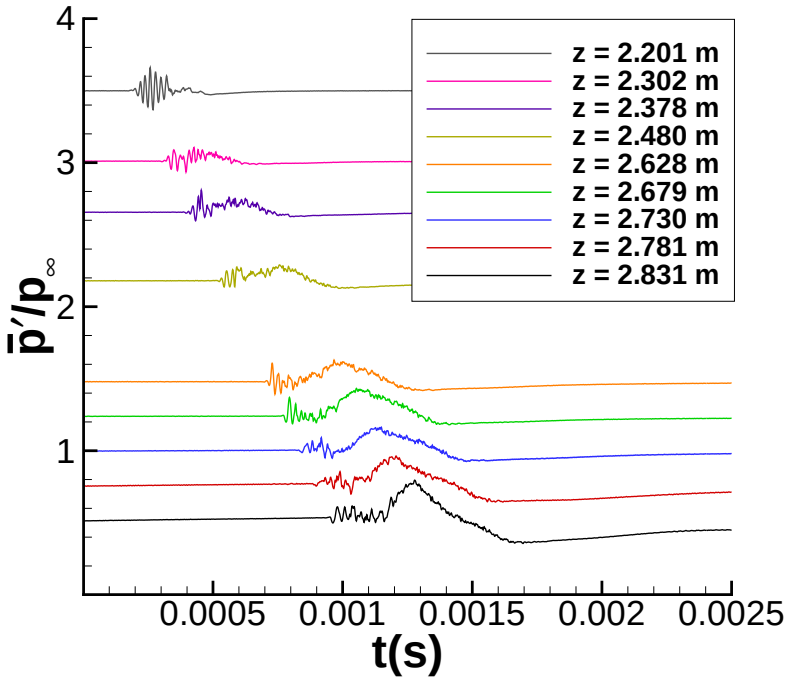

(a) Ensemble average

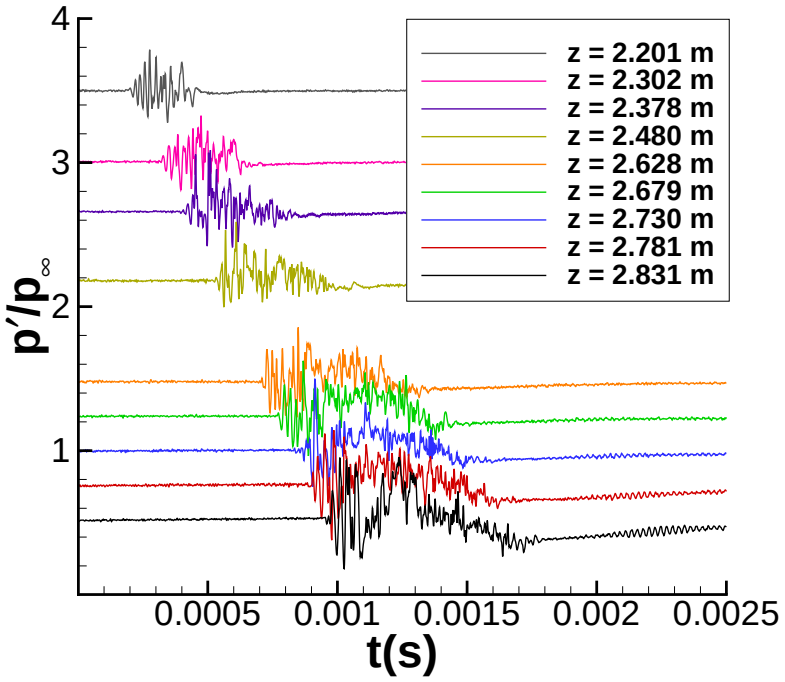

(b) Single perturbation

Figure 4.14. Perturbation generated using the poppet with a 0.005-inch flat. $Re = 12.0 \times 10^6/\text{m}$, $p_{0v} = 80$ psig

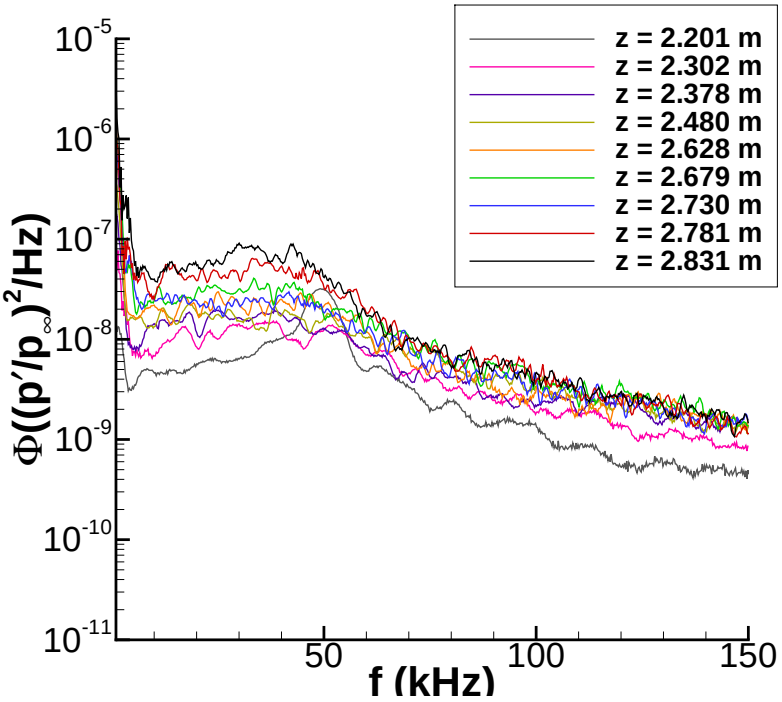

Figure 4.15. Power spectral density for perturbations generated using the poppet with a 0.005-inch flat. $Re = 12.0 \times 10^6/\text{m}$, $p_{0v} = 80$ psig.

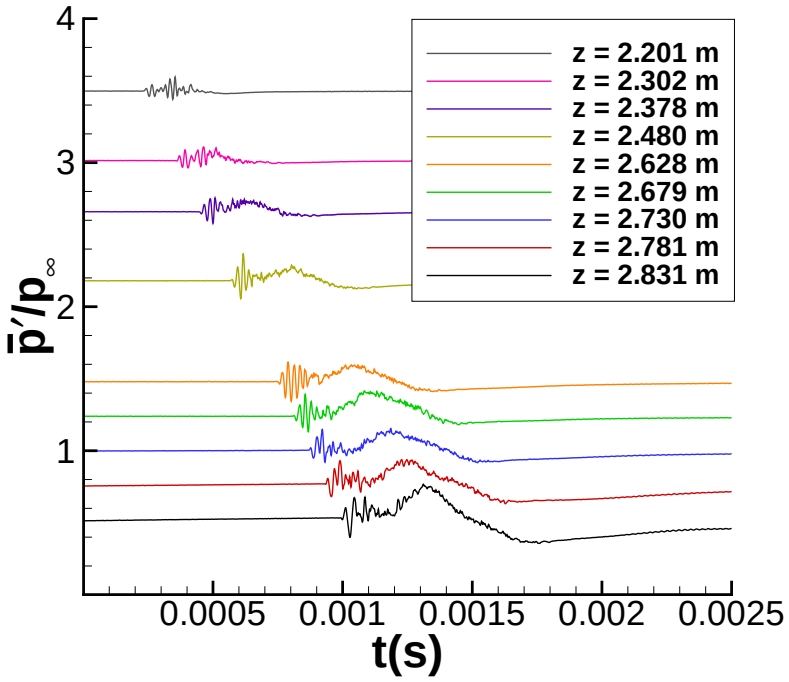

(a) Ensemble average

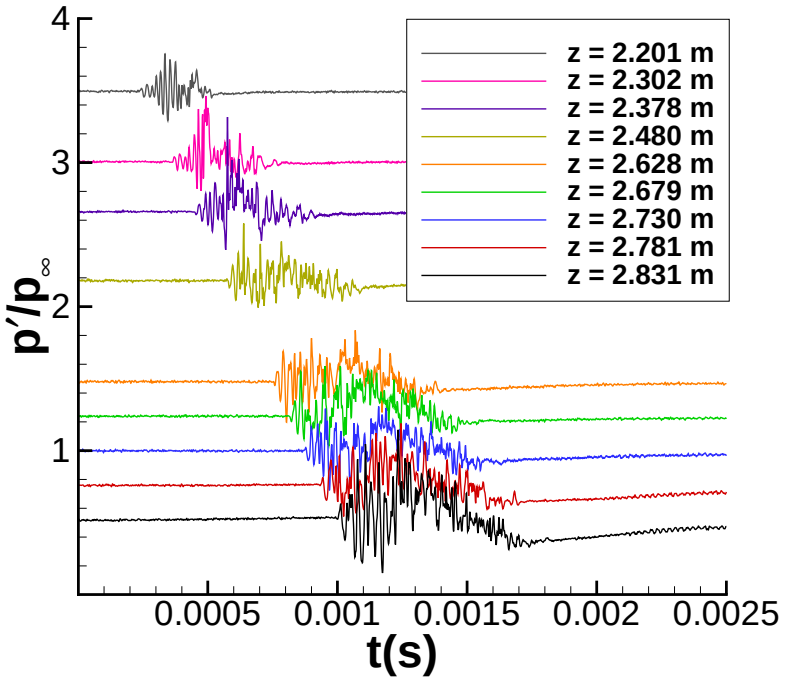

(b) Single perturbation

Figure 4.16. Perturbation generated using the poppet with a 0.009-inch flat. $Re = 11.9 \times 10^6/\text{m}$, $p_{0v} = 80$ psig

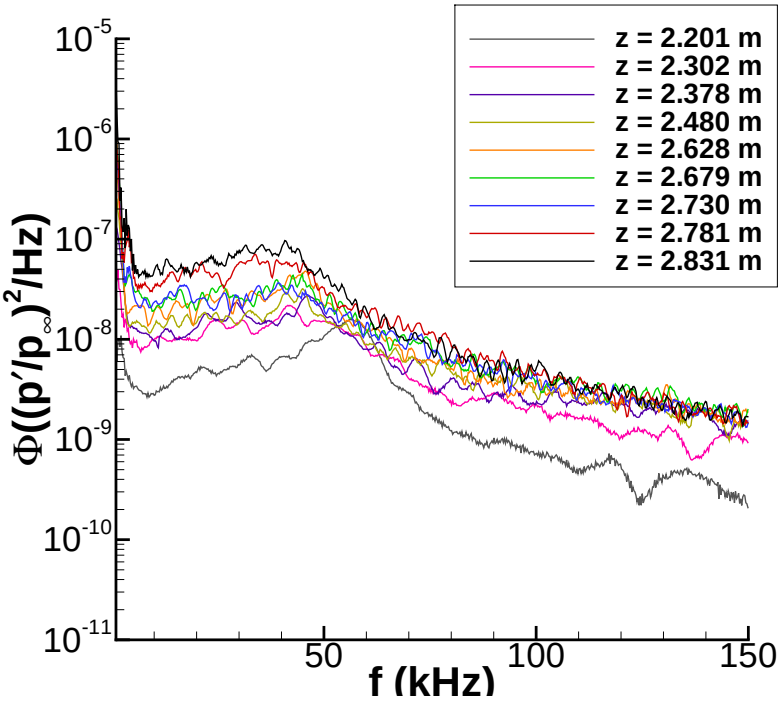

Figure 4.17. Power spectral density for perturbations generated using the poppet with a 0.009-inch flat. $Re = 11.9 \times 10^6/\text{m}$, $p_{0v} = 80$ psig.

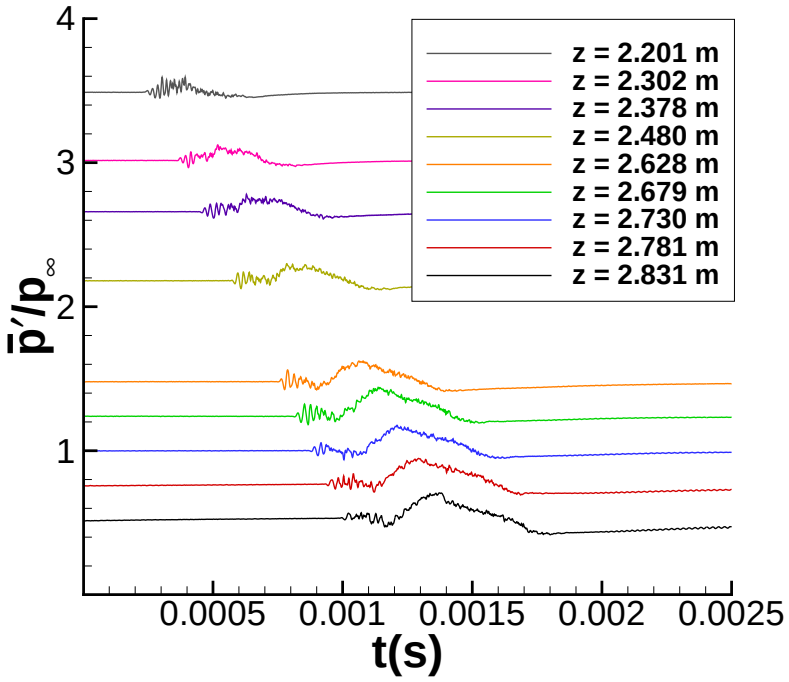

(a) Ensemble average

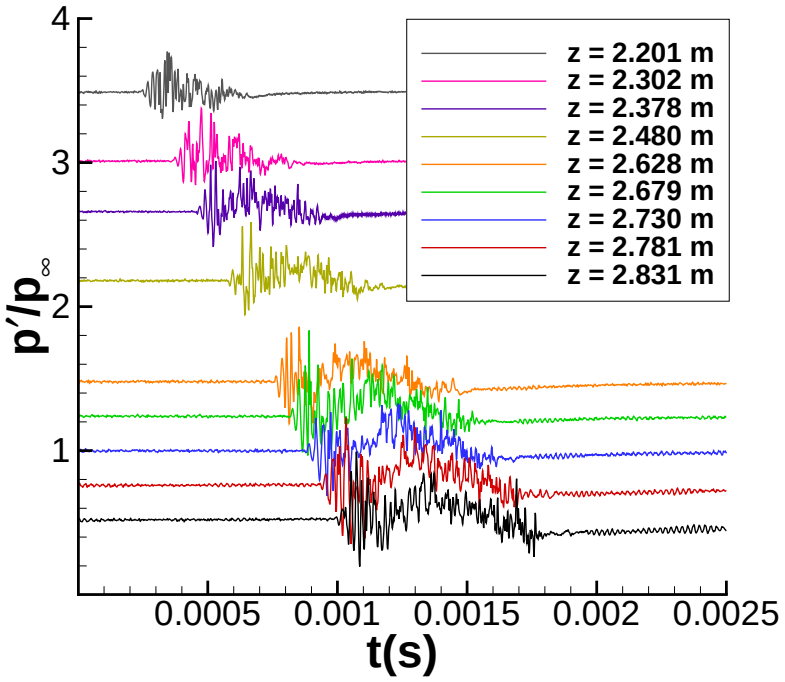

(b) Single perturbation

Figure 4.18. Perturbation generated using the 0.011 inch face depth valve poppet. $Re = 11.7 \times 10^6/\text{m}$, $p_{0v} = 80$ psig

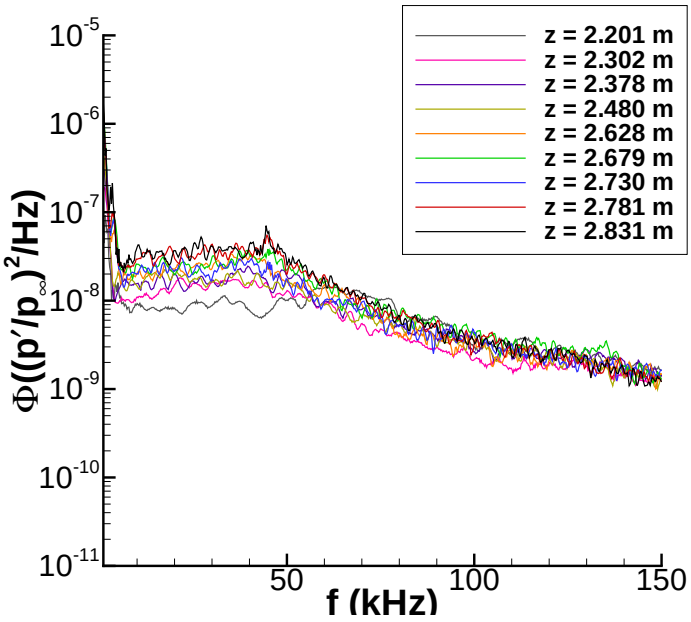

Figure 4.19. Power spectral density for perturbations generated using the poppet with a 0.011-inch flat. $Re = 11.7 \times 10^6/\text{m}$, $p_{0v} = 80$ psig.

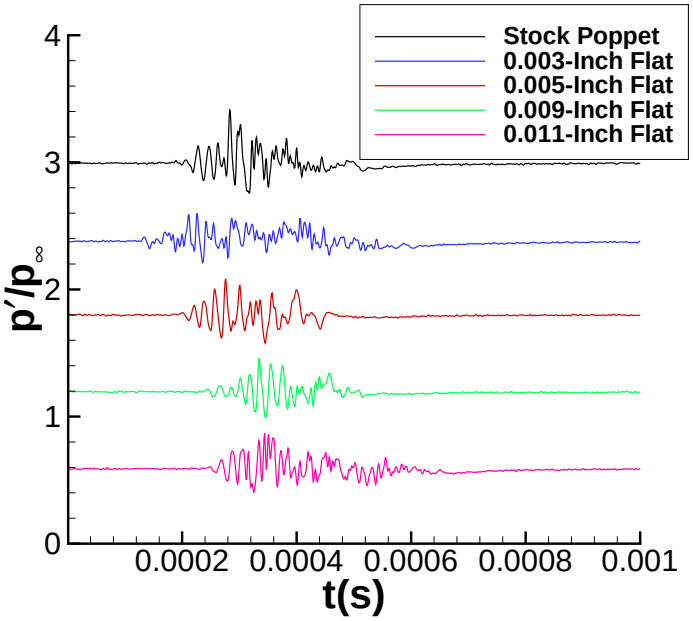

Figure 4.20. Individual pressure traces at $z = 2.201$ m for five different poppet configurations. $Re \approx 11.7 \times 10^6/\text{m}$, $p_{0v} = 80$ psig

4.3.2 Hot Wire Measurements

Perturbation measurements were also taken using the hot wire anemometry. The hot-wire measurements were taken 1.9 mm above the bottom of the nozzle wall. All hot wire measurements were taken at the maximum quiet stagnation pressure in the BAM6QT, giving a nominal freestream Reynolds number of $Re = 11.5 \times 10^6$/m. Perturbations were made using five different poppet configurations with flats ranging from 0.000 (stock) to 0.011 inches. Figure 4.21 shows the ensemble average of 50 samples of the uncalibrated AC voltage response. The presence of a naturally occurring turbulent spot resulted in a large increase in hot wire voltage from the mean. In order to remove any perturbations contaminated by naturally occuring turbulent spots from the data set, samples were thrown out if the mean voltage during the first 0.0005 seconds was greater than 2 mV. A single hot wire was used for all measurements; survivability of the hot wires did not present a problem during this experiment.

The hot-wire data shows a typical response pattern to the perturbations. There is a small dip in the hot wire voltage immediately preceding the perturbation, which is followed by a rapid rise to a peak. After the maximum mass flux, it decays back to ambient noise levels. A measurement was made to determine the duration of the perturbations. The perturbation beginning was set as the low peak ahead of the perturbation. The end point was set as the time required for the hot wire response to reach either 3% or 10% of the maximum voltage. Table 4.2 lists the durations of the perturbations generated by each valve configuration. It can be seen that the 10% cut off produces perturbation durations that are roughly 10% shorter than calculated using the 3% cutoff. The 0.003 inch face poppet performed the best, although the improvement could have been due to a better alignment as there was no quantifiable method of aligning the valve.

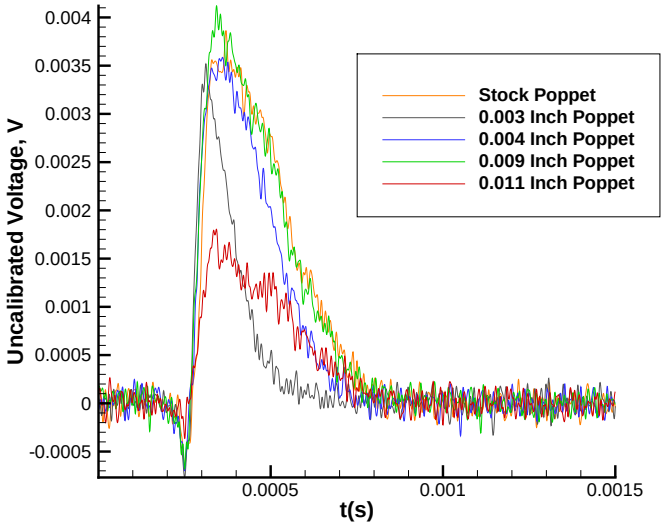

Figure 4.21. Ensemble averaged hot wire measurements of perturbations taken 0.031 m behind the perturber. $Re = 11.5 \times 10^6$/m nominally.

Table 4.2 Perturbation durations measured using hot wire anemometry for various perturber configurations.

Poppet Configuration	Duration (μs)(3%)	Duration (μs)(10%)
Stock	525	469
0.003 Inches	288	257
0.004 Inches	448	391
0.009 Inches	513	440
0.011 Inches	492	472

4.3.3 Perturbation Duration and Convection Velocity

Determination of the convection rates of turbulent spots is important in order to accurately determine the transition length when using a turbulent spot model of

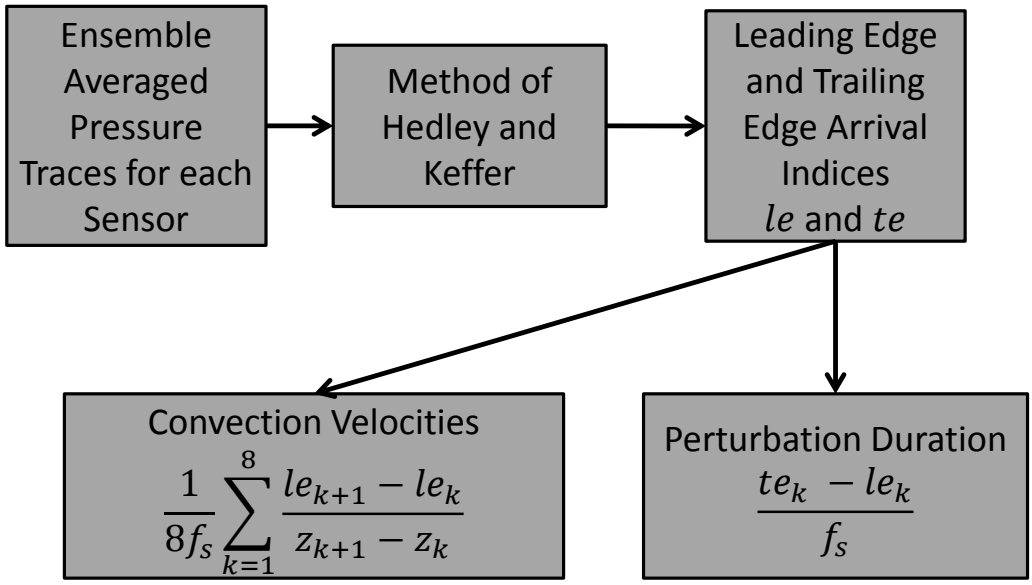

Figure 4.22. Flow chart for determining perturbation durations and convection velocities. k indicates sensor number.

transition. For each run, the method of Hedley and Keffer described in Section 3.5.1 was used to determine the leading and trailing edges of the perturbation using the ensemble averaged pressure traces [43]. The convection velocity of each edge was then calculated by determining the time each perturbation took to convect from the Kulite XCQ-062-15A sensor at $z = 2.201$ m to each other Kulite. The sensor at $z = 2.302$ m was ignored in this calculation, as small errors resulting from the algorithm were amplified by the short distance between the first two sensors. The resulting velocities were averaged to produce an average leading and trailing edge convection velocity for a given run. A flow chart of this process is shown in Figure 4.22.

Table 4.3 gives the convection velocities at both the leading and trailing edge for various valve configurations with a 95% confidence interval based on the sample standard error. The leading edge is easier for the algorithm to detect, as the pressure

fluctuations at the leading edge rise quickly above the background tunnel noise. At the trailing edge, the pressure fluctuations decay slowly back to background noise levels. This, combined with the second-mode waves trailing the perturbations make it difficult to determine a clear trailing edge in the current data set. Additionally, there is a lack of repeatability at the trailing edge of the perturbations.

Figure 4.23 shows the criterion function (Eq. 3.4) for several individual perturbations during a run at $Re = 11.7 \times 10^6/\text{m}$, where t = 0 s is the time at which the trigger signal begins. The leading edge of the perturbation is fairly repeatable, with a small amount of scatter on the order of 20-30μs , which is correctable by determining all characteristics relative to the leading edge. The trailing edge shows far more scatter. This is likely due to a combination of two factors. The valve closing process likely has some level of variation, or the inherent randomness of the turbulent process at the trailing edge of the spot results in slight differences between individual spots. As a result, the error is higher than when calculating the leading edge convection velocity.

Despite this difficulty, measured trailing edge convection velocities fall within the range reported in literature. Casper reported U_{le}/U_∞ from 0.93-0.97 across a range of Reynolds numbers and noted a similar difficulty determining the trailing edge [5, 46]. Schubauer and Klebanoff also found a higher level of error while determining the trailing edge convection velocity [9]. Trailing edge convection velocities are lower than the primary values reported by Casper, although they do fall within the range reported by Redford et al. [20]

Initially, the convection rates and the perturbation durations were to be used to calculate the approximate length of the perturbations. This proved unreliable using the current data set. When determining the perturbation convection velocities, data could be averaged over multiple sensors to improve the accuracy of the calculation. When determining the perturbation durations, each duration had to be determined at a single sensor. It was impossible to average multiple values to improve the accuracy of the calculation. This lead to such errant results as the algorithm interpreting that

Table 4.3 Convection velocity for various perturber configurations at $Re \approx 12 \times 10^6$/m.

Configuration	U_{le}/U_∞	U_{te}/U_∞	U_{mean}/U_∞
1	0.95 ± 0.02	0.69 ± 0.06	0.82
2	0.97 ± 0.02	$0.65. \pm 0.07$	0.81
3	0.98 ± 0.02	$0.60. \pm 0.01$	0.79
4	0.96 ± 0.01	$0.60. \pm 0.05$	0.78
5	0.96 ± 0.01	$0.63. \pm 0.03$	0.79
6	0.97 ± 0.01	$0.57. \pm 0.07$	0.77
7	0.96 ± 0.02	$0.64. \pm 0.03$	0.80
8	0.96 ± 0.03	$0.66. \pm 0.04$	0.81
Average	0.96 ± 0.02	$0.63. \pm 0.05$	0.81

the perturbation duration decreased as it convected downstream, when simple visual examination showed this to not be the case.

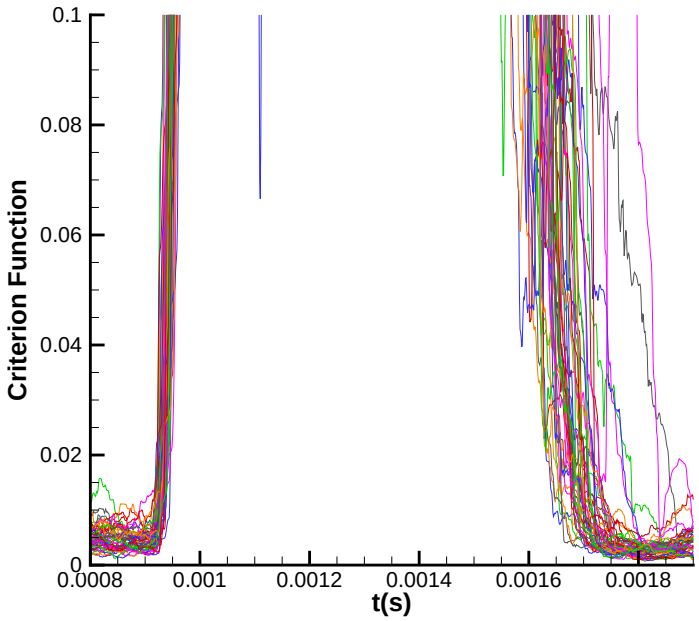

Figure 4.23. Criterion function for perturbations generated at $Re = 11.7 \times 10^6/\text{m}$, $p_{0v} = 80$ psig. t=0 s is the point at which the valve electronics fire.

5. Perturber Performance Under Varying Conditions

5.1 Valve Stagnation Pressure Effects

A single valve configuration was used to test the effect of the valve stagnation pressure on the perturbations. A poppet with a 0.005-inch flat was used to make perturbations for the centerline pressure measurements. The tests were performed at freestream unit Reynolds numbers from $Re = 11.5 - 12.1 \times 10^6$/m. Three separate valve stagnation pressures were tested in 20 psi intervals from 40-80 psig. Additional pressures below 40 psig were tested, but failed to produce measurable perturbations. In between runs, the change in valve stagnation pressure was sufficient to shift the valve alignment. This necessitated a realignment of the pulse valve.

Decreasing the stagnation pressure of the jet decreases the mass flow rate through the perturber system and the jet penetration, which should reduce the effective amplitude of the perturbation. It was sought to reduce the total amplitude of the perturbation in hopes that only a small portion of the overall perturbation duration would be strong enough to seed a turbulent spot. Three separate runs are shown in Figures 5.1 - 5.5.

Figure 5.1 shows the pressure trace for a typical perturbation generated at the maximum quiet freestream unit Reynolds number with a valve stagnation pressure of 80 psig. The spectra at $z = 2.201$ and 2.302 m (Figure 5.2) have lower levels of broadband noise than the rest of the sensor locations, possibly indicating a perturbation in the late stages of transition. Downstream, the ensemble averaged pressure traces show fluctuations at the leading edge of the perturbation that are not smoothed by the averaging.

Figure 5.3 shows the perturbation that results when the valve stagnation pressure is decreased to 60 psig. The perturbation looks very similar to the perturbation

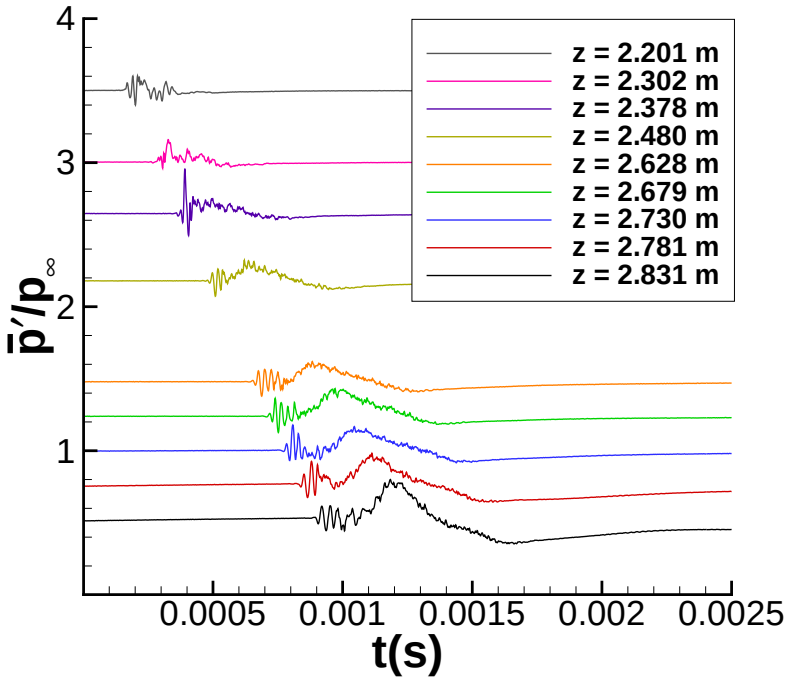

(a) Ensemble average

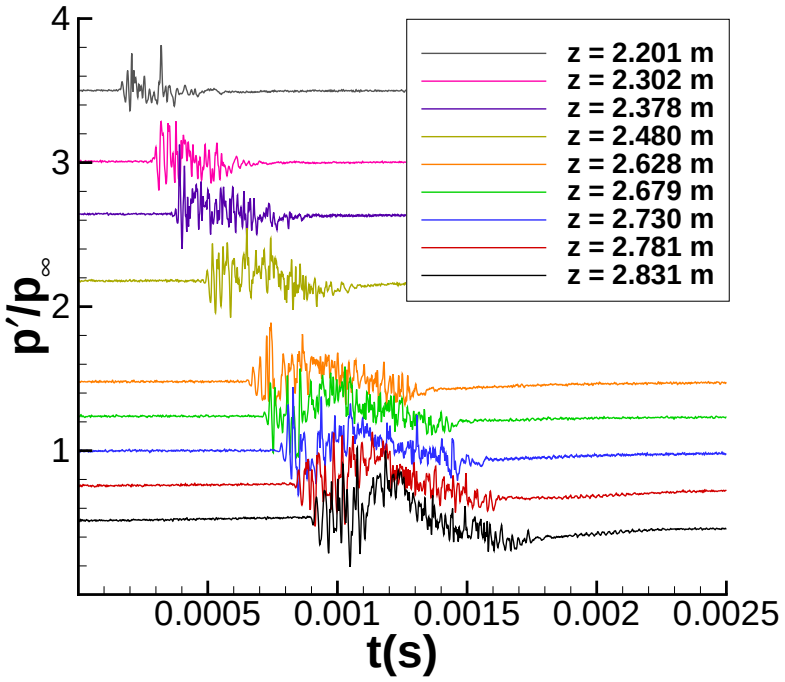

(b) Single perturbation

Figure 5.1. Perturbation generated using the 0.005 inch poppet. $Re = 11.7 \times 10^6/\text{m}$, $p_{0v} = 80$ psig

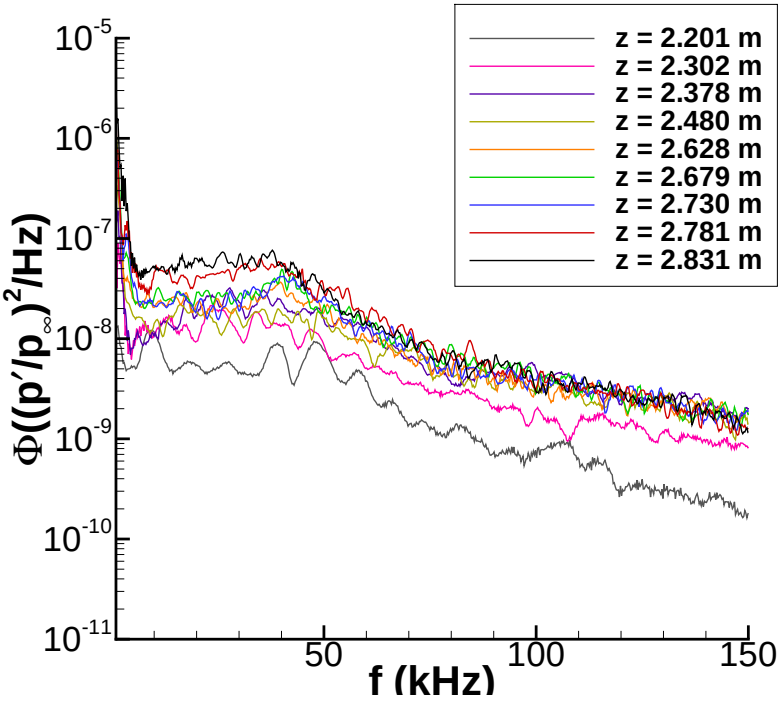

Figure 5.2. Power spectral density for perturbations generated using the poppet with a 0.005-inch flat. $Re = 11.7 \times 10^6/\text{m}$, $p_{0v} = 80$ psig

generated with a valve stagnation pressure 80 psig. The pressure trace shows higher fluctuation levels in the center of the perturbation at $z = 2.201$ m. The spectra shown in Figure 5.4 indicate high levels of broadband noise at all sensor locations, indicating a perturbation that is turbulent throughout the entire measurement range.

Figure 5.5 has a further reduction in valve stagnation pressure to 40 psig. This perturbation does appear to be of a lower amplitude than the perturbations generated at higher valve stagnation pressures. The spectrum at $z = 2.201$ m shown in Figure 5.6 has a very broad peak at 55 kHz and lower levels of broadband noise compared to the other sensors. By $z = 2.302$ m the peak is no longer visible and the spectra indicate a turbulent perturbation. The pressure traces show a similar structure with higher levels of pressure fluctuations at the leading edge followed by an increase in the static pressure accompanied by a decrease in the fluctuation intensity.

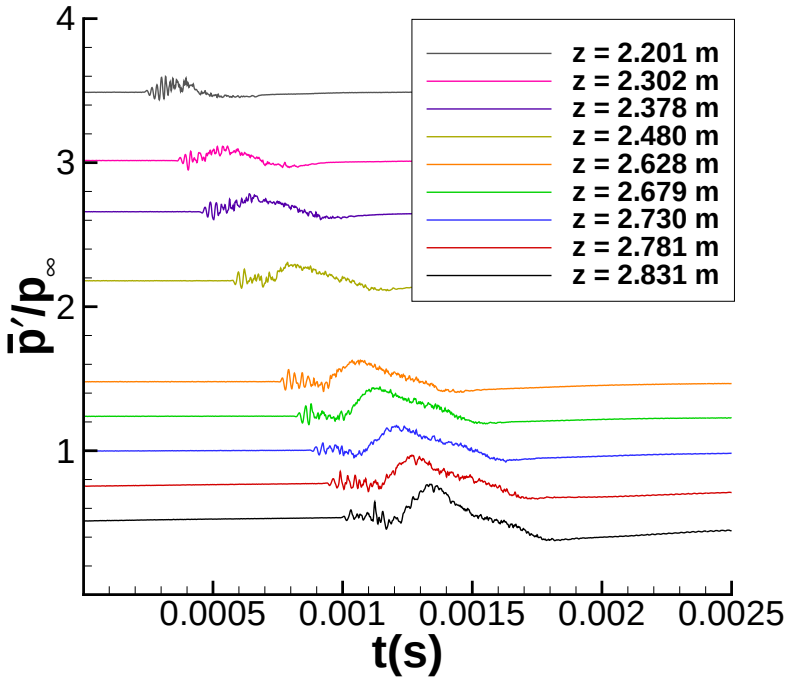

(a) Ensemble average

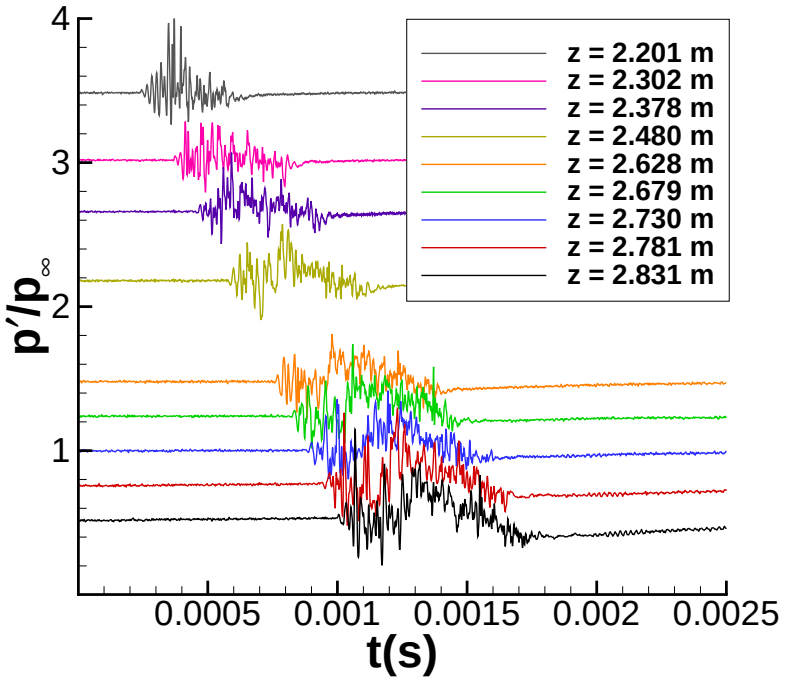

(b) Single perturbation

Figure 5.3. Perturbation generated using the 0.005 inch poppet. $Re = 11.7 \times 10^6/\text{m}$, $p_{0v} = 60$ psig

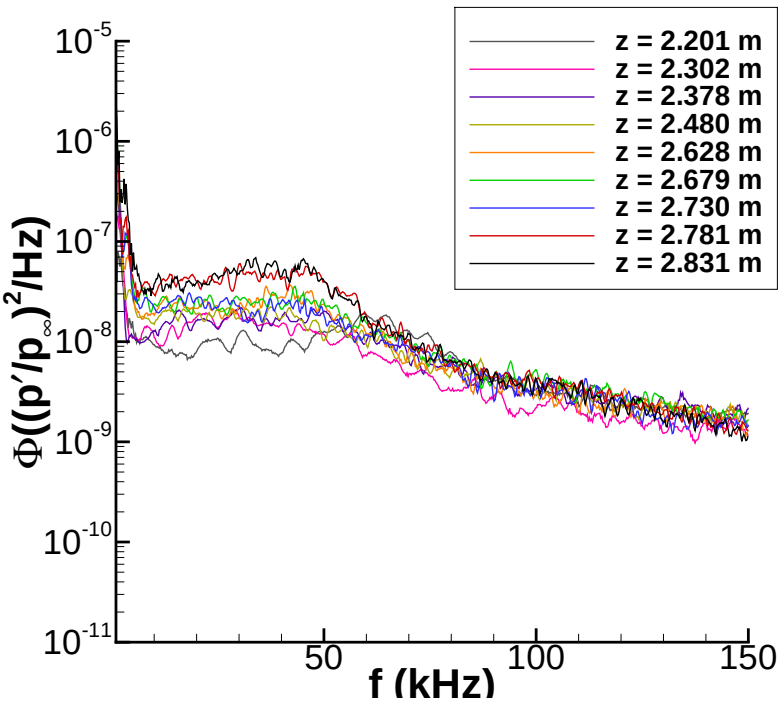

Figure 5.4. Power spectral density for perturbations generated using the poppet with a 0.005-inch flat. $Re = 11.7 \times 10^6/\text{m}$, $p_{0v} = 60$ psig

Figure 5.7 shows individual pressure traces for the three cases presented above. The traces show that the 40 psig valve stagnation pressure case is of a shorter duration. Unfortunately, the spectrum at $z = 2.201$ m show a peak at 55 kHz and lower levels of broadband noise (Figure 5.6). This could indicate that the perturbation generated by the 40 psig valve stagnation pressure might not be fully turbulent, decreasing the benefit of the shorter duration. Recent modifications to the air supply has increased the maximum valve stagnation pressure from 80 psig to 140 psig. Further testing is needed to determine if this higher pressure will be more effective at making perturbations, or if it will be accompanied by an increase in perturbation duration.

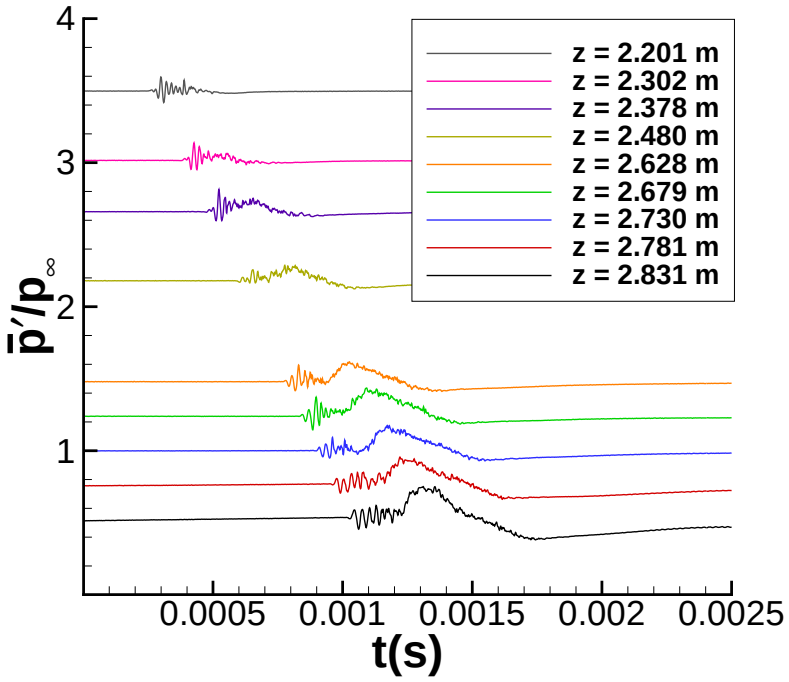

(a) Ensemble average

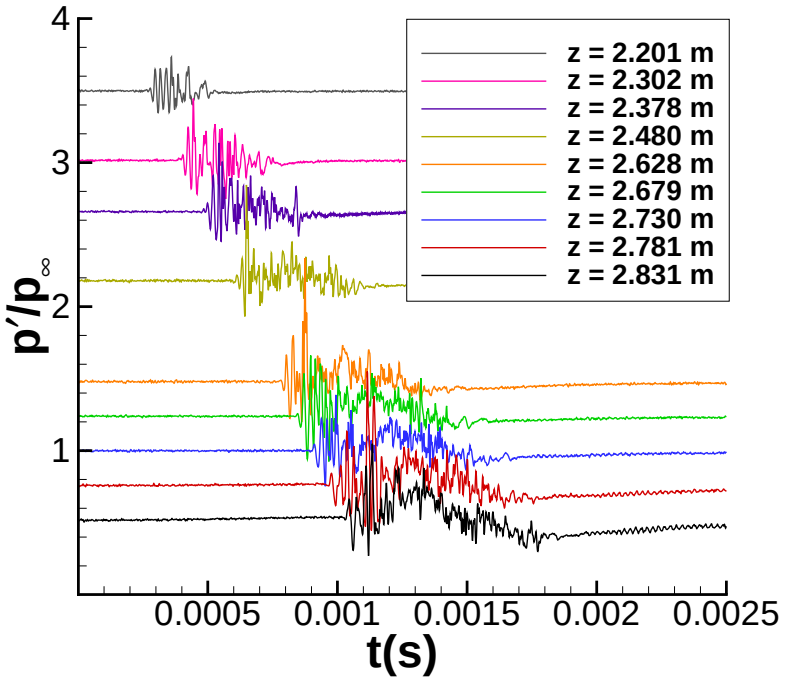

(b) Single perturbation

Figure 5.5. Perturbation generated using the 0.005 inch poppet. $Re = 11.7 \times 10^6/\text{m}$, $p_{0v} = 40$ psig

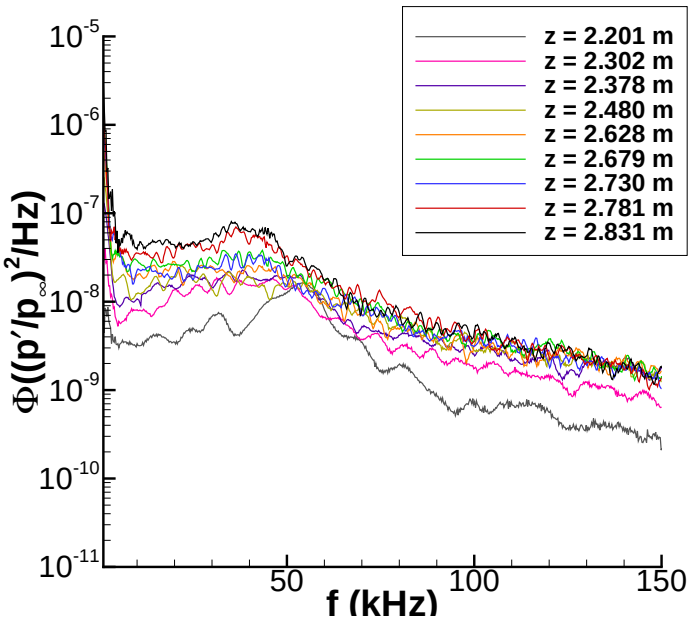

Figure 5.6. Power spectral density for perturbations generated using the poppet with a 0.005-inch flat. $Re = 11.7 \times 10^6$/m, $p_{0v} = 40$ psig

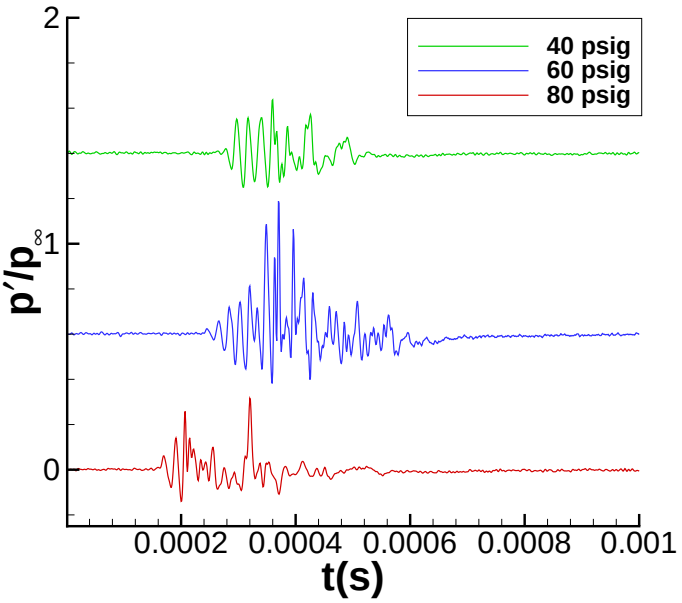

Figure 5.7. Comparison of three individual perturbations generated with different valve stagnation pressures at $z = 2.201$ m. $Re = 11.7 \times 10^6$/ m. Offset for clarity.

5.2 Reynolds Number Effects

Perturbations generated at the maximum quiet freestream unit Reynolds number typically showed a fully turbulent disturbance at the first sensor location. Due to the limited data available, it was difficult to determine whether the resultant perturbation was truly a turbulent spot. In an effort to improve certainty, four runs were made at varying freestream unit Reynolds numbers. The same perturber configuration was used in each case, using the poppet with an 0.011-inch flat at a valve stagnation pressure of $p_{0v} = 40$ psig without removing the valve from the tunnel. This configuration was chosen simply because it happened to be set up at the time of the test. There was no strong evidence that any configuration performed better than the others due to the inherent issues with the valve alignment. There is a chance that the beginning of the tunnel runs, which can shift the tunnel, caused a slight shift in the valve alignment. Leaving the valve attached to the tunnel without attempting realignment was deemed more desirable then attempting to realign the valve. The resultant perturbations and spectra are shown in Figures 5.8 - 5.15.

Figure 5.8 shows a perturbation generated at roughly the maximum quiet freestream Reynolds number of the BAM6QT. At this Reynolds number, the perturbation shows signs of laminar-turbulent transition at $z = 2.201$ m. The spectrum has a broad peak from 40-60 kHz accompanied by moderate levels of broadband noise. The spectra indicate a turbulent flow for every other sensor.

Figure 5.10 shows the presssure traces for a perturbation generated at a $Re = 8.38 \times 10^6$/m. The first three sensor locations ($z = 2.201 - 2.378$ m) show a transitional perturbation, with a well organized wave packet visible in both the ensemble average and individual samples, trailed by lower levels of turbulent fluctuations. In the spectrum at $z = 2.201$ m shown in Figure 5.11, there is a broad double lobed peak from 30-50 kHz with small peaks at 30 - 45 kHz. This could be indicative of a different transition process than observed by Casper. The spectra indicate different frequency content when using the perturbations generated using the pulsed glow per-

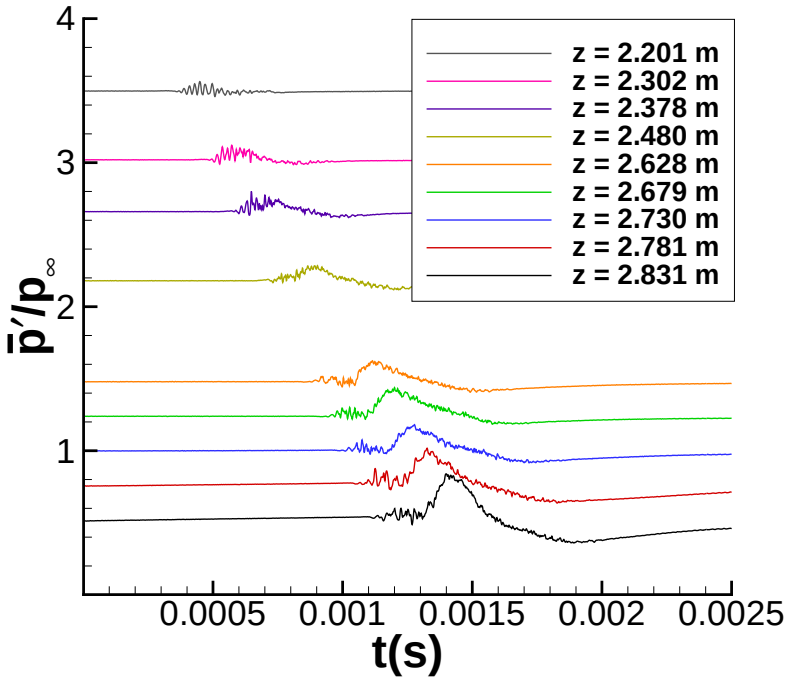

(a) Ensemble average

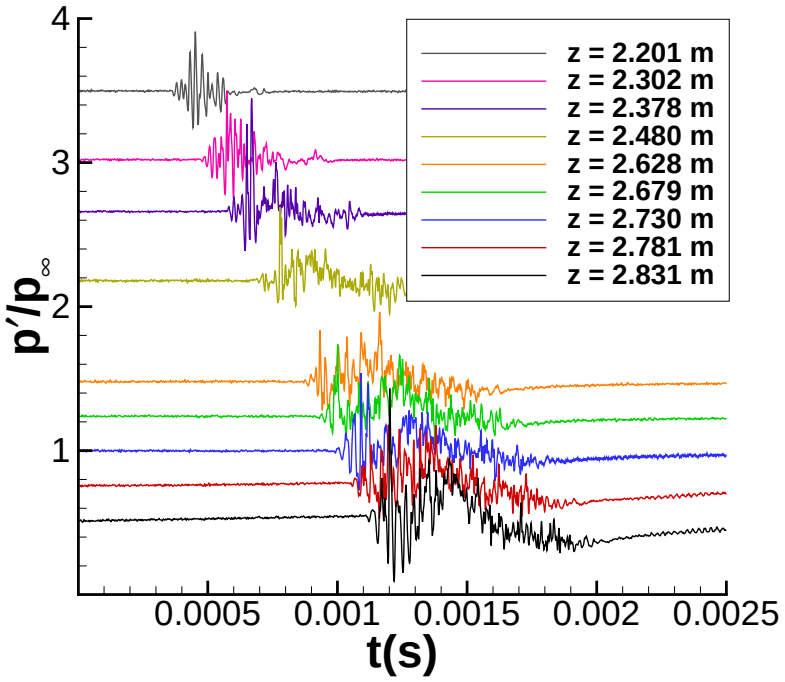

(b) Single perturbation

Figure 5.8. Perturbation generated using a poppet with an 0.011-inch flat, $Re = 11.8 \times 10^6$/m, $p_{0v} = 40$ psig

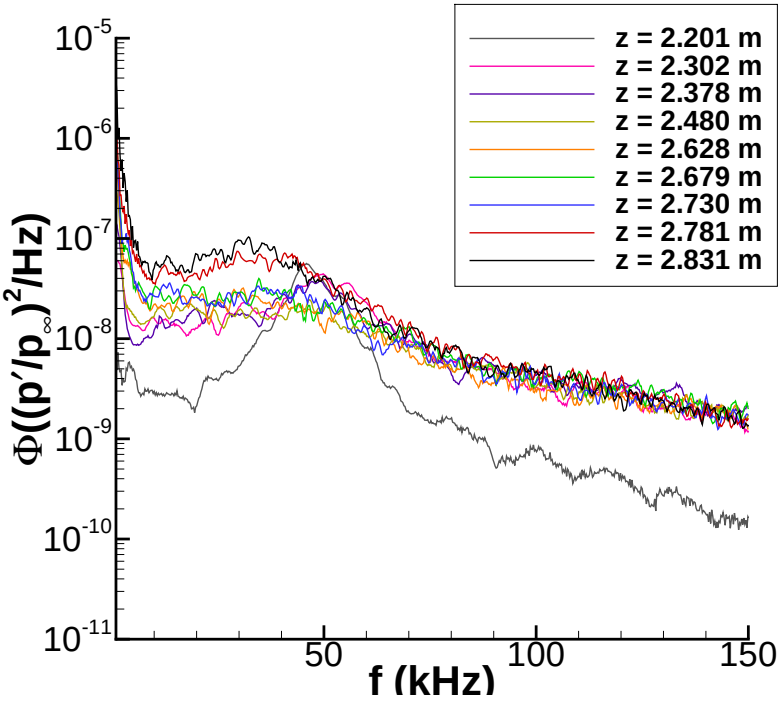

Figure 5.9. Power spectral density for a perturbation generated using a poppet with an 0.011- inch flat, $Re = 11.8 \times 10^6$/m, $p_{0v} = 40$ psig

turber. As the spot convects downstream over the sensors at $z = 2.302$ and 2.378 m, the spectral peak narrows at 45-50 kHz, followed by a rise in broadband noise. The pressure traces show that the largest amplification of the second mode waves at this axial location occurs in the center of the perturbation. Further downstream, wave packet breakdown begins in the rear half of the perturbation. Of note is the absence of the harmonics found by Casper in the same facility in transitional instability wave packets, with higher initial amplitudes shown in the present data [5]. Casper suggested that the higher initial amplitude of the disturbances could have resulted in enough growth to cause transition prior to non-linear growth taking place [47].

At even lower freestream Reynolds numbers, the transition process occurs further downstream. Figure 5.12 show the pressure traces generated at $Re = 7.48 \times 10^6$/m. The ensemble averaged trace at $z = 2.201$ m shows fluctuation levels that are similar to the individual trace, although the rear of the disturbance does not agree as well.

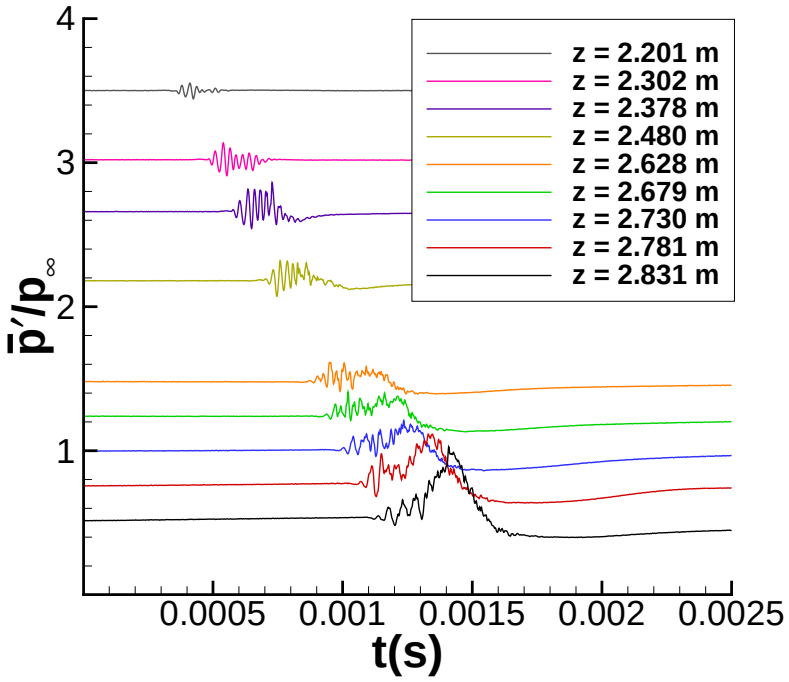

(a) Ensemble average

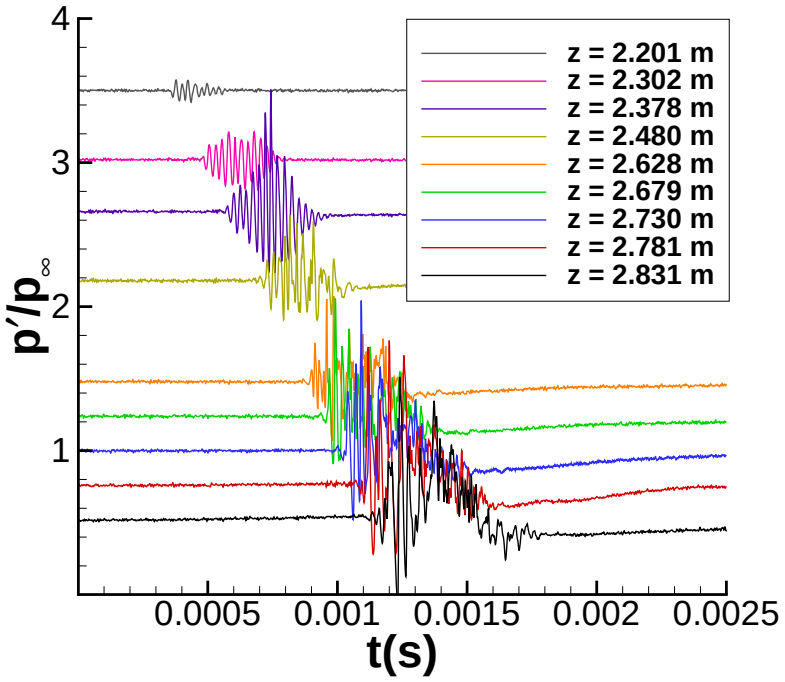

(b) Single perturbation

Figure 5.10. Perturbation generated using a 0.011 inch poppet, $Re = 8.38 \times 10^6/\text{m}$, $p_{0v} = 40$ psig

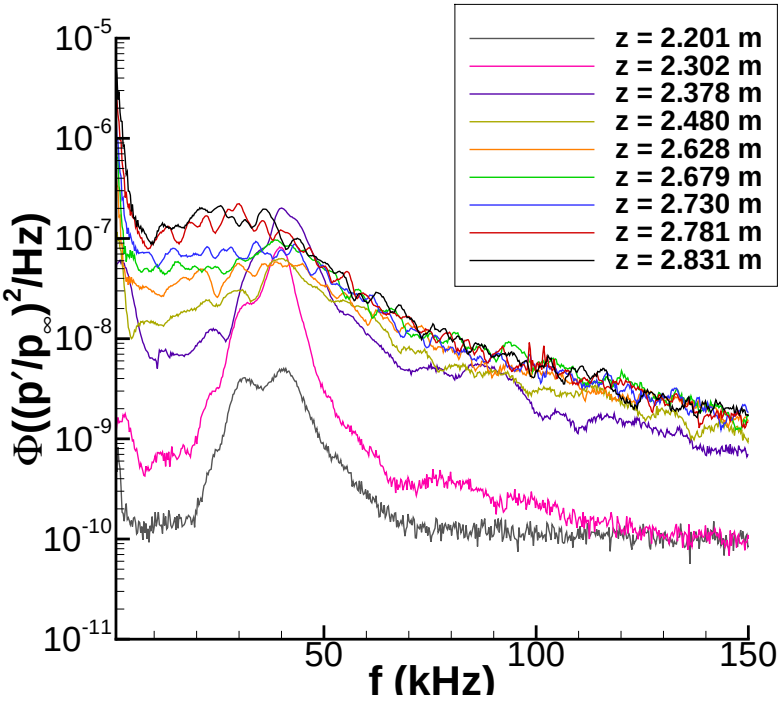

Figure 5.11. Power spectral density for a perturbation generated using a poppet with an 0.011- inch flat, $Re = 8.38 \times 10^6$/m, $p_{0v} = 40$ psig

As the perturbations convect downstream, the highest levels of amplification are seen in the center of the wave packets at $z = 2.378$ m. Further downstream, the ensemble averages become poor indicators of the fluctuation levels within the perturbations. Figure 5.13 shows the spectra of the perturbations. The frequency of the second mode waves has dropped slightly to between 30 and 45 kHz, as would be expected from the increased thickness of the boundary layer at lower unit Reynolds numbers. The twin peaks in the spectra are now located at 30 and 40 kHz, and are more defined than at $Re = 8.38 \times 10^6$/m. The amplitude of the pressure fluctuations have dropped due to the decreased unit Reynolds number. The first evidence of harmonics appears at 80 kHz at $z = 2.378$ m, but even these are small compared to those reported by Casper, and are accompanied by a slight increase in broadband noise.

At $Re = 5.53 \times 10^6$/m (Figure 5.14) the wave growth prior to the first sensor has been reduced to nearly the background noise levels. The second mode waves

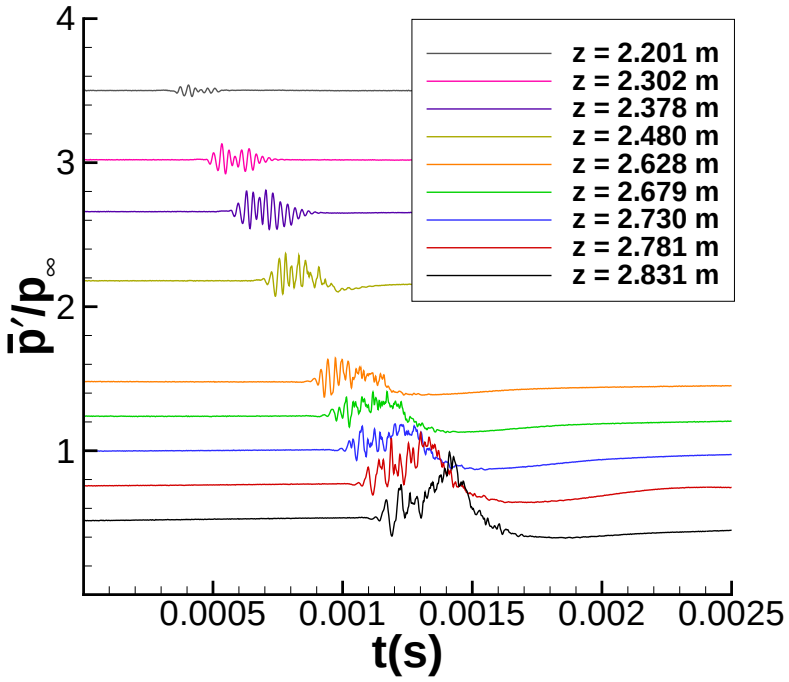

(a) Ensemble average

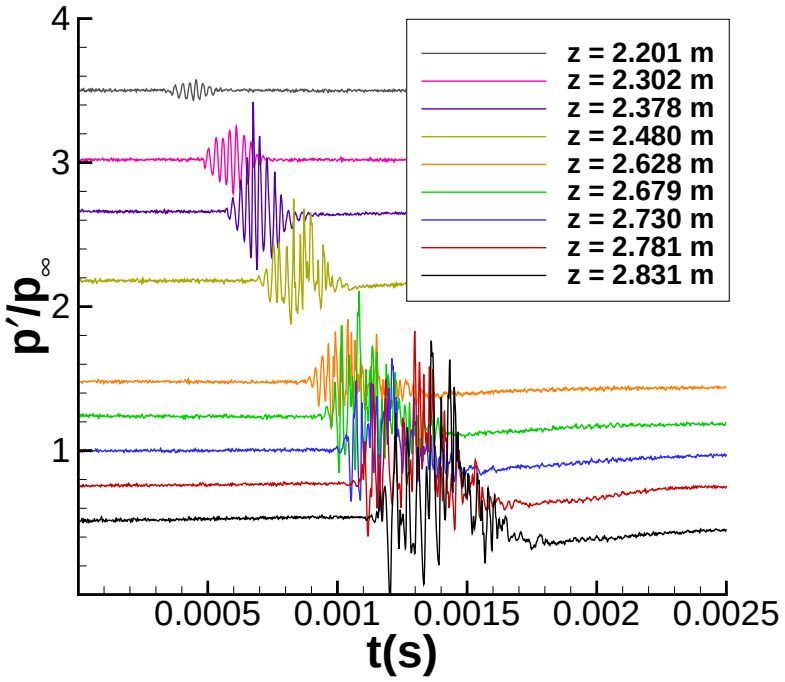

(b) Single perturbation

Figure 5.12. Perturbation generated using a 0.011 inch poppet, $Re = 7.48 \times 10^6/\text{m}$, $p_{0v} = 40$ psig

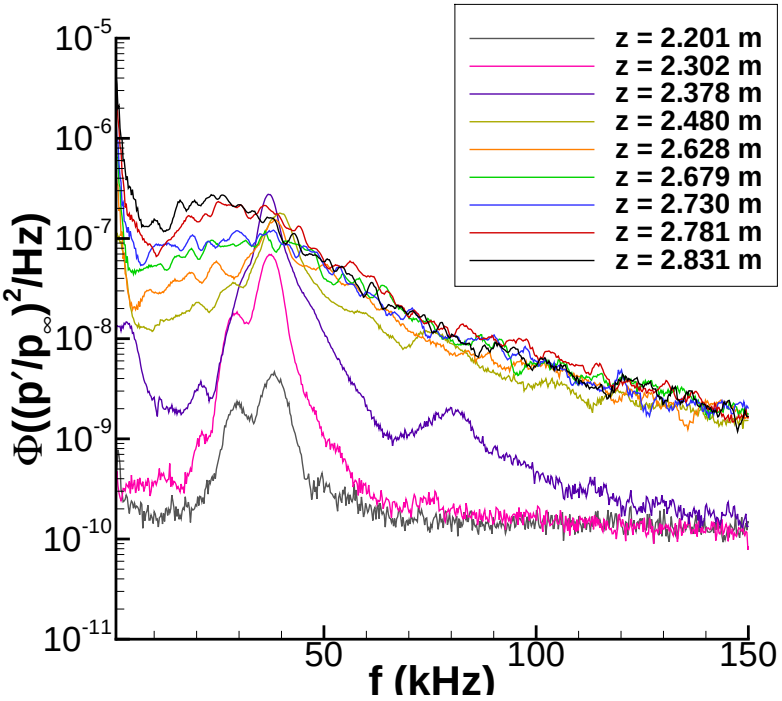

Figure 5.13. Power spectral density for a perturbation generated using a poppet with an 0.011-inch flat, $Re = 7.48 \times 10^6$/m, $p_{0v} = 40$ psig

appear at 30-35 kHz, as shown in Figure 5.15. The dual-lobed peak is no longer present. Additionally, harmonics can be seen in Figure 5.15 from 50-60 kHz at $z =$ 2.378 and 2.480 m. It is unclear if non-linear growth is present, as the gap between the sensors at 2.480 and 2.628 m is the largest in the experiment. The pressure traces at this unit Reynolds number show a well organized wave packet that is very well represented by the ensemble average until $z = 2.628$ m. Further downstream, the individual pressure trace shows a high level of amplification in the center of the perturbation that is not well represented by the ensemble average.

These perturbations, although generated by completely different methods, share some similarities with those reported by Casper. High levels of amplification occur in the center of the wave packets, which then transition to turbulence. Occasionally, the transitional wave packets contained higher amplitude fluctuations than the fully turbulent disturbances (see Figure 5.13) although not with the same intensity as

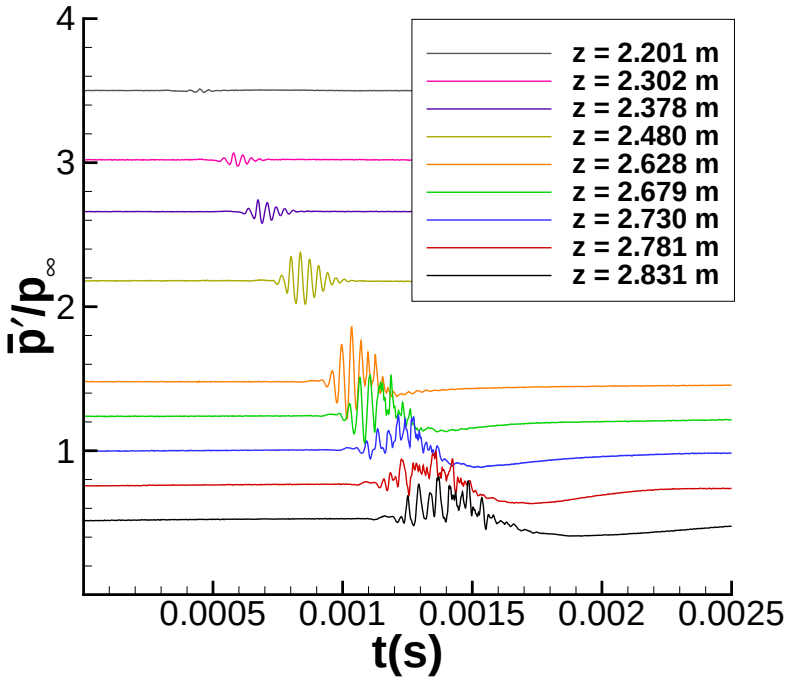

(a) Ensemble average

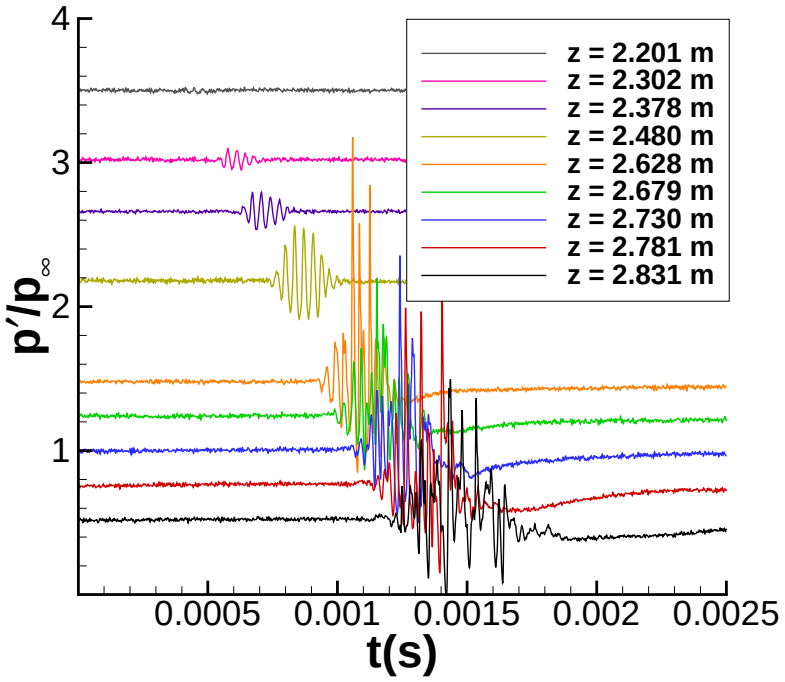

(b) Single perturbation

Figure 5.14. Perturbation generated using a 0.011 inch poppet, $Re = 5.53 \times 10^6/\text{m}$, $p_{0v} = 40$ psig

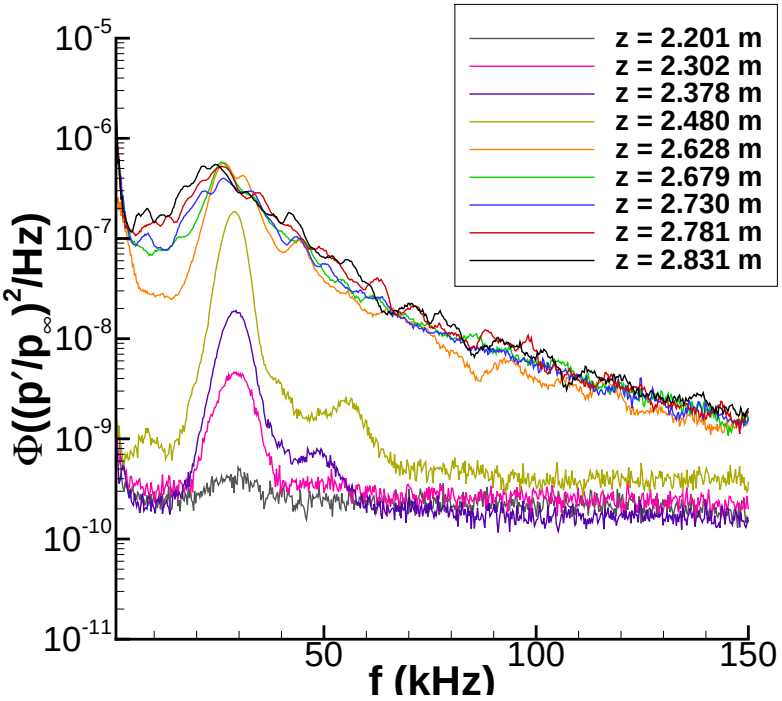

Figure 5.15. Power spectral density for a perturbation generated using a poppet with an 0.011-inch flat, $Re = 5.53 \times 10^6$/m, $p_{0v} = 40$ psig

reported by Casper [5]. However, there are distinct differences as well. There is a noted absence of harmonics, and the presence of the double lobed peaks in the spectra could indicate a breakdown process due to additional frequency content not present in the perturbations generated by Casper. It appears that

The purpose of this study was not to produce instability wave packets, but to perturb the flow in such a way that turbulent spots result very near the perturber location. Perturbations generated in the lower Reynolds number cases transition further upstream than those generated by Casper. However, they still convect a significant distance downstream prior to transition. Additional runs were made using a poppet with the 0.005-inch flat at three different Reynolds numbers at the maximum valve stagnation pressure in order to determine whether instability wave packets could be produced that would transition even sooner. This change again required a realignment of the valve, but permitted study of how the perturber performed at maximum

stagnation pressure under varying tunnel conditions. Figures 5.16 and 5.18 show the perturbations generated with $p_{0v} = 80$ psig at lower freestream Reynolds numbers using the same valve configuration. Figure 4.14 shows the same valve configuration at the maximum quiet pressure.

Figure 5.16 shows a perturbation much further along in the transition process than that generated with a valve stagnation pressure of 40 psig (Figure 5.10). At $z = 2.201$ m the perturbation still shows signs of being a wave packet, but by $z = 2.302$ m the ensemble average is no longer an accurate representation of the fluctuation amplitudes shown in the individual sample. Figure 5.17 shows the spectra for the perturbation. At $z = 2.201$ m, the perturbation shows a broad peak at 30-60 kHz, with possible harmonics near 100 kHz. The pressure traces show a rapid breakdown of the perturbation. By $z = 2.302$ m, the spectra indicate a turbulent perturbation, with broadband noise increasing as the perturbation convects downstream. Once the perturbation is turbulent, the peak frequency decreases incrementally as the perturbation convects downstream.

At $Re = 5.95 \times 10^6$/m (Figure 5.18) the perturbation is still a wave packet at $z = 2.201$ m. As the perturbation convects downstream, second mode amplification and breakdown can be seen in the pressure traces. Again, it primarily occurs in the center of the wave packet. By $z = 2.378$ m the broadband noise above 40 kHz has risen to the levels of fully turbulent flow(Figure 5.19). By the time the perturbation has convected into the pipe insert at $z = 2.628$ m, it has transitioned to turbulence.

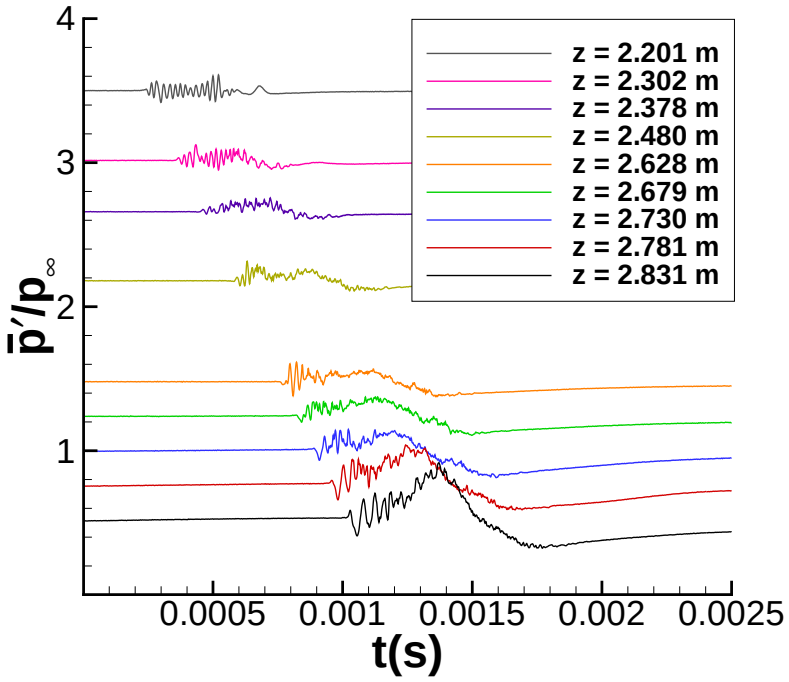

(a) Ensemble average

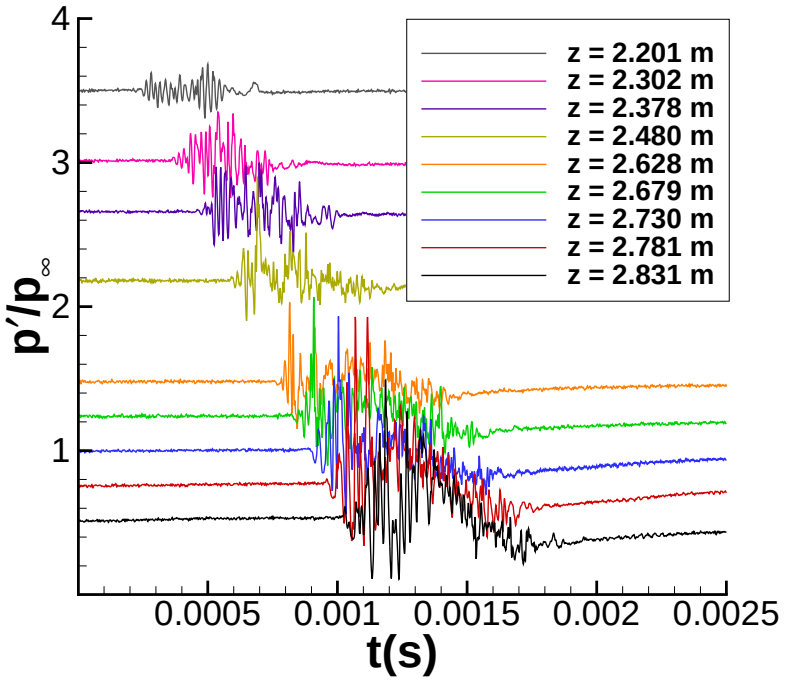

(b) Single perturbation

Figure 5.16. Perturbation generated using a 0.005 inch poppet, $Re = 8.23 \times 10^6/\text{m}$, $p_{0v} = 80$ psig

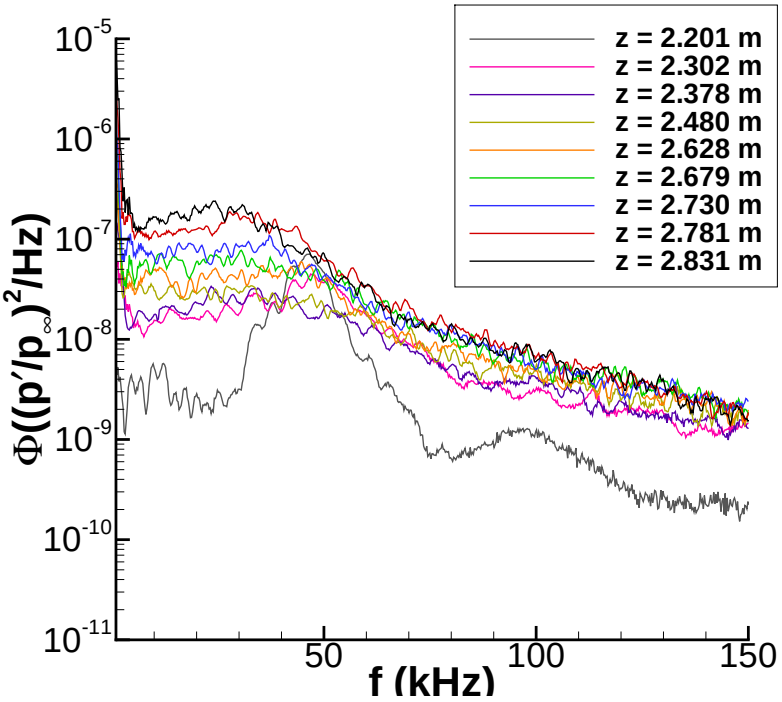

Figure 5.17. Power spectral density for a perturbation generated using a poppet with an 0.005-inch flat, $Re = 8.23 \times 10^6$/m, $p_{0v} = 80$ psig

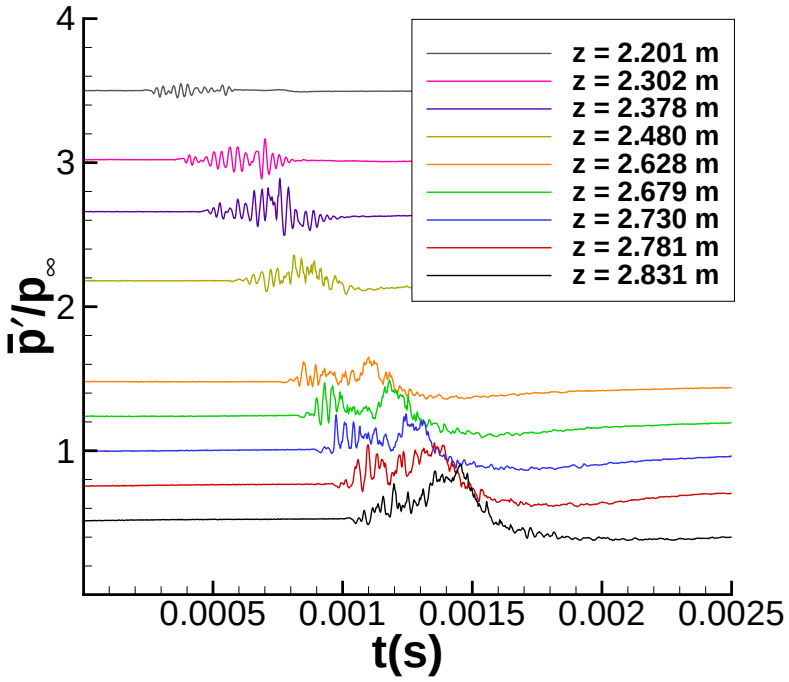

(a) Ensemble average

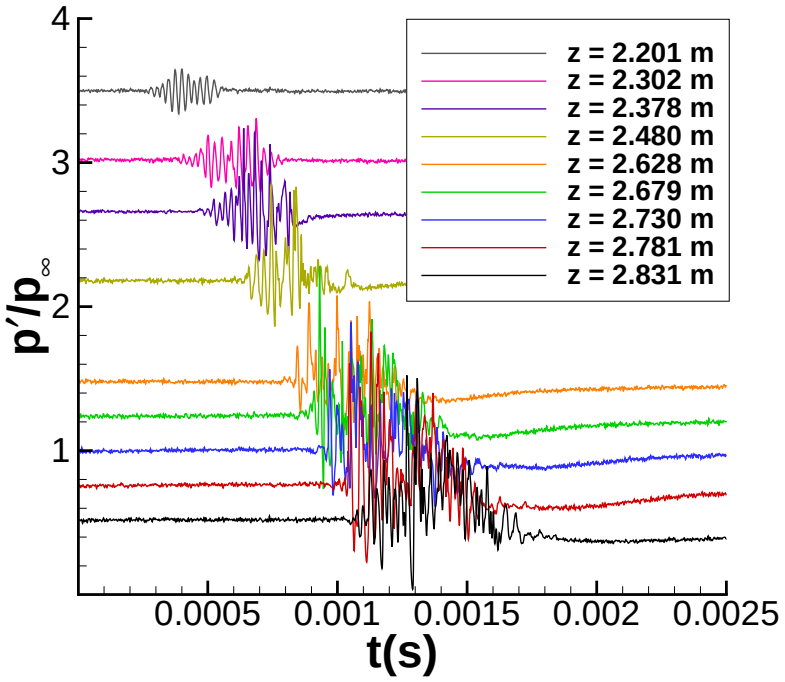

(b) Single perturbation

Figure 5.18. Perturbation generated using a 0.005 inch poppet, $Re = 5.95 \times 10^6/\text{m}$, $p_{0v} = 80$ psig

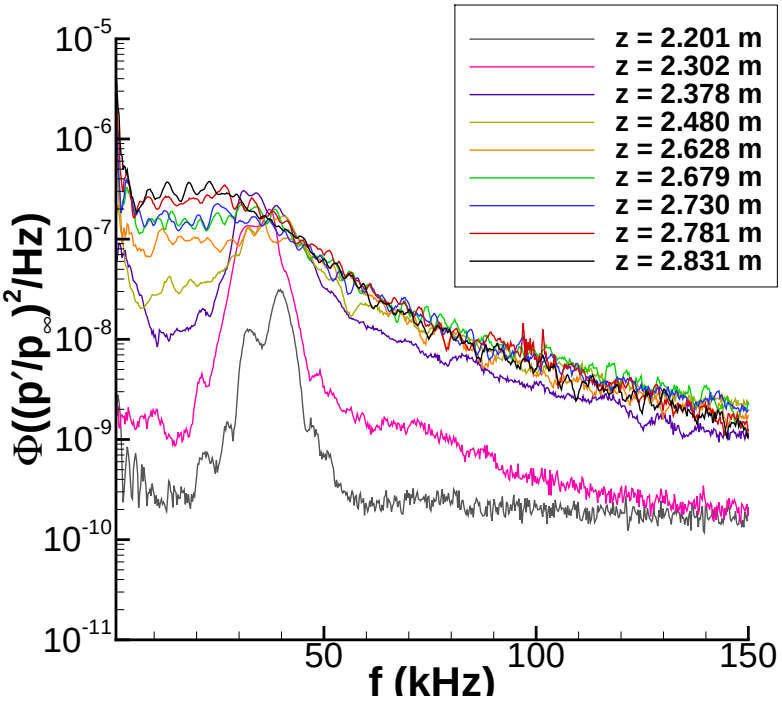

Figure 5.19. Power spectral density for a perturbation generated using a poppet with an 0.005-inch flat, $Re = 5.95 \times 10^6$/m, $p_{0v} = 80$ psig

5.3 Repeatability

The perturber must produce repeatable perturbations in order to be used as a tool in developing a turbulent spot model of transition for hypersonic flow. Figure 5.20 shows the ensemble averaged perturbation overlaid upon several individual samples for a single perturber configuration at a freestream unit Reynolds number of $Re = 12 \times 10^6$/m from a single run. At $z = 2.201$ m, the individual disturbances are well represented by the ensemble average for roughly the first half of the perturbation. The latter half of the perturbation appears to be turbulent, with variation between samples in both the magnitude and phase of the pressure fluctuations.

By $z = 2.302$ m the perturbation is turbulent, and there is great variation between samples. The ensemble average shows the underlying mean static pressure changes. For the perturbations at $z = 2.730\,\text{and}\,2.831$ m, the turbulent fluctuations are averaged out, and the ensemble average gives no indication of the true level of turbulent fluctuations. The ensemble average still accurately displays the local mean pressure level within the perturbations.

At lower freestream unit Reynolds numbers, the perturbations have not yet transitioned to turbulence. As a result the wave packets tend to be well organized. Figure 5.21 shows the perturbation generated at $Re = 5.53 \times 10^6$/m with a 40 psig valve stagnation pressure. At $z = 2.201\text{and}2.302$ m, the perturbation is very repeatable, with little variation between samples. At $z = 2.628$ m the perturbation has begun to break down in the center of the wave packet, but is still well organized at the leading edge, similar to the perturbation shown in Figure 5.20(a). By $z = 2.831$ m, the perturbation is turbulent.

At low Reynolds numbers, the perturbations tend to be instability wave packets. As a result the perturbations tend to be more repeatable. As perturbations convect downstream, the transition process takes place, and the repeatability of the perturbations decreases due to the stochastic nature of turbulence. At higher freestream Reynolds numbers, this process occurs far upstream, or is completely bypassed all

together. As a result, the perturbations contain fully turbulent regions at all measurement locations, and are much less repeatable. Further studies of the perturbations are needed to determine whether the perturber is repeatable from run to run. It is unrealistic to expect turbulent perturbations to be fully repeatable due to the stochastic nature of turbulence.

Additionally, the statistical stability of the perturbations is important when developing a turbulent spot model of transition. In order to determine how statistically stable the perturbations were, the RMS amplitude was calculated for each of the 50 samples used to generate the ensemble averaged perturbations. The mean and standard deviation were computed for each of the RMS values, and the coefficient of variation (standard deviation/mean $\times$ 100) was calculated. Figure 5.22 is a plot of the coefficient of variation for the data presented in Sections 4.3 and 5.2. There appears to be a trend in the coefficient of variation near the maximum quiet freestream Reynolds number in the wind tunnel, indicated by the black symbols. At the first two to three sensors, the coefficient of variation ranges from $10-18\%$. As the perturbation convects further downstream, the coefficient of variation drops to between 5 and 8%. Finally, at the last two sensors, the level of variation rises again in some cases, to between 14 and 19%. This final rise appears to be due to the growth of the second mode waves trailing the perturbations, as the cases with using the poppets with the 0.005 and 0.009 inch flats did not show the high levels of variation, and lacked the high levels of second mode wave growth. The instability wave packets showed higher levels of variation from perturbation to perturbation. Each color symbol represents an approximate Reynolds number range. As the perturbations transitioned, the variation levels dropped. As the freestream Reynolds number drops, the perturbation shows high levels of variation further and further downstream. Lastly, the 80 psig valve stagnation pressure case at a $Re = 5.95 \times 10^6$/m seems counter intuitive at first. However, the higher valve stagnation pressure resulted in transition by $z = 2.628$ m, despite the low freestream Reynolds number. This is why the coefficient of variation drops to the turbulent levels for the last five sensor locations for this case.

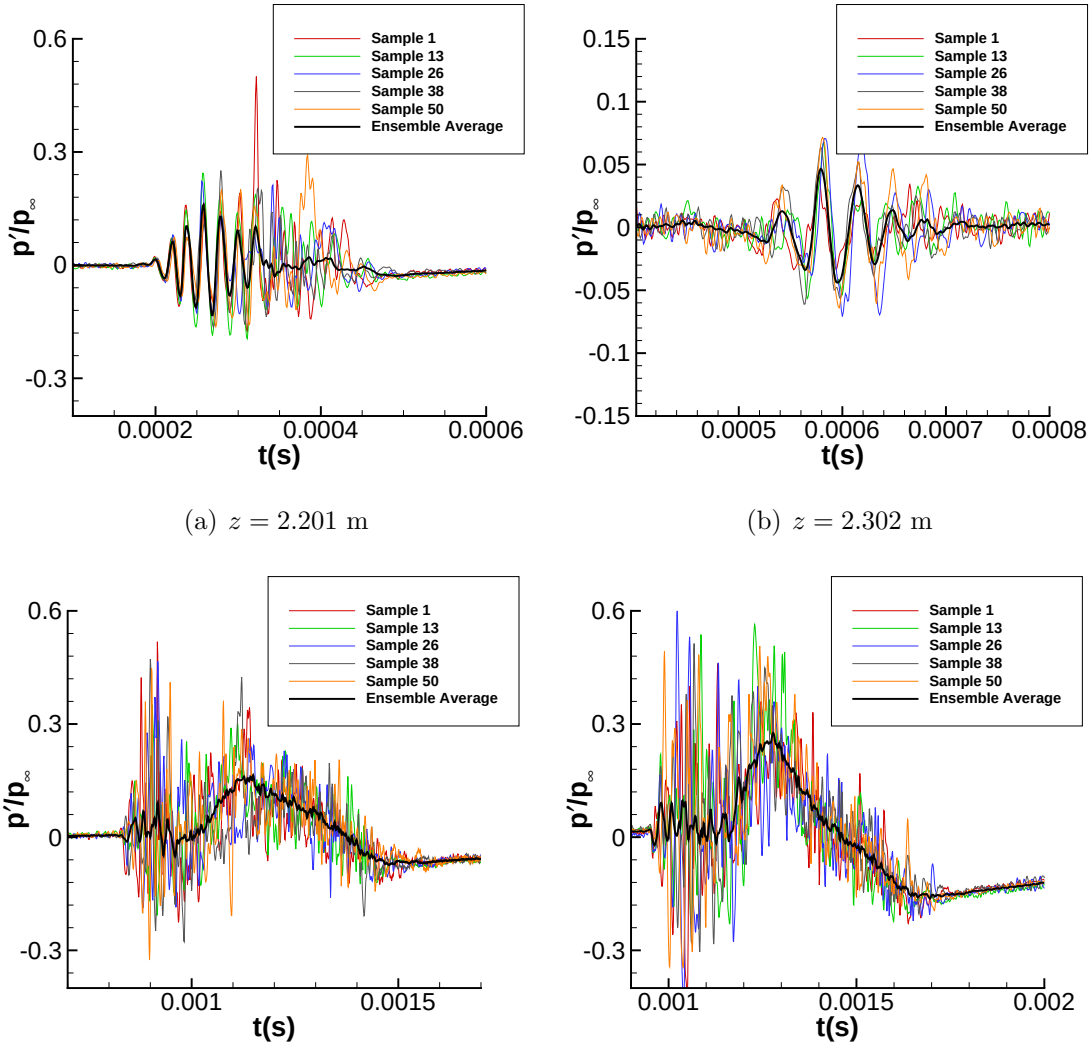

(a) $z = 2.201$ m

(b) $z = 2.302$ m

(c) $z = 2.730$ m

(d) $z = 2.831$ m

Figure 5.20. Comparison of ensemble averaged to individual samples generated using a 0.005 inch poppet, $Re = 12.0 \times 10^6/\text{m}, p_{v0} = 80$ psig.

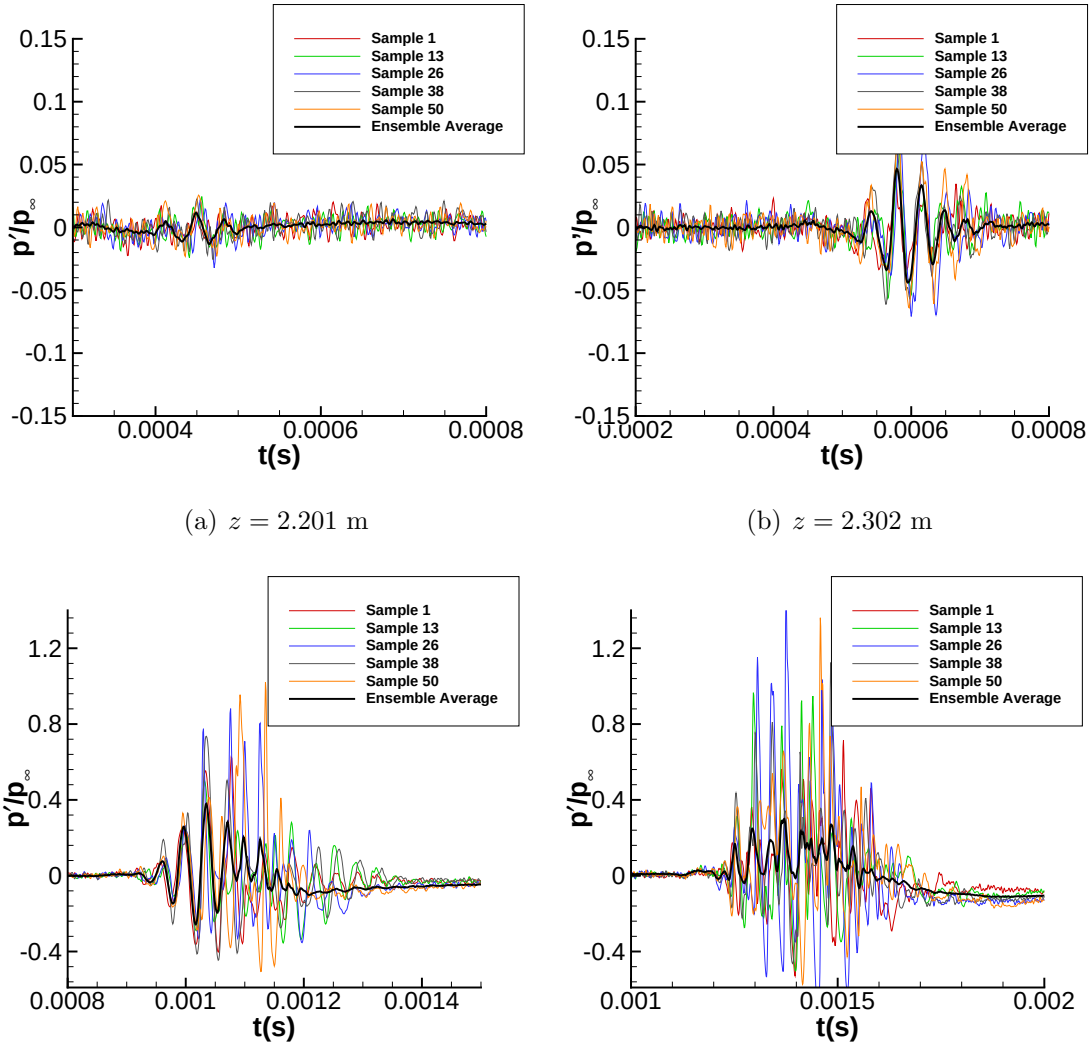

(a) $z = 2.201$ m

(b) $z = 2.302$ m

(c) $z = 2.628$ m

(d) $z = 2.831$ m

Figure 5.21. Comparison of ensemble averaged to individual samples generated using a 0.005 inch poppet, $Re = 5.53 \times 10^6/\text{m}, p_{v0} = 40$ psig.

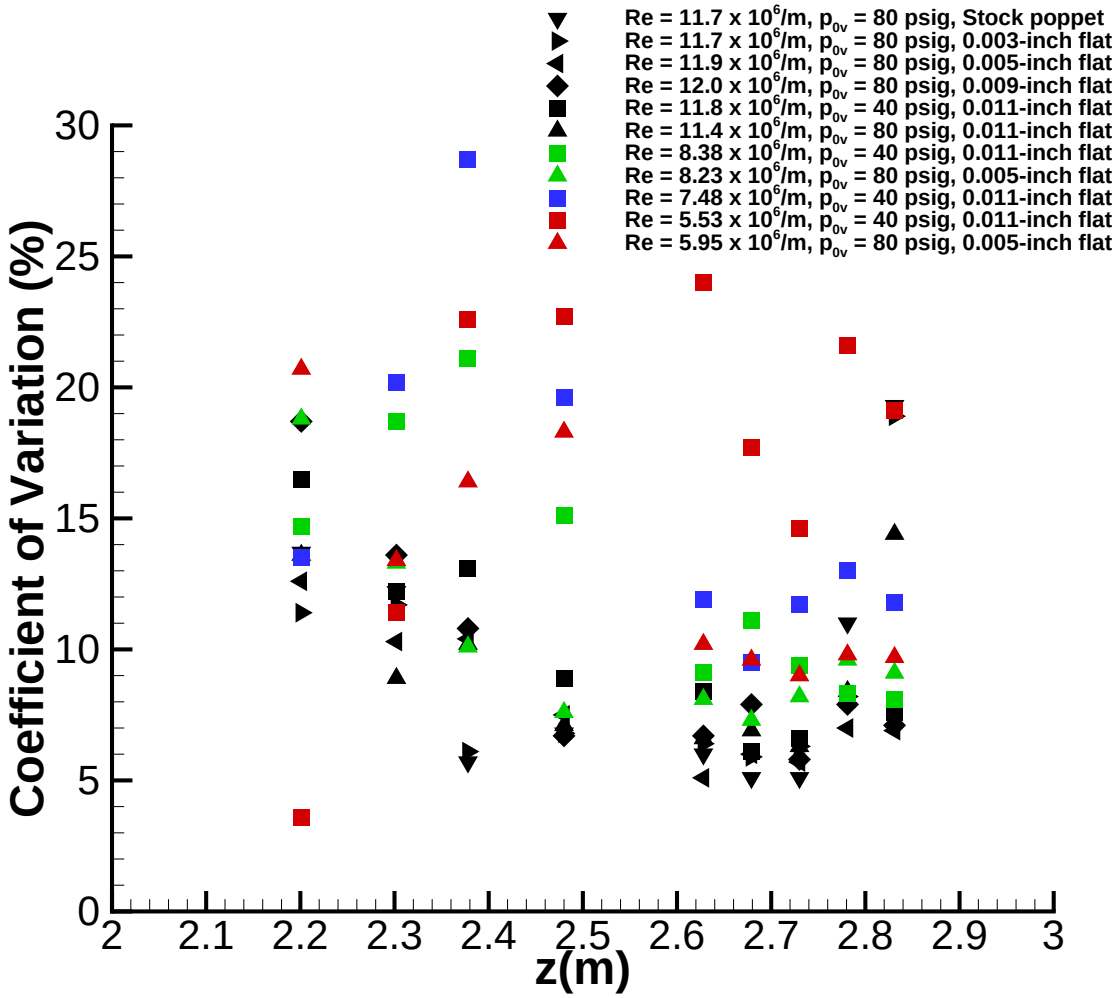

Figure 5.22. Coefficient of Variation(%) of individual perturbations for various valve configurations and tunnel conditions.

5.4 Development of a Valve Alignment Tool

The development of an accurate and repeatable alignment procedure for the Parker valve became one of the project's largest obstacles. An appropriate test apparatus had to be developed in order to consistently align the perturber system. The previous iteration of the BAM6QT diffuser section was already in use as a vacuum test cell, and the modifications made to configure the diffuser test cell for perturber alignment are documented in Chapter 3. The jet will behave differently when injected into the test cell than rather than into the nozzle wall boundary layer, but the jet response in a quiescent flow should be a useful tool for analysis of the performance of the perturbation.

The alignment apparatus was used during July, 2013. Tests were made to determine how the perturber alignment signal compared to the perturbations generated during a run in the BAM6QT immediately following alignment. In quiet flow conditions in the BAM6QT, the Mach 6 freestream flow results in a pressure ratio (p_0/p_∞) of about 1579. During a run near maximum quiet conditions, the freestream static pressure is approximately 0.1 psia. In practice the static pressure varies by approximately 4% during the 0.5 second data collection window. While the test cell is capable of reaching a vacuum of 0.1 psia or lower, leaks caused the pressure to vary slightly between 0.08-0.1 psia during alignment testing. Figure 3.6 shows an image of the test cell located in the downstairs portion of room 29B.

5.4.1 Test Cell Preparation

Prior to reducing the pressure in the test cell, the valve must be mounted to the acrylic faceplate of the test cell. In order to speed up the alignment process, the valve was operated prior to being attached to the acrylic flange of the test cell. Once assembled in the desired configuration, the tactile alignment method was used for gross alignment of the valve to the point that a jet was being produced. At this point

the valve was mounted to the acrylic flange. Once mounted, the alignment process proceeded as follows.

1. Reduce pressure in the test cell to the 0.08-0.1 psia range
2. Turn on the perturber
3. Rotate the valve coil relative to the body until a perturbation of desired duration is produced (See schematic in Figure 4.2)
4. Tighten set screws to lock perturber alignment
5. Check to ensure that tightening the set screws did not shift the alignment
6. Turn off perturber electronics and close off air supply
7. Remove air supply from valve by unscrewing the instrument fitting

Once this procedure was completed, the valve was removed from the test assembly and transfered to the tunnel for use during a run. Care was taken to handle the valve in such a way as to not shift the alignment. When the compressed air supply was removed, and then reattached by the tunnel, a torque had to be applied to the valve coil to unscrew the instrument fitting that connected the pressurized air supply. During this step, the valve was held only by the valve coil, to prevent the application of a torque that could rotate the valve body relative to the valve coil (See Figure 4.2).

5.4.2 Test Apparatus Response and Resulting Perturbations

A typical test signal from the Kulite mounted directly opposite the valve exit orifice can be seen in Figure 5.23 (see Figure 3.7 for clarity). The signal is calibrated using the manufacturer calibration from Kulite Semiconductors. It was planned to calibrate the sensor at the end of the test cycle, but the sensor failed prior to the end of testing. The test signal is characterized by a rapid increase in pressure followed by a rapid decrease to approximately half of the maximum pressure. From this point, the

pressure level of the transverse jet rebounds briefly before decaying back to ambient levels. It is clear that a certain jet intensity is required to produce a perturbation, but the exact intensity required is unknown at this time. Figure 5.24 compares the response for two different valve configurations. Each valve configuration was aligned, and then run at the maximum quiet freestream Reynolds number. Both cases show that the Kulite sensor is well below its maximum measurement range, and could be moved closer to the exit of the nozzle wall spacer to increase signal levels. However, the lower intensity jet failed to produce a measurable boundary-layer perturbation when injected during a tunnel run.

Figure 5.25 shows the averaged responses from four separate valve configurations aligned to produce similar duration jets in the test cell. The pressure traces shown were generated immediately after each configuration was aligned. There is poor agreement between the perturbations and the measured response within the test cell. The most misleading data are from two separate runs. The first used a stock poppet with a larger exit orifice for the valve. The passage through the nozzle wall was the same 0.039-inch diameter. The alignment signal indicated a very strong perturbation. The resulting perturbation consisted of a double burst of relatively weak amplitude. The alignment signal generated by the valve equipped with a poppet featuring a 0.003-inch flat was both the weakest and the shortest duration. The perturbation generated with this configuration was by far the longest in duration, and additionally was of a high amplitude.

The disagreement between the test apparatus results and the results in the Mach-6 tunnel likely points to an inability to maintain alignment during the transfer between the test cell and the nozzle wall. While the injection of a transient underexpanded jet into quiescent flow will be different from an injection into crossflow, correlation between the two disturbances was expected. It is likely that the valve alignment shifts during the transfer of the valve from the alignment test cell to the tunnel. The process consists of removing the pressurized air line from the valve on the test cell, and unbolting the valve from the test cell. The valve is then carried upstairs where

pressurized air is reattached, and the valve is bolted to the 2.5-inch nozzle-wall insert. The stability of the valve alignment must be improved in order for the perturber to be useful for measuring statistical properties of turbulent spots. It is unknown what causes the shift in valve alignment to occur.

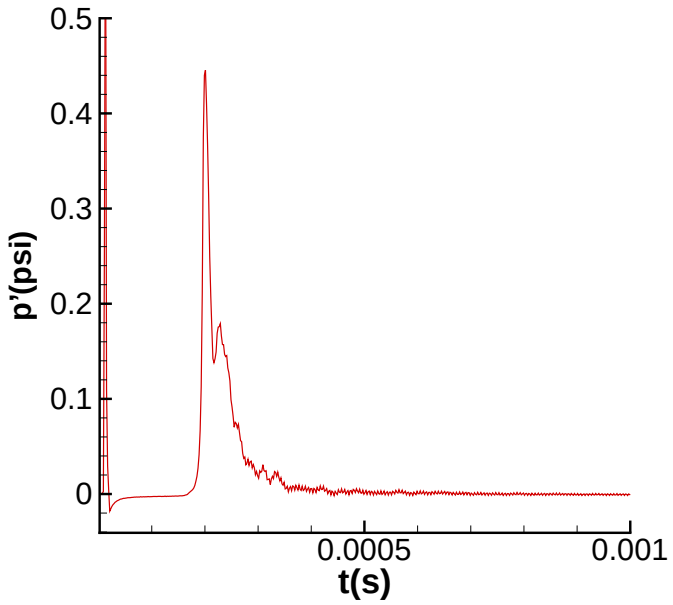

Figure 5.23. Sample signal using alignment apparatus. $p_{0v} = 60$ psig, stock poppet.

It was planned to test the realignment of a single valve configuration. The plan was to find a suitable valve configuration during testing, and then to align the valve and use it to perturb the flow in the BAM6QT. Once this step was completed the valve would be disassembled and then realigned and used for an additional run. Unfortunately, the Kulite mounted in the test cell failed before this test could be completed. The Kulite mounted in the test cell used an A-screen, which leaves the sensor diaphragm exposed via a large central orifice. It was assumed that the filtered air would prevent failure of this diaphragm due to particulate damage. Unfortunately this was not the case, and the sensor diaphragm was pierced. Future tests should utilize a B-screen Kulite, which features 8 holes distributed around the periphery of the sensor to protect the diaphragm from particulate matter.

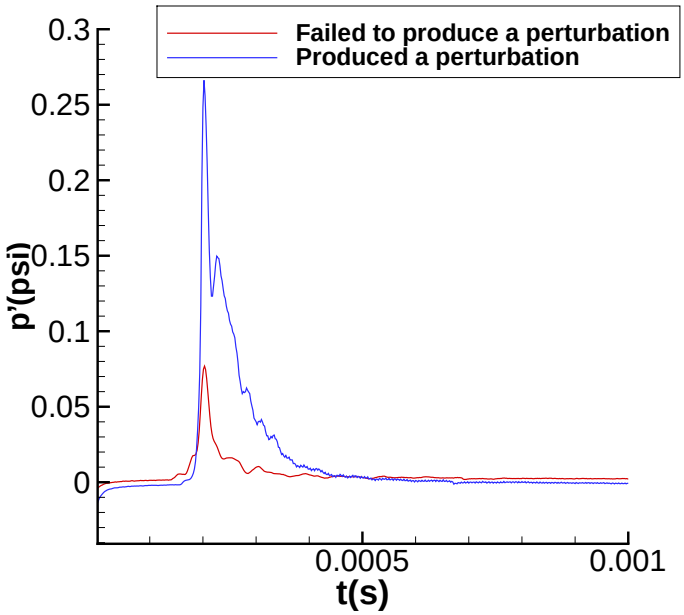

Figure 5.24. Comparison of two different measured jet intensities for two valve configurations run at maximum quiet freestream Reynolds numbers. $p_{0v} = 60$ psig.

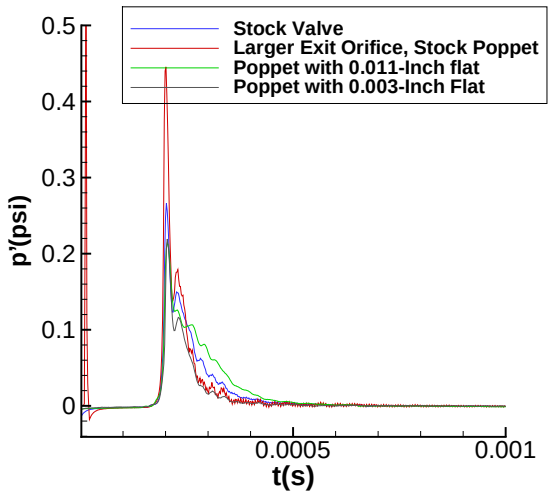

(a) Test apparatus signal

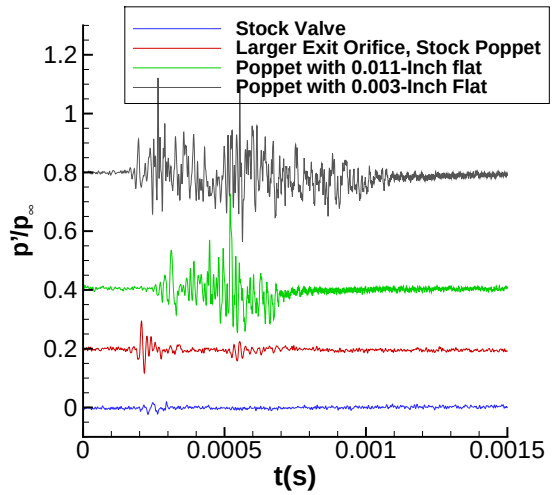

(b) Pressure traces of perturbations at $z = 2.055$ m, taken immediately after valve alignment

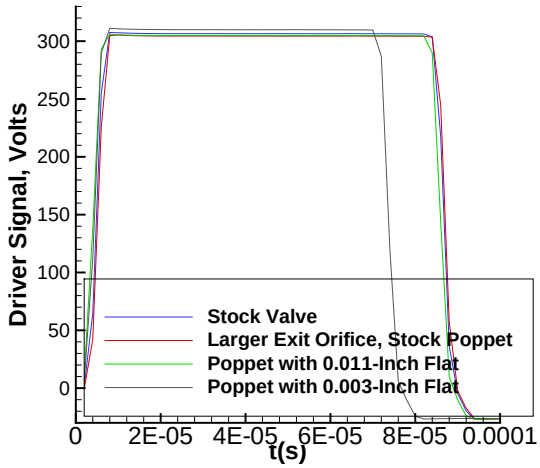

(c) Driver signal

Figure 5.25. Comparison of four similar perturbations with similar alignment signals. $Re \approx 11.5 \times 10^6/\text{m}, p_{0v} = 60psig$

6. Development of a new electronic perturber

6.1 Electrical Breakdown of Air

The electrical breakdown of any material is defined as the *transformation of a nonconducting material into a conductor as a result of applying to it a sufficiently strong field* [48]. Air will break down between two electrodes if a strong enough voltage is applied. Depending on the level of applied voltage, different electrical discharges can be produced.

Ionization of individual electrons due to external sources of radiation can sustain small currents between the electrodes at low applied voltages. Increasing the applied voltage imparts enough energy to cause the free electrons to ionize nearby electrons. This process repeats over and over causing an electron avalanche. This sudden increase in ionization occurs with only a small increase in voltage until the breakdown voltage is reached. Electrical breakdown is considered a threshold process. Once the applied voltage has reached the threshold voltage, the current saturates and is no longer dependent on the applied voltage. The breakdown voltage depends on the gas, the electrode spacing, and the gas pressure and is governed by Pashcen's Law, which states that for a given gas the breakdown voltage is dependent only on the product of the pressure (p) and the electrode spacing(d). Raizer gives experimental measurements of $pd_{min} = 0.759$ Pa-m with a $V_{min} = 330$ V for the breakdown of air [48].

At the breakdown voltage, the discharge is defined as a Townsend Dark Discharge, which is characterized by low levels of current and produces no emission of light. As the applied voltage is increased beyond the breakdown voltage, the discharge becomes a glow discharge. This discharge is marked by a drop in voltage, a rise in current, and the visible emission of light. As the applied voltage is further increased within the

glow discharge region, the current density at the cathode remains the same. What serves to increase the current is the area of the cathode that is utilized by the glow discharge.

Once the entire cathode surface is covered by the glow discharge, further increase in the applied voltage results in the current density at the cathode increasing. The discharge is now considered an abnormal glow discharge. If the applied voltage is further increased, the discharge will cascade into an arc discharge, characterized by a low voltage and high currents typically above 1 A.

6.2 Previous Glow Perturbers in the BAM6QT

Casper's work relied solely on the generation of turbulent spots through the use of a pulsed glow perturber [5]. This proved effective at producing instability wave packets, but failed to produce turbulent spots near the perturber. As these instability wave packets convected downstream, non-linear wave growth would occur, leading to transition. This process required a significant portion of the measurement region of the BAM6QT nozzle wall. As a result, Casper was only capable of measuring young turbulent spots.

Casper was able to produce a spark discharge which resulted in a much larger perturbation, but the spark generated electromagnetic interference (EMI). This rendered the spark perturbations of no use, and the resulting perturbations were eliminated from Casper's data set for analysis. With Capser's glow perturber, sparks ocurred randomly during the initial rise in voltage of a pulsed glow perturbation.

In order to improve the measurement of turbulent spots, a new electronic perturber that could produce much higher amplitude pulsed glow perturbations or well controlled spark discharges is being designed. The basis of this design is the Behlke HTS-121-01-HB-C (formerly HTS-121-01-HB-03) High Voltage Transistor Switch. The switch is capable of a maximum current of 15 A and a maximum voltage of 12 kV. Additionally the switch is capable of highly controlled operation, with on

times as low as 70 ns. The high voltage circuit is powered by a Universal Voltronics BRC 4000 which is capable of supplying 10 kV DC with a current of 400 mA.

The benefit of using the Behlke HVT switch is additional control. The switch is triggered through the use of a TTL signal to turn the high voltage signal on and off. This is an improvement in control over the perturber system used by Casper. Casper's design was limited by the ringing of the automotive ignition coil used to provide the high voltages required for the pulsed glow. After one ringing cycle, a current was fed back into the ignition coil to reduce the inductive ringing of the circuit.

6.3 Circuit Design

The development of the circuit for the new electronic perturber is still in its initial phases. Initial layout of the circuit has not been conducted due to extended shipping delays for the Behlke transistor. Now that the key components are in stock, work can begin on the detailed design of the perturber. Future work should include the detailed design of the perturber circuit as well as the shakedown of the system and the measurement of the discharges produced in the test cell. Once the perturbation is understood in the test cell, and deemed sufficient, the perturber should be used in the BAM6QT to determine the perturber's ability to produce high amplitude perturbations. Circuit design will be assisted by Evan Meyerhoff of High Voltage Connection and Scott Stanfield of the Air Force Research Lab.

7. Conclusions and Future Work

A Parker 009-1699-900 pulse valve was used to generate perturbations in a Mach 6 boundary layer. The perturbations were generated by injecting a transverse jet into the BAM6QT nozzle-wall boundary layer. Perturbations generated with the stock system had a duration that was longer than desired. As a result the system was modified. Elimination of a low voltage pulse designed to hold the valve open reduced the duration of the perturbation by 300 μs to approximately 600 μs at the first sensor location 27.7 cm downstream of the perturber. Other methods of reducing the perturbation duration had mixed results. Shorter duration perturbations were achieved by modifying the poppets internal to the valve, but the results were inconsistent. During this process, the intensity of the jet was judged using the author's finger. In order to accurately compare different valve configurations, it became clear that a more objective alignment method was necessary in order to produce consistent disturbance amplitudes.

Perturbations were made at freestream unit Reynolds numbers from $Re = 5.53 - 11.7 \times 10^6/$ m, and pressure fluctuations were measured downstream. At lower unit Reynolds numbers, the perturbations were initially second-mode instability wave packets, similar to those seen by Casper [5]. The transition process appears similar to that reported by Casper, with breakdown occurring in the middle of the perturbations. The second-mode wave packets grow and break down, but there is additional low frequency content in the form of a double-lobed peak seen in the spectra during the transition process, where Casper showed a single frequency peak. The present data showed the growth of spectral peaks followed by a rise in broadband noise, similar to Caspers' data. Additionally, there was a marked reduction in harmonics when compared to Casper's data.

The perturber was capable of making fully turbulent perturbations at the maximum quiet freestream Reynolds number of the BAM6QT. This is a major step forward in measuring the growth rates of mature turbulent spots. At lower Reynolds numbers, the perturber still resulted in turbulent spots well upstream of Casper's data, including those that would transition at Reynolds numbers which never resulted in transition using Casper's perturber.

An apparatus was designed in order to aid in aligning the valve to improve the consistency of operation. Unfortunately, the alignment apparatus seemed to be ineffective as a tool for alignment of the perturber. Alignment signals varied greatly from the perturbations generated within the BAM6QT, suggesting a high level of difficulty in maintaining the alignment when transferring the valve from the alignment apparatus to the BAM6QT nozzle wall.

As a result of the inconsistencies encountered during the course of this project, additional refinement of the perturber is recommended prior to using it as a tool for generating turbulent spots. The perturber has shown some promise, as it is capable of producing fully turbulent perturbations prior to the first sensor available in the BAM6QT, at $z = 2.055$ m. Additionally, even at lower unit Reynolds numbers, the perturbations transitioned to turbulence, something Casper was unable to achieve using a pulsed glow perturber. It is unclear whether or not the perturbations are true turbulent spots, given the moderately long durations currently achieved, but the approach seems promising if further improvements can be achieved.

7.1 Future Work

The largest difficulty encountered in the course of this project was consistent alignment of the valve. Additional modifications to the valve to increase the precision of the valve adjustment are worth investigating. The stock valve is aligned using by threading the valve together. The relatively coarse thread pitch results in the entire operational regime being traversed in approximately 30° of rotation, which presents

a two fold problem. Aligning the valve is difficult, and once aligned, a slight rotation can greatly alter the performance. Increasing the thread count could significantly improve the performance of the system, as would another method that reduced the variability of the alignment. This would allow the perturber to be adjusted with less error, as well as reduce the effects of slight adjustments once the valve is aligned. Further refinement of the existing method should be pursued. A new method of alignment would be desirable.

Additional work should be done to investigate the geometry of the passage through the nozzle wall of the BAM6QT. Of great interest is the effect of increasing the orifice diameter and decreasing the length. Sinclair and Robins noted that for a pressure tap, the time lag (or in this case equalization time) was directly proportional to the length of the passage, and inversely proportional to the fourth power of the diameter [49]. Varying the diameter could help reduce the duration of the blow-down portion of the perturbation, and the test cell could provide an easily accessible test apparatus to see if improvements are possible.

Lastly, development of the electronic perturber system should be completed. The major long lead parts have finally arrived, and circuit design can begin. It is likely that a fully electronic perturber will be more repeatable due to improved precision. It is unclear if the limitations of low amplitude disturbances and high levels of electromagnetic interference can be overcome. However, the new system appears promising, and preliminary testing should be completed to determine its viability as a flow perturber for the generation of turbulent spots.

LIST OF REFERENCES

LIST OF REFERENCES

[1] R.L. Wright and E.V. Zoby. Flight boundary layer transition measurements on a slender cone at Mach 20. AIAA Paper 77-719, June 1977.

[2] Steven P. Schneider. Effects of high-speed tunnel noise on laminar-turbulent transition. *Journal of Spacecraft and Rockets*, 38(3):323–333, May–June 2001.

[3] S. Park and G. C. Lauchle. Wall pressure fluctuation spectra due to boundary-layer transition. *Journal of Sound and Vibration*, 319:1067–1082, 2009.

[4] K .M. Casper, S.J. Beresh, and S.P. Schneider. Spanwise growth of the turbulent spot pressure-fluctuation field in a hypersonic boundary layer. AIAA Paper 2011-3873, June 2011.

[5] K. M. Casper. *Pressure Fluctuations Beneath Instability Wave Packets and Turbulent Spots in a Hypersonic Boundary Layer*. PhD thesis, Purdue University School of Aeronautics and Astronautics, August 2012.

[6] L. Krishnan and N.D. Sandham. On the merging of turbulent spots in a supersonic boundary-layer flow. *International Journal of Heat and Fluid Flow*, 27:542–550, 2006.

[7] H. W. Emmons. The laminar-turbulent transition in a boundary layer - part 1. *Journal of the Aerospace Sciences*, 19:490–498, July 1951.

[8] M. Mitchner. Propagation of turbulence from an instantaneous point disturbance. *Journal of the Aeronautical Sciences*, 22:350–351, January 1954.

[9] G. B. Schubauer and P. S. Klebanoff. Contributions on the mechanics of boundary-layer transition. NACA Report 1289, February 1955.

[10] R. Narasimha. On the distribution of intermittency in the transition region of a boundary layer. *Journal of Aerospace Sciences*, 24:711–712, May 1957.

[11] S. Dhawan and R. Narasimha. Some properties of boundary layer flow during the transition from laminar to turbulent motion. *Journal of Fluid Mechanics*, 3:418–436, January 1958.

[12] R. Narasimha. The laminar-turbulent transition zone in the boundary layer. *Progress in Aerospace Sciences*, 22:29–80, 1985.

[13] Mohamed Gad el Hak, Ron F. Blackwelder, and James J. Riley. On the growth of turbulent regions in laminar boundary layers. *Journal of Fluid Mechanics*, 110:73–95, 1981.

[14] J. W. Elder. An experimental investigation of turbulent spots and breakdown to turbulence. *Journal of Fluid Mechanics*, 9(02):235–246, October 1960.

[15] A. E. Perry, T. T. Lim, and E. W. Teh. A visual study of turbulent spots. *Journal of Fluid Mechanics*, 104:387–405, 1981.

[16] R. A. Antonia, A. J. Chambers, M. Sokolov, and C. W. Van Atta. Simultaneous temperature and velocity measurements in the plane of symmetry of a transitional turbulent spot. *Journal of Fluid Mechanics*, 108:317–343, 1981.

[17] E. Gutmark and R. F. Blackwelder. On the structure of a turbulent spot in a heated laminar boundary layer. *Experiments in Fluids*, 5:217–229, 1987.

[18] R. Sankaran, M. Sokolov, and R. A. Antonia. Substructures in a turbulent spot. *Journal of Fluid Mechanics*, 197:389–414, 1988.

[19] D. Henningson, P. Spalart, and J. Kim. Numerical simulations of turbulent spots in plane Poiseuille and boundary-layer flow. *Physics of Fluids*, 10:2914–2917, October 1987.

[20] J. A. Redford, N. D. Sandham, and G. T. Roberts. Numerical simulations of turbulent spots in supersonic boundar layers: Effects of Mach number and wall temperature. *Progress in Aerospace Sciences*, 52:67–79, 2012.

[21] F. W. Chambers and A. S. W. Thomas. Turbulent spots, wave packets, and growth. *Physics of Fluids*, 26:1160–1162, May 1983.

[22] A. Glezer, Y. Katz, and I. Wygnanski. On the breakdown of the wave packet trailing a turbulent spot in a laminar boundary layer. *Journal of Fluid Mechanics*, 198:1–26, 1989.

[23] B. Cantwell, D. Coles, and P. Dimotakis. Structure and entrainment in the plane of symmetry of a turbulent spot. *Journal of Fluid Mechanics*, 87:641–672, 1978.

[24] I. Wygnanski, M. Sokolov, and D. Friedman. On a turbulent 'spot' in a laminar boundary layer. *Journal of Fluid Mechanics*, 78:785–819, 1976.

[25] I. Wygnanski, M. Zilbermand, and J. H. Haritonidis. On the spreading of a turbulent spot in the absence of a pressure gradient. *Journal of Fluid Mechanics*, 123:69–90, 1982.

[26] M. C. Fischer. Spreading of a turbulent disturbance. *AIAA Journal*, 10:957–959, July 1972.

[27] A. H. Haidari and C. R. Smith. The generation and regeneration of single hairpin vortices. *Journal of Fluid Mechanics*, 277:135–162, 1994.

[28] H. Makita and A. Nishizawa. Characteristics of internal vortical structures in a merged turbulent spot. *Journal of Turbulence*, July 2001.

[29] L. Krishnan and N. D. Sandham. On the merging of turbulent spots in a supersonic boundary-layer flow. *International Journal of Heat and Fluid Flow*, 27:542–550, 2006.

[30] C. S. James. Observations of turbulent-burst geometry and growth in supersonic flow. Technical Note 4235, NACA, April 1958.

[31] L. Krishnan and N. D. Sandham. Effect of Mach number on the structure of turbulent spots. *Journal of Fluid Mechanics*, 566:225–234, 2006.

[32] L. M. Mack. Boundary layer linear stability theory. Report 709, Special Course on Stability and Transition of Laminar Flow, March 1984.

[33] V. A. Zharov, H. Htun, and Y. I. Khlopkov. Statistical modeling of the turbulent transition in the boundary layer. *Journal of Applied Mechanics and Technical Physics*, 50:742–746, 2009.

[34] S. P. Schneider, C. E. Haven, J. B. McGuire, S. H. Collicott, D. Ladoon, and L. A. Randall. High-speed laminar-turbulent transition research in the Purdue quiet-flow Ludwieg tube. AIAA Paper 94-2504, June 1994.

[35] S. P. Schneider. Development of hypersonic quiet tunnels. *Journal of Spacecraft and Rockets*, 45:641–664, July 2008.

[36] Erick O. Swanson. Mean flow measurements and cone flow visualization at Mach 6. Master's thesis, Purdue University School of Aeronautics and Astronautics, December 2002.

[37] C. Doerge. Pulsed Valve Driver Model IV Manual. Jonathan W. Amy Facility for Chemical Instrumentation, Purdue University Department of Chemistry, February 1999.

[38] S. J. Beresh, J. F. Henfling, R. W Spillers, and B. O. M. Pruett. Measurements of fluctuation wall pressures beneath a supersonic turbulent boundary layer. AIAA Paper 2010-305, January 2010.

[39] E. F. Spina and C. B. McGinley. Constant-temperature anemometry in hypersonic flow: critical issues and sample results. *Experiments in Fluids*, 17:365–374, 1994.

[40] Shann J. Rufer. *Hot-wire Measurements of Instability Waves on Sharp and Blunt Cones at Mach 6.* PhD thesis, Purdue University School of Aeronautics and Astronautics, December 2005.

[41] Bradley M. Wheaton. Roughness-induced instability in a laminar boundary layer at Mach 6. Master's thesis, Purdue University School of Aeronautics and Astronautics, December 2009.

[42] Virgil A. Sandborn. *Resistance Temperature Transducers.* Metrology Press, 1972.

[43] T. B. Hedley and J. F. Keffer. Turbulent/non-turbulent decisions in an intermittent flow. *Journal of Fluid Mechanics*, 64:625–644, 1974.

[44] C. Y Ching and J. E LaGraff. Measurements of turbulent spot convection rates in a transitional boundary layer. *Experimental Thermal and Fluid Science*, 11:52–60, 1995.

[45] Parker Hannifin Precision Fluidics. *Pulse Valves Series 9 Ultra Low Leak Extreme Performance Valve*, September 2009. ppfinfo@parker.com.

[46] K. M. Casper. Private Communication email, September 9, 2013.

[47] K. M. Casper. Private Communication email, August 21, 2013.

[48] Y. P. Raizer. *Gas Discharge Phsysics.* Springer, 2nd edition, 1997.

[49] A. R. Sinclair and A. W. Robins. A method for the determination of the time lag in pressure measuring systems incorporating capillaries. NACA TN 2793, September 1952.

APPENDICES

A. Experimental Hardware Drawings

This chapter contains drawings for the modifications made to the pulse valve poppet, as well as the nozzle wall hardware and the alignment apparatus.

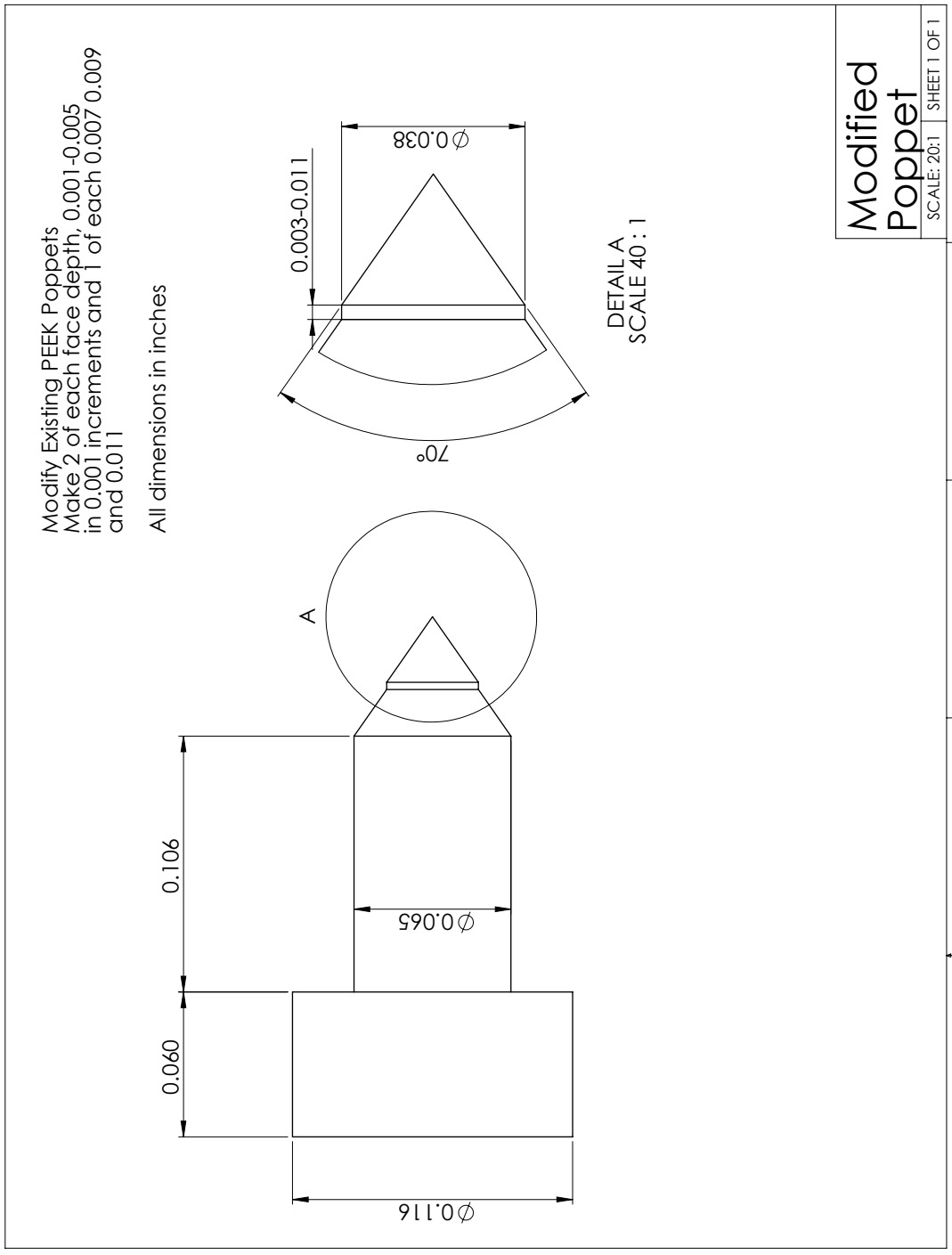

Figure A.1. Modified poppet.

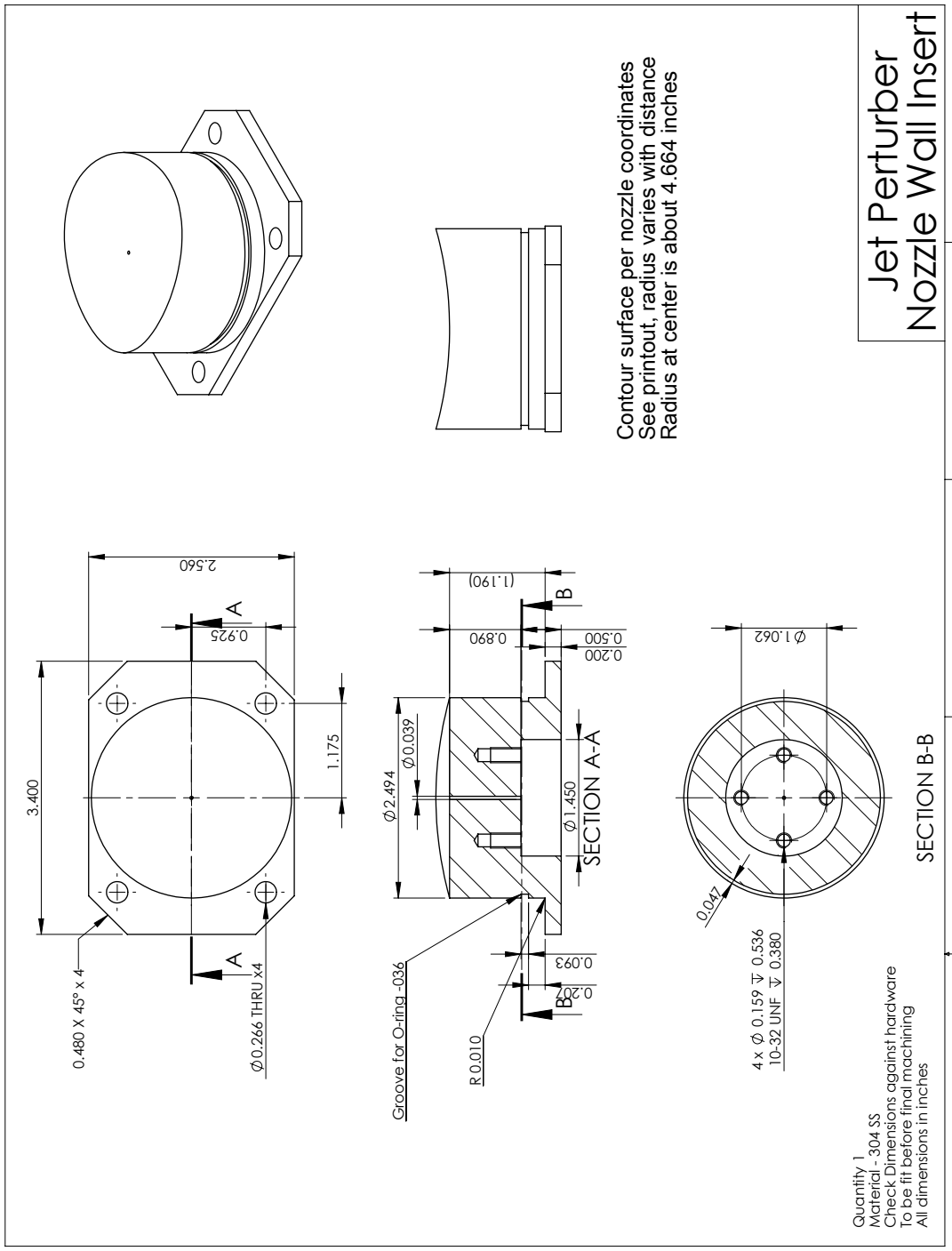

Figure A.2. Nozzle-wall insert for passage of underexpanded jet through the BAM6QT nozzle wall.

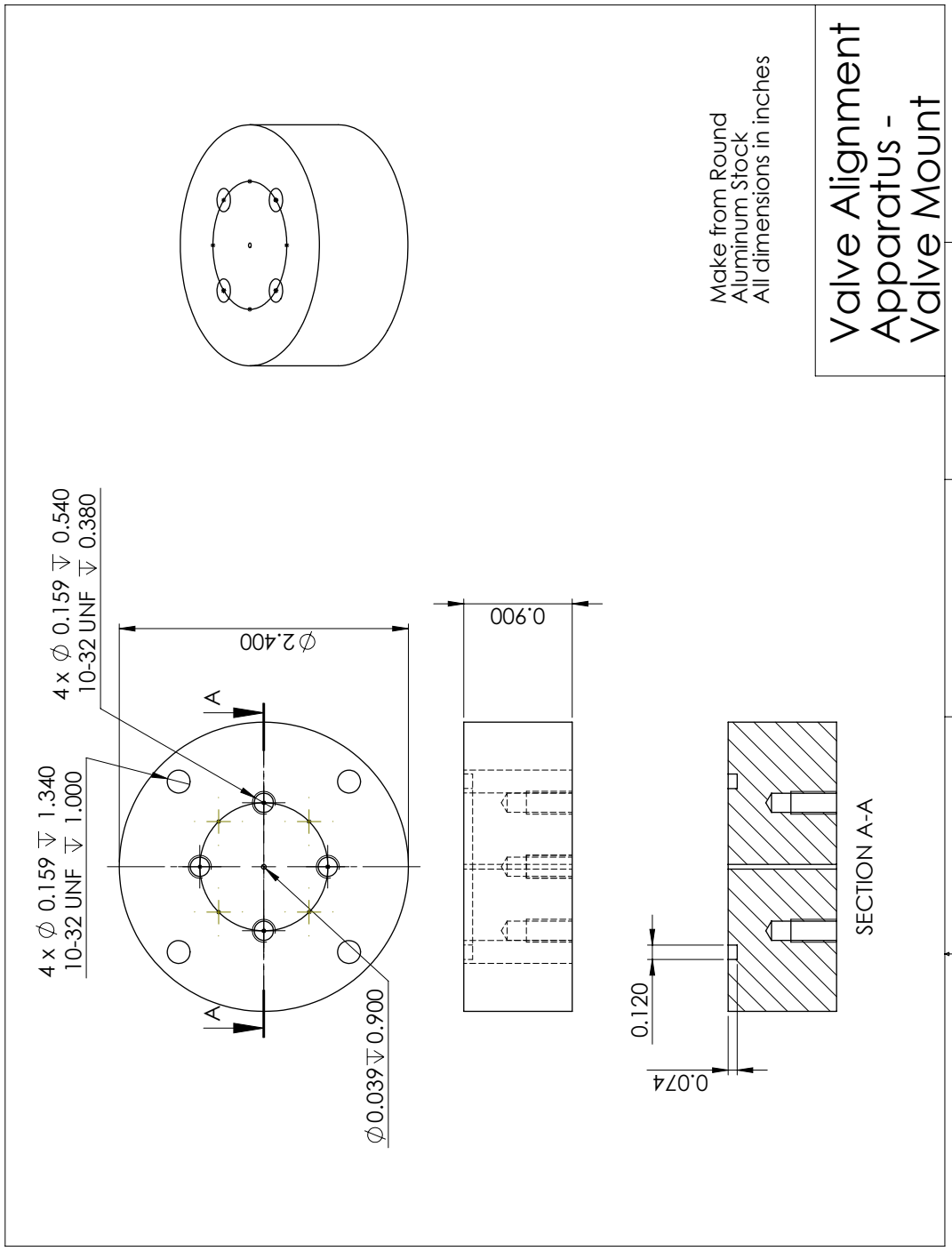

Figure A.3. Valve mount and nozzle wall emulating passage for valve alignment apparatus.

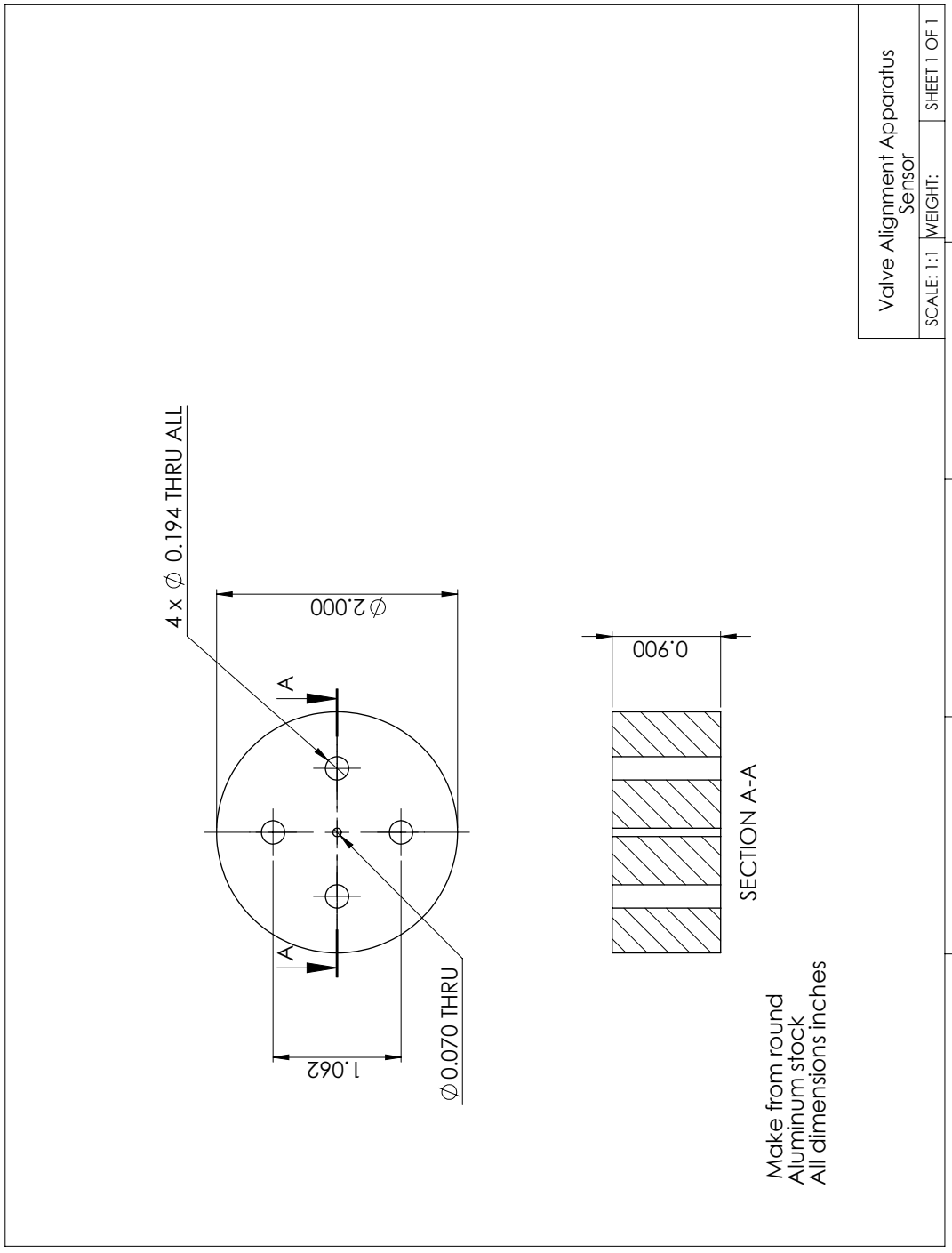

Figure A.4. Sensor mount for valve alignment apparatus.

B. New Traverse Plug Design

Significant tunnel time was lost due to the failure of dowel pin seals in the traverse plug. When a dowel pin failed it resulted in a multiple day down time while waiting for glue removal and then for the new adhesive to dry. In order to alleviate this issue, the traverse plug design was modified to allow quick removal and replacement of sensors and plugs through the use of self sealing bolts that were modified for use as sensor plugs.

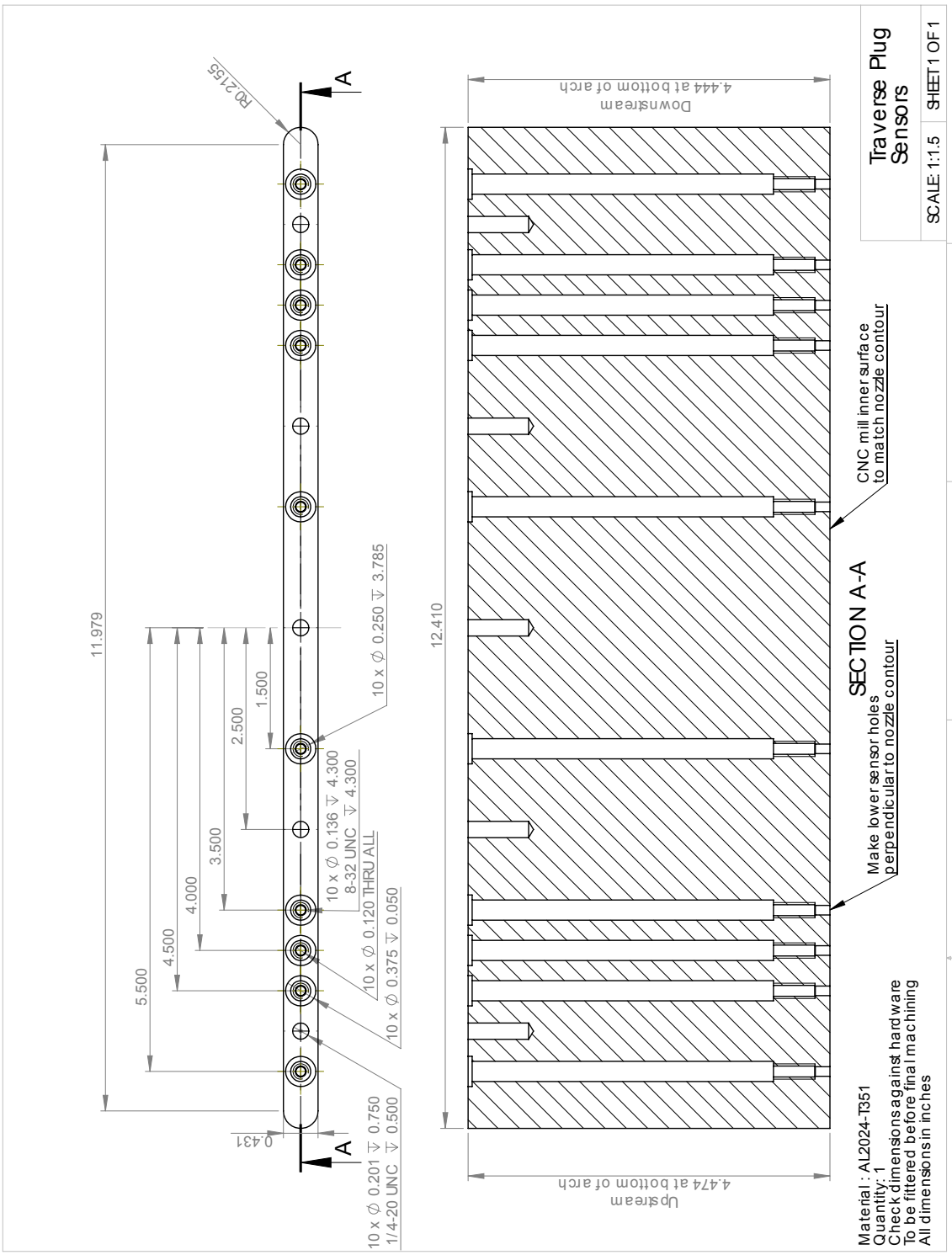

Figure B.1. Traverse plug schematic.

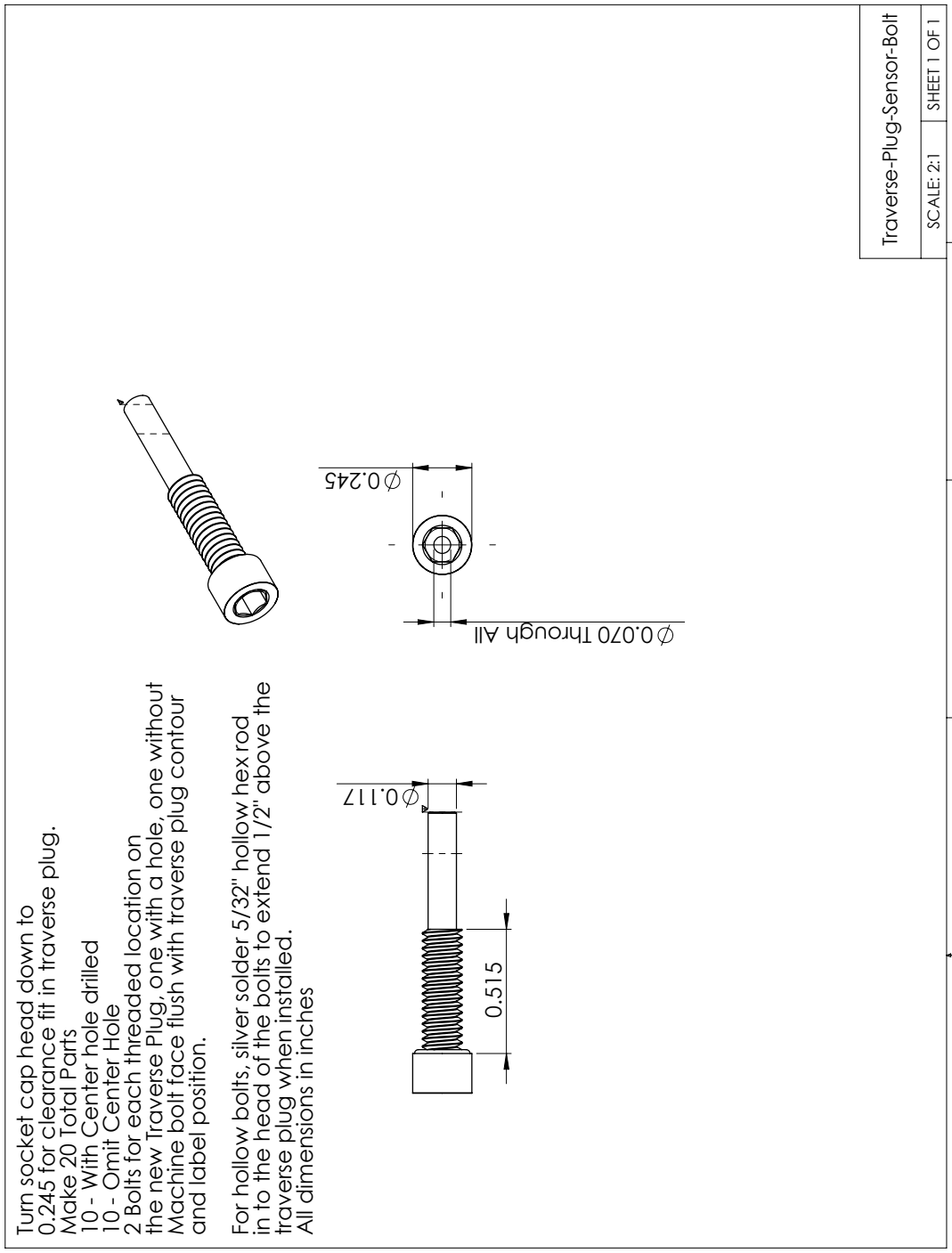

Figure B.2. Traverse plug sensor bolt schematic.

C. Changes from JAFCI Pulse Valve Driver Schematics

Several component values in the JAFCI Pulse Valve Driver schematics were changed to better suit the needs of the experiment in the BAM6QT. The changes are listed in Table C.1

Table C.1 Modified Components from JAFCI Pulsed Valve Driver

Component Number in JAFCI Schematic	New Component Value
R12	Paralleled 48 kΩ
C1	4.7μF
C11	3.3 nF

D. MATLAB Codes

```
function [start,finish,time] = detect(X,fs)
%detect.m determines the start and end times of the perturbations generated
%by the pulsed jet perturber.

% Inputs
%   X     - Burst samples, can be a single sample, or a group
%   fs    - Sampling Frequency

% Outputs
%   start  - sample index marking the beginning of the perturbation
%   finish - sample index marking the end of the perturbation
%   time   - duration of the perturbation

[m,n]=size(X);
X = mean(X,2)

% The relative magnitude (mag) and the perutrbation derivative (dpdt) are
% determined, and then the product of mag*dpdt^2 is taken to produce a
% signal where the high frequency components are emphasized (D).
mag = abs(((X)-(min((X))'*ones(1,m))')./...
     ((max((X))-min((X)))'*ones(1,m))');
dpdt=zeros(m,n);
for i = 2:m-1
    dpdt(i,:) = (X(i+1,:)-X(i-1,:))/(2/fs);
end
```

```
D = mag.*abs(dpdt).^2;

% D exponentially averaged across a number of sample segments
tau = m/fs;
delt = tau/24;
C = zeros(m,n);
for i = 1:m
    if i>tau/(2*delt) && i<m-tau/(2*delt)
    C(i,:)=delt^2/(1+tau/delt)*...
        sum(exp(-(.625/(tau/delt))*abs((i-tau/(2*delt):i+tau/(2*delt))'...
        *ones(1,n)-i)).*D(i-tau/(2*delt):i+tau/(2*delt),:));
    else
        C(i,:) = 0;
    end
end

% Determine where the signal meets the threshold requirements
Q = C>.001;
for i=1:1
    if i>3
        start(i)  = find(C(50:end)>.001,1,'first')+50;
    else
        start(i) = find(C(50:end)>.001,1,'first')+50;
    end
    finish(i) = find(Q(start(i)+.000160*fs:end,i)==0,1,'first')...
    +start(i)+.00016*fs;
end

startf = floor(mean(start));
```

```
finishf = floor(mean(finish));
time = (finish-start)./fs;
end
```